Doctoral (Ph.D.) Dissertation

Attila Kormányos

PHOTOELECTROCHEMISTRY OF CONDUCTING POLYMER-BASED NANOHYBRID ELECTRODES

SUPERVISORS:

Dr. Csaba Janáky

Assistant Professor

Prof. Csaba Visy

Professor Emeritus

University of Szeged
Faculty of Science and Informatics
Department of Physical Chemistry and Materials Science
Doctoral School of Chemistry

2018

TABLE OF CONTENTS

LIST OF ABBREVIATIONS

APS – ambient pressure UV photoelectron spectroscopy

BID – dielectric barrier discharge ionization detector

COF – covalent organic framework

CNT – carbon nanotubes

CP – conducting polymer

CPD – contact potential difference

CV – cyclic voltammogram

E_{BG} – bandgap energy

E_{CB} – conduction band edge energy

E_F – Fermi-level energy

E_{VB} – valence band edge energy

EDOT – 3,4-ethylenedioxythiophene

EIS – electrochemical impedance spectroscopy

EQE – external quantum efficiency

FT-IR – Fourier-transform infrared

GC – glassy carbon

GC-BID – gas chromatograph coupled with a barrier dielectric discharge detector

GC-MS – gas chromatograph coupled with a mass spectrometer detector

IPCE – incident photon-to-current-conversion efficiency

MWCNT – multi-walled carbon nanotubes

PANI – polyaniline

PC – photocatalytic

PEC – photoelectrochemical

PEDOT – poly(3,4-ethylenedioxythiophene)

PNMANI – poly(N-methylaniline)

PPY – polypyrrole

QCM – quartz crystal microgravimetry

SC – semiconductor

SDS – sodium dodecyl sulfate

SHE – standard hydrogen electrode

TGA – thermogravimetric analysis

LIST OF FIGURES

1. INTRODUCTION

One of the most critical challenges and paradigms of the 21st century is the shift in energy use from fossil fuels to renewable sources. Sunlight is undoubtedly one of the most valuable resources in the quest for a diversified and sustainable energy supply [1,2]. Sun delivers around $1.2 \cdot 10^5$ terawatts of solar energy to Earth, which is about 9000 times as much as the entire human population produces (currently approximately 18 terawatts) [3,4]. While solar energy is the most abundant energy source on our planet, its intermittency necessitates the storage of the harvested energy. There are several ways to utilize this tremendous amount of energy as it is presented in **Fig. 1**. In the case of solar cells, when the applied n-type semiconductor (SC) is illuminated, charge carrier generation occurs, resulting in electron-hole pairs. The electrons and holes are separated at the p-n junction (where the n-, and p-type SC is connected). After charge separation, the charge carriers are driven to the external electrodes (by the space charge, developing at the p-n junction interface), which generates a potential difference (**Fig. 1A**). The generated electricity can be stored in batteries or used to produce solar fuels or other useful chemicals.

Sunlight can also be converted directly to chemicals, to which the oldest, best-known example is photosynthesis (**Fig. 1B**), developed to perfection by nature during the past billion years. Inspired by Nature, researchers created methods, called artificial photosynthesis, which also aims to convert solar energy to useful products, but using totally different approaches and man-made materials (**Fig. 1C**) [5]. There are two major methods under the umbrella of artificial photosynthesis, one of them is photocatalysis (only heterogeneous photocatalysis belongs to the interest of this dissertation, therefore only this one is elaborated further) and the other is photoelectrochemistry. In a photocatalytic (PC) setup, SC nanoparticles are dispersed in a solution, containing the reactants. After illuminating the dispersion with a light, having higher energy than the bandgap of the SC, a charge separation occurs in the SC nanoparticles, and these photogenerated charge carriers can drive the conversion of the reactants to products on the surface of the nanoparticles. Importantly, in a PC setup both half-cell reactions (driven by either the holes or electrons) take place at the surface of the SC nanoparticles. The difference between a PC and photoelectrochemical (PEC) setup is that in a PEC cell, i) the SC nanoparticles are immobilized on an electrode surface, ii) the two half reactions are isolated (by a

membrane), therefore products form separately and iii) external bias is applied to suppress the recombination of the photogenerated charge carriers, thus assisting the conversion of the substrate(s) to products [6].

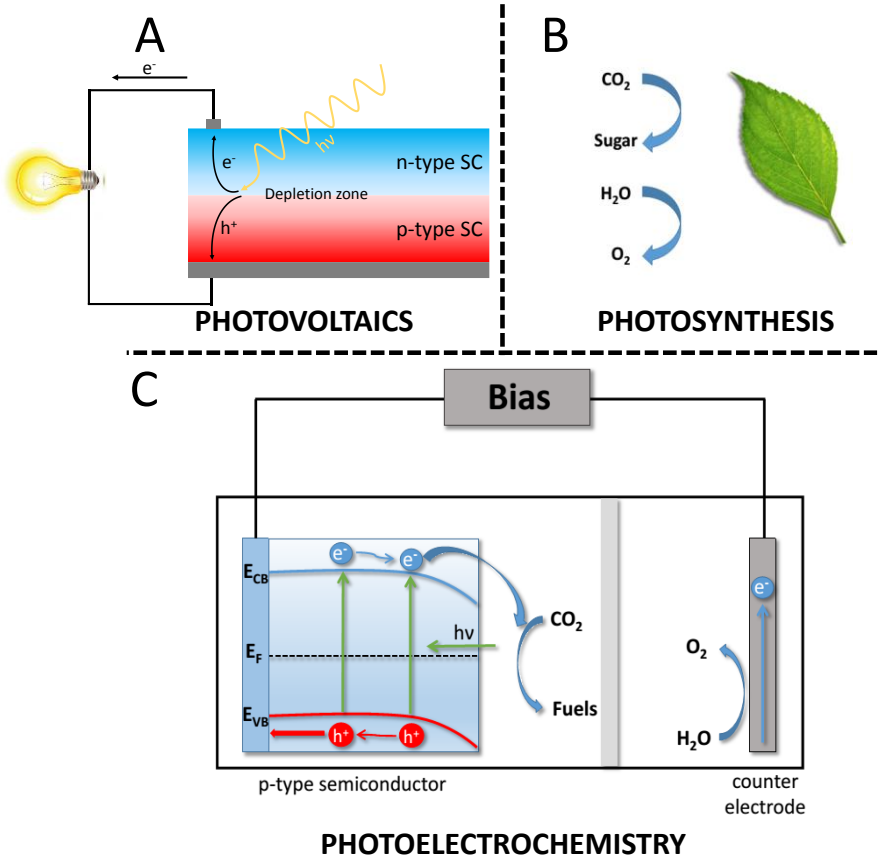

Fig. 1: Methods of solar energy conversion. (A) Photovoltaic, (B) photosynthetic and (C) photoelectrochemical method, utilizing a p-type SC as a photocathode.

The main and most widely studied half reactions include H^+-reduction, water oxidation and the conversion of CO_2 to various chemicals, such as CO, CH_4, HCOOH, CH_3OH, and other alcohols [7]. Endeavors in the field are directed to find materials which can be used to drive these reactions efficiently and cost-effectively, ultimately opening an avenue to industrial applications. The present work focuses on the synthesis of such new materials, and the investigation of their PEC properties along with their applicability as photoelectrodes in solar fuel generation processes.

2. LITERATURE BACKGROUND

2.1 Challenges of photoelectrochemical CO_2 reduction

The two major categories of solar fuels are H_2, produced by solar water splitting, and high-energy chemicals, for example, CO, CH_4, HCOOH and CH_3OH, etc. obtained via the PC or PEC conversion of CO_2 [8,9]. Both H^+- and CO_2 reduction are *thermodynamically uphill* reactions [8,10]. Furthermore, these processes are *multi-electron* in nature (e. g., it requires 6 electrons to reduce CO_2 to methanol), and in parallel, *kinetically hindered*. The formal electrochemical redox potentials for various CO_2 reduction reactions are presented in **Table 1**. The values are given at pH = 7.0, vs. the standard hydrogen electrode (SHE). The $E^{0'}$ value of the H^+ reduction reaction is also presented, because it has to be always expected as a competing process with the reduction of CO_2, since its formal potential is close to those of the multi-electron reduction of CO_2. Most of the data, presented in **Table 1** imply that the multi-electron reduction of CO_2 can be driven at moderately negative potentials (e.g., $E^{0'}$ = −0.53 V vs. SHE at pH = 7.0 for the formation of CO). On the other hand, notably more negative potential is needed for the one-electron reduction of CO_2. This can be a problematic factor mostly in the case of metal electrodes, where $CO_2^{\cdot-}$ often forms as an intermediate [11]. This very negative formal potential is due to the stability of the linear CO_2 molecule. It requires the investment of a large-amount of energy to change the hybridization of the central carbon atom from sp^2 to sp^3 [12–14], thus to shift from a very stable structure to an unstable, tensed one. Another serious factor which makes the conversion of CO_2 in large quantities challenging, is its low solubility in aqueous media (0.033 mol dm^{-3}) at atmospheric pressure. Poor solubility requires either the use of elevated pressure [15] during the experiments or using organic media, such as acetonitrile (0.205 mol dm^{-3}), tetrahydrofuran (0.279 mol dm^{-3}) or dimethyl-sulfoxide (0.138 mol dm^{-3}) [11,16]. Note that if an aprotic solvent is used, water has to be added as a H^+-source (typically ≈ 1%), since CO_2-reduction processes are proton transfer-coupled

Table 1: Formal electrochemical redox potentials ($E^{0'}$) for the reduction of CO_2 and H^+ in aqueous media (pH = 7.0 vs SHE) [8,9].

#	Reduction reaction	$E^{0'}$/V (vs. SHE)
1	$CO_2 + e^- \rightarrow CO_2^{\cdot -}$	−1.90
2	$CO_2 + 2H^+ + 2e^- \rightarrow HCOOH$	−0.61
3	$CO_2 + 2H^+ + 2e^- \rightarrow CO + H_2O$	−0.53
4	$CO_2 + 4H^+ + 4e^- \rightarrow HCOH + H_2O$	−0.48
5	$2H^+ + 2e^- \rightarrow H_2$	−0.41
6	$CO_2 + 6H^+ + 6e^- \rightarrow CH_3OH + H_2O$	−0.38
7	$2CO_2 + 8H_2O + 12e^- \rightarrow C_2H_4 + 12OH^-$	−0.34
8	$CO_2 + 8H^+ + 8e^- \rightarrow CH_4 + 2H_2O$	−0.24

In light of these difficulties, there are certain properties, which a good photoelectrode material has to *simultaneously* bear with to maximize efficiency and cost-effectiveness. These include [17]:

- *The bandgap* has to be narrow enough to effectively utilize the whole solar spectrum, but wide enough to avoid the fast recombination of the photogenerated charge carriers.
- *Band edge positions* should be optimal to drive the desired redox process. For example, if a p-type SC is employed in PEC CO_2 reduction process, the conduction band energy (E_{CB}) has to be negative enough, thus the photogenerated e- is able to reduce CO_2. However, if it is too negative, significant amount of the photopotential can be lost, which should be avoided.
- Good chemical-, electrochemical- and photo*stability* over a wide pH-, and potential window is required
- *Facile charge transport*, which ensures that most of the photogenerated charge carriers can be extracted both toward the electrode/electrolyte junction and toward the back contact, without significant recombination. In practice, in the case of a p-type SC this means, that the higher the mobility of the photogenerated electrons, the higher the harvested cathodic photocurrent.

- *Facile charge transfer* from the SC/liquid junction to the substrate molecule: appropriate band positions and bandgap only provide thermodynamic criteria to the PEC conversion of H^+ or CO_2. Since these reactions are multi-electron in nature, facile charge carrier transfer from the SC to the substrate molecule(s) is a vital kinetic criterion.
- High *selectivity* towards the formation of the targeted products.
- Low *toxicity*.
- Reasonable *production cost.*

2.2 Photoelectrode materials – inorganic semiconductors

Mostly inorganic SCs were applied as photoelectrode materials in the past decades. Several p-type materials have been already studied as photocathodes, ranging from elemental SCs, such as p-Si[18] to binary SCs in the Group 12-16 families, for example, SiC, CdTe, InP, ZnTe, GaP, GaAs, etc [19]. Beyond these, a lot of binary and ternary metal oxides (mostly Cu-based) were also studied in this vein, for example Cu_2O, CuO, Cu_2O/CuO, $CuFeO_2$, $CuNb_2O_6$, $Cu_3Nb_2O_8$, $CuRhO_2$, etc [20–22]. Almost all the listed inorganic p-SCs have narrow bandgap, resulting in good overlap with the solar spectrum and their E_{CB} is sufficiently negative, thus making them able to reduce H^+ and CO_2.

On the other hand, most of the narrow-bandgap p-type inorganic SCs are inherently chemically and electrochemically unstable upon photoexcitation and in contact with aqueous media. It can be concluded that *none* of the studied inorganic SCs have met all the listed requirements and *none* of them have reached the performance level required for practical application so far.

2.3 SiC as a promising photoelectrode material

Because SiC was investigated as a possible photoelectrode material to drive PEC CO_2 reduction during my PhD studies, its (P)EC properties are detailed further. Silicon carbide is a wide-bandgap (E_{BG} = 2.4 – 3.1 eV) semiconductor, which exhibits either n-, or p-type behavior depending on the polymorph (note that over a hundred different polytypes are known for SiC) and the exact composition. The crystal structure of the most common ones are showed in **Fig. 2** [23–25]. Many of them have excellent mechanical properties and

chemical stability, high thermal conductivity, biocompatibility, diverse surface chemistry, and affordable production cost [26–29].

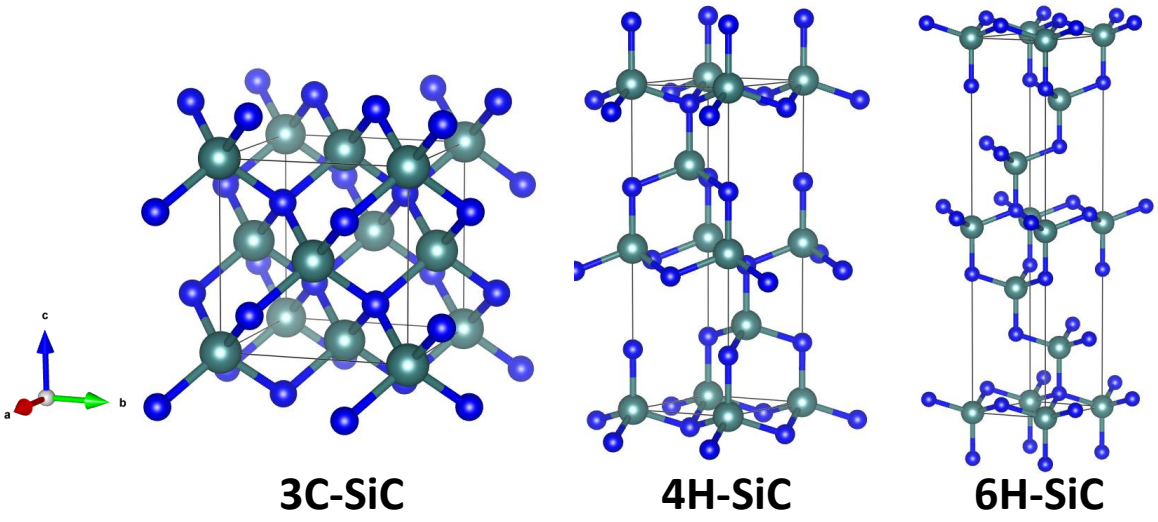

Fig. 2: Crystal structures of the most common polytypes of SiC [30]. Si: grey spheres, C: blue spheres.

Furthermore, the conduction band edge position of SiC allows its application for the photodriven reduction of water and CO_2. This latter was first demonstrated in 1979 [31]. The main products were hydrogen and methanol, along with some formaldehyde. Contrastingly, when we tried to employ the cubic polytype (3C-SiC, which behaves as a p-type SC) for the PEC reduction of CO_2, only marginal photocurrents were detected (**Fig. 3 inset**). Furthermore, the photoresponse of SiC was very slow (the applied sweep rate was only 0.5 mV s^{-1} during the measurements shown in **Fig. 3**) indicating that both H^+-, and CO_2-reduction processes are *kinetically hindered* on the surface of the SiC nanoparticles. This statement was also supported by the experiments performed in O_2 atmosphere: the photocurrents increased, mostly because O_2 acted as an e^- - scavenger and rapidly reacted with the photogenerated electrons. According to these observations, if the surface of the nanoparticles is modified with a co-catalyst which acts as a mediator of the targeted reaction, the sluggish surface kinetics can be improved and the promising properties of SiC can be harnessed.

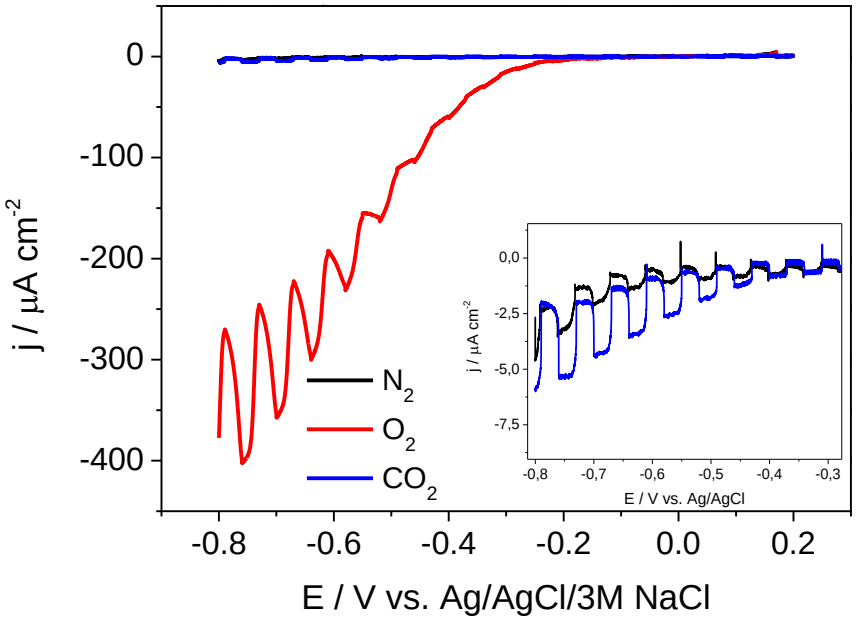

Fig. 3: Photovoltammograms recorded for SiC-modified glassy carbon (GC) electrodes (m_{SiC} = 0.4 mg cm^{-2}); in N_2-saturated 0.1 M Na_2SO_4, O_2-saturated 0.1 M Na_2SO_4 and CO_2-saturated 0.1 M $NaHCO_3$ solutions (all *pH* ≈ 7.0). The sweep rate was kept at 0.5 mV s^{-1}, while the light-chopping frequency was 0.05 Hz. A 300W Hg-Xe lamp was used as a UV-vis light source. The inset shows the enlarged photovoltammograms, recorded in N_2-saturated 0.1 M Na_2SO_4 and CO_2-saturated 0.1 M $NaHCO_3$ solutions.

2.4 Organic photoelectrodes

Contrary to inorganic SCs, only a few organic SC have been applied in the field of solar fuel generation. The family of organic SCs can be divided to four main categories (**Fig. 4**)[32]:

1. Small organic molecules
2. Carbon nitrides
3. Covalent organic frameworks
4. Conducting polymers

Molecular organic SCs are small conjugated molecules with well-defined structure and definite molecular weight. Graphitic carbon nitrides (g-C_3N_4) comprise of alternating C-N bonds without any carbon-carbon or carbon-hydrogen connection. One possible structure is shown in **Fig. 4**. These materials are electron-deficient and have suitable optical properties for PEC applications (e.g., 2.4 ≤ E_{BG} ≤ 2.7 depending on structural variations and adatoms [33]), thus they are coming more and more to the forefront of research [34]. Covalent organic frameworks (COFs) are extended structures with periodic molecular orderings and inherent porosity (very high active surface area), allowing these materials to

be used as excellent CO_2 adsorbents [35]. Moreover, it has been shown recently that COFs can be used as photocathode materials for PEC H_2 evolution [36,37]. Electron conducting polymers belong to the fourth category of organic SCs. These are polymers represented as molecules with alternating single and double bonds (π-conjugation). Most of them contain heteroatoms, such as O, N and S. Some common examples are presented in **Fig. 4**, such as polypyrrole (PPy), poly(3,4-ethylenedioxythiophene) (PEDOT) and polyaniline (PANI). Since my dissertation focuses on the PEC properties of these materials, only this last category is discussed in detail from now on.

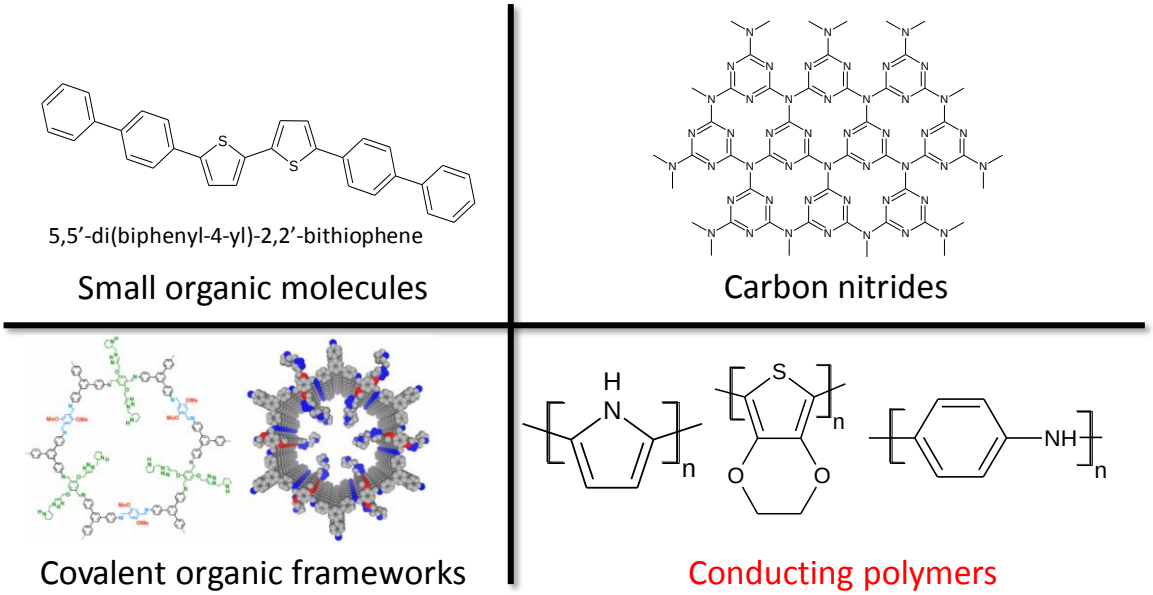

Fig. 4: The main categories of organic SCs.

The most important difference between conducting polymers (CPs) and other polymers (i.e., plastics) is that their conductivity can be varied within wide limits (5-10 orders of magnitude) [38]. Since the discovery of CPs in the 1970s, both their structure and the mechanism of conductivity have been extensively studied. In a polymer, just as in a crystal, the interaction of a polymer unit cell with all its neighbors leads to the formation of electronic bands. The highest occupied electronic levels constitute the valence band (VB), and the lowest unoccupied levels the conduction band (CB), respectively [39]. When they are in their fully reduced state, CPs behave as insulators/SCs, depending on the bandgap (see **Fig. 5** for the corresponding band diagrams). Upon oxidation, the removal of an electron from the VB creates charge carriers, a positive hole, and an unpaired electron and a polaron forms. Due to the delocalized electron system these charge carriers can freely move along the chain several monomeric units. This distance is characterized by the

effective conjugation length [40], which gives the average number of the segments, participating in delocalization along the polymer chain. In a real sample, π-conjugation is not infinite, defects often interrupt the delocalized structure. Electrons can travel between these interrupted segments by electron hopping [41]. According to early interpretations, first, new energy levels appear in between the VB- and CB edges during oxidation. If the degree of doping is high enough, the newly formed energy levels overlap, and form new bands, resulting in a slightly widened bandgap [39].

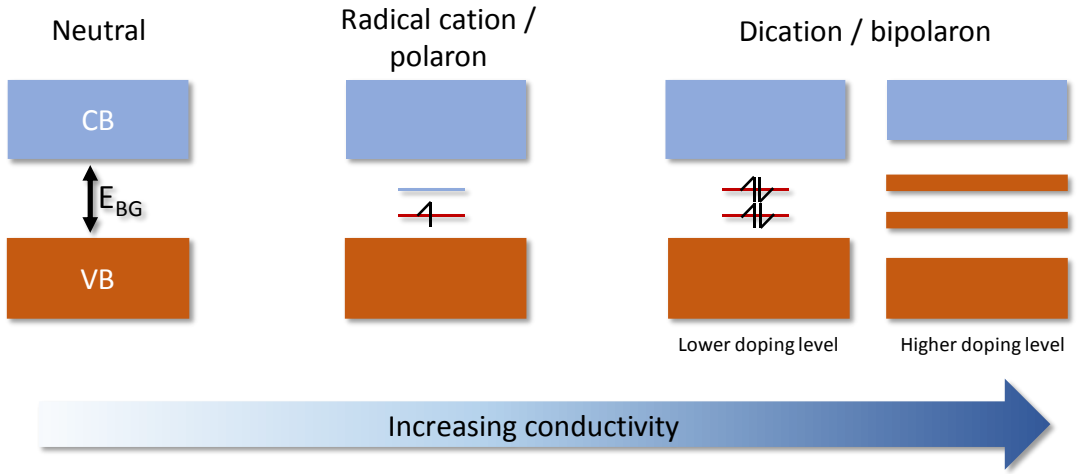

Fig. 5: Evolution of conductivity in CPs.

The synthesis techniques of CPs can be divided in three major categories: i) *chemical*-, ii) *electrochemical*, and iii) *photocatalytic* polymerization. All three methods have a similar basis: in the first step, the monomer molecule must be oxidized in the first step to form a radical cation. This can be achieved either by using a strong oxidant or by applying appropriately positive electrochemical bias and finally, by photoexciting the surface of a SC and utilizing the photogenerated holes to drive the polymerization. Because the latter two methods were used to form CP layers during my doctoral work, only these are detailed here.

The main advantage of oxidative electrochemical polymerization is that the thickness of the electrodeposited CP films can be easily controlled by the polymerization charge density. Furthermore, the electrodeposited CP can be immediately investigated by various electrochemical techniques or applied as an electrode. An example to the mechanism of the electropolymerization is shown in **Fig. 6** for PANI [42].

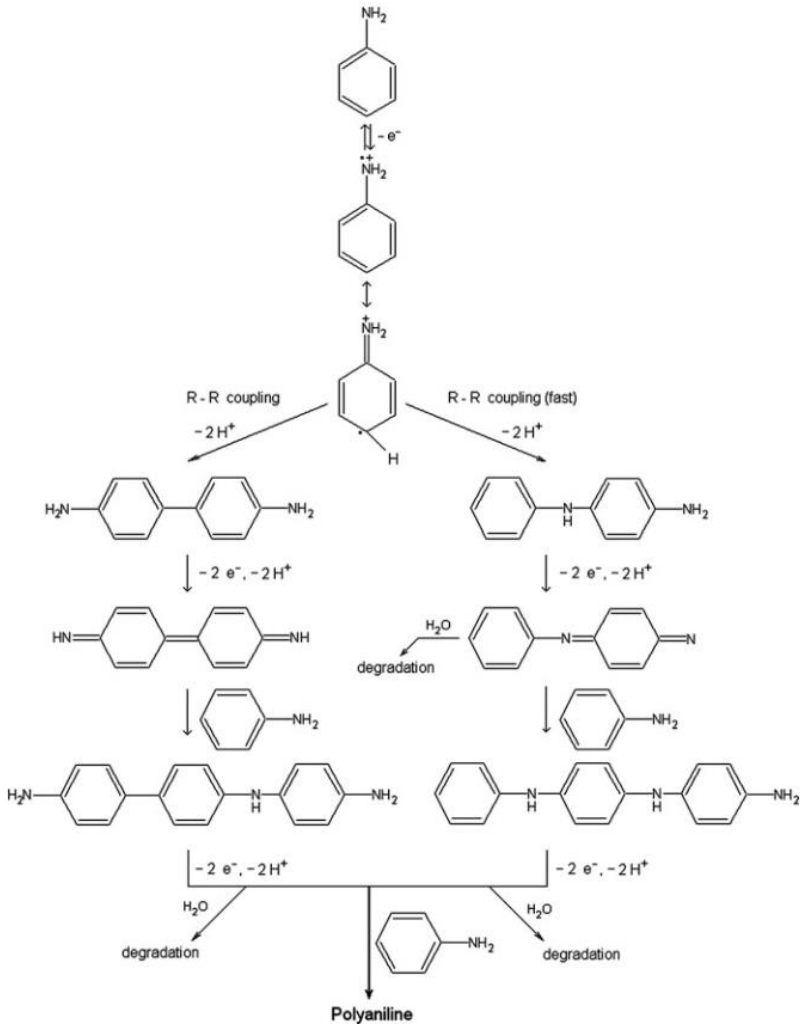

Fig. 6: Reaction scheme for the electropolymerization of aniline [42].

Electrodeposition methods can be categorized as *static*-, and *dynamic* techniques. By using a static technique (i.e., performing the electrodeposition at a constant current/potential), the amount of the electrodeposited polymer can be easily controlled by the polymerization charge density. The main advantage of dynamic techniques is that the synthesis is not limited by the diffusion of the monomer molecules to the electrode surface. [43,44]. In both static and dynamic deposition protocols the overoxidation of the polymer can be easily avoided by controlling the electrode potential. On the other hand, current controlled polymerization ensures high control over the growth rate of the polymer layer.

Most CPs typically behave as p-type SCs [45,46]. Interestingly, there are significantly less studies in the literature on the PEC properties of organic SCs compared to their inorganic counterparts. The first ones were performed on PANI, in the mid' 80s [45], when small cathodic photocurrents were observed applying negative bias and visible light

irradiation. Since then a few studies were published on this topic[47–54], and the PEC behavior was also studied for PPy [46,55], poly(3-methyltiophene) [56–58], substituted PANIs [47], and for poly(benzimidazobenzophenantroline) [59].

CPs are promising photoelectrode candidates due to their several beneficial properties, namely:

- CPs can be prepared via *mild synthetic routes* (such as electrodeposition), which result in short energy payback time.
- Processing and fabrication of high surface area photoelectrodes is *convenient* and *cheap*.
- The polymer structure can be *tailored* to fit to the requirements of the given application (e.g., tunable bandgap, high CO_2-adsorption capacity) [60,61].
- Several N-containing CPs showed *reasonable catalytic activity* toward the electrochemical reduction of CO_2 [62,63], which implies that N-atoms play a key role in this process – note that polyimides are among the best CO_2 absorbents [64].

CPs also suffer from some disadvantages which limit their applicability as photoelectrode materials. One of them is the *low charge carrier mobility*, which results in extensive recombination and thus small photocurrents. Their typical charge carrier mobility values are 0.01 – 0.1 $cm^2\ V^{-1}\ s^{-1}$ (for poly(3-hexylthiophene) (P3HT)) [65,66], and 0.045 – 1.7 $cm^2\ V^{-1}\ s^{-1}$ (for PEDOT:(poly(styrenesulfonate) − PSS) [67]. Accordingly, it is not possible to increase the polymer thickness on the current collector to a level where light absorption is sufficient because the photogenerated charge carriers recombine before they could be fully extracted. Finally, most CPs have *poor photostability*, especially under UV-light irradiation.

Judging by the number of articles published on the PEC behavior of PANI, it can be concluded that this is the most widely studied CP in this vein. Unfortunately there are many controversies in the literature, concerning i) the origin of the photocurrent [50–52], ii) the mechanism of photodegradation [52,68], iii) the potential window where PANI is photoelectroactive [49,50,52,54–56]. Therefore, some of their conclusions have to be handled with caution. PANI is a particularly attractive CP, because of its versatile redox behavior (it has many different intrinsic oxidation states), excellent chemical and electrochemical stability, large charge capacitance, and electrochromic properties [69–71]. On the other hand, with a bandgap of approximately 2.8 eV [72–74], PANI only can utilize

a small portion of solar irradiation, meaning that it can be efficiently excited by only UV-light. Unfortunately, as in the case of almost all CPs, the mobility of the photogenerated charge carriers is quite small, typically in the range of 0.0001 – 0.01 $cm^2\ V^{-1}\ s^{-1}$ [75–77]. Despite these disadvantages, what still makes PANI a potential photoelectrode candidate for solar fuel generation purposes is that its E_{CB} is negative enough (**Fig. 7**), therefore the photogenerated e^- can reduce either CO_2 or H^+. Moreover, the monomer structure contains a nitrogen heteroatom (see **Fig. 4**), which might result in increased CO_2-adsorption capacity. This can be a crucial property in the PEC reduction of CO_2, since its reduction is multi-electron in nature, thus substrate molecules staying close to the electrode surface longer can highly enhance the efficacy of these processes. PANI itself has been already employed as a photoelectrocatalyst for PEC H_2 evolution [78], along with its hybrids with inorganic SCs (ZnO, Cds) [79,80].

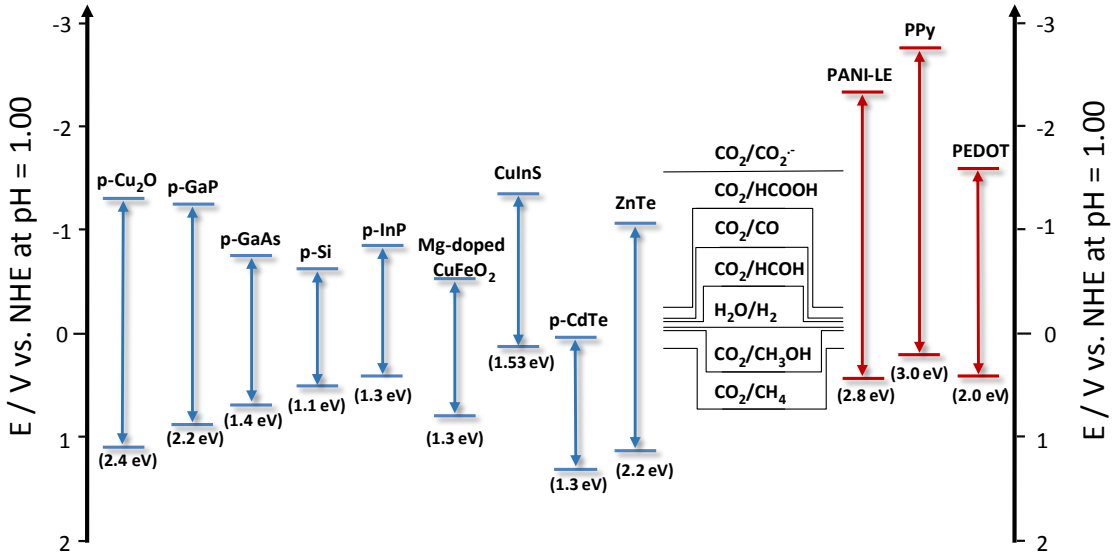

Fig. 7: Comparison of the band edge positions of the most frequently employed p-type inorganic SCs and some common CPs, along with the thermodynamic potentials for H^+ and CO_2 reduction to different products [9,78,81–83].

To the best of my knowledge, no studies have been performed yet concerning the PEC CO_2 reduction ability of PANI itself. A bit more can be found on its hybrids with inorganic complexes[62] or SCs: PANI/p-Si hybrid was studied as a photoelectrode material in this manner [84]. The main products were formic acid and formaldehyde along with the formation of H_2.

To overcome the issues, originating from the wide bandgap of PANI, other, narrow-bandgap CPs, such as PEDOT can be taken in consideration. PEDOT has a broad absorption band in its reduced form (**Fig. 8**). Moreover, its spectrum overlaps with the solar spectrum, which further highlights the promise of this material in solar fuel generation (**Fig. 8**). However, PEDOT also has poor charge carrier mobility values [67], which results in extensive recombination, thus small photocurrents. PEDOT has been successfully applied as an electrocatalyst for O_2 reduction and also proven to be a very stable and robust CP in dark conditions [85]. Moreover, PEDOT and its derivatives have already been widely used as hole-transporting materials in dye-sensitized solar cells [86–88]. Despite these applications, there is no comprehensive study in the literature on the PEC behavior of the pristine polymer; it has been only applied as a hole-selective layer in CP-based hybrid organic photocathodes [89]. These showed unprecedentedly high photocurrents, and high rates of PEC H_2-generation with the use of a homogeneous photocatalyst [89].

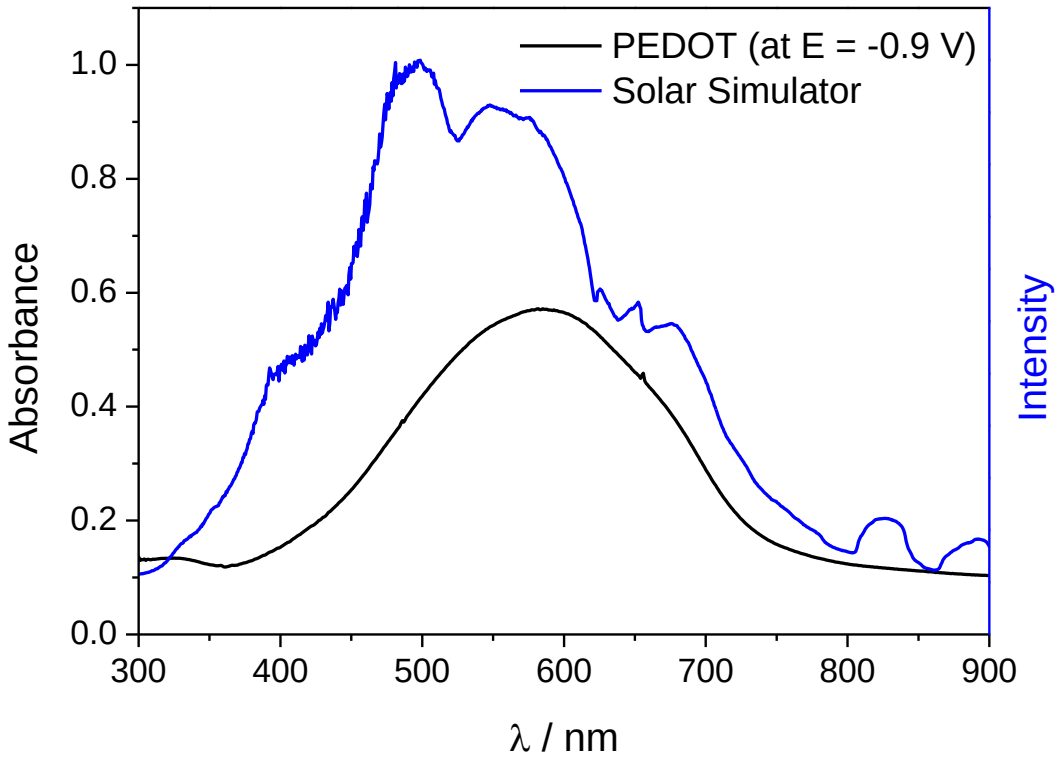

Fig. 8: Comparison of the UV-vis spectrum, recorded for a PEDOT layer (Q_{pol} = 25 mC cm^{-2}), at E = −0.9 V in 0.1 M Na_2SO_4 solution, saturated with Ar; with the irradiance spectrum of a solar simulator.

2.5 Nanocomposite photoelectrodes

To achieve the highest possible efficiency in solar fuel generation processes (in other words: to have a material with practical significance), three parameters must be simultaneously optimal for a photoelectrode material (visualized on the Venn-diagram, presented in **Fig. 9**):

- Optimal *light absorption*
- Optimal charge carrier *transport*
- Optimal charge carrier *transfer*.

Since there is no single (known) material, which possesses all three parameters in the ideal range, nanocomposites can be synthesized to reach this goal. In these hybrid systems, each constituent has a well-defined role, covering all three previously listed areas.

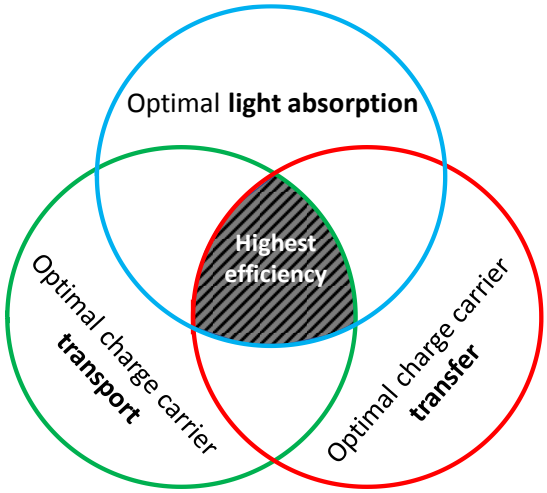

Fig. 9: Venn-diagram, representing the criteria which has to be met to achieve high efficiency in solar fuel generation.

Synthesis procedures can be classified in to two main categories. Methods, during both the CP and the SC components are synthesized separately, and the composite is assembled subsequently by a simple or more sophisticated blending, belong to the first category. The main advantage of such procedures, is their simplicity. Moreover, the resulting hybrid material is often solution-processible, and a large amount of material can be synthesized, which facilitates production and processing on an industrial scale. However, several unforeseen problems may occur by blending two (or more) components, such as: CPs may completely block the pores of the nanostructured component, the hydrophilic/hydrophobic characteristics nature of the components can be different, which

may further hamper the application of such procedures, etc.

The second category includes all methods, where one component of the nanocomposite material is synthesized in the presence of the other component. In-situ polymerization of the CP in the presence of the other counterpart (carbon nanotubes - CNTs, inorganic SCs, etc.) is one of such attractive techniques. In-situ polymerization can be carried out using two different strategies. In the first group, the other component is dispersed in the same solution as the monomer molecules, therefore polymerization results in composite particles, or thin films, depending on the initiation (chemical-, photocatalytic-, or electrochemical). Tactics, where the CP component is deposited on either electrodes − made of the other component (e.g., Si-, or SiC wafer, etc.) − or on the other component immobilized on a supporting electrode surface, belong to the second category. Both the composition and the morphology of the synthesized nanocomposites can significantly affect their PEC properties, therefore their *synthesis in a precisely controlled manner* is of prime importance. Typical drawbacks and limitations of hybrid materials derived by chemical techniques are: i) uncontrolled, random distribution of the nanoparticles in the CP matrix, ii) no-, or poor electrical contact between the nanocomposite and the supporting electrode surface, and iii) the particles can aggregate, which results in smaller active surface area. In contrast, electrochemical methods bear with several advantages, such as: a thin film can be directly formed on the electrode surface. Moreover, using electrochemical methods the film thickness, morphology, and porosity can be precisely regulated. Also, nanocomposites, deposited by applying such methods have a higher mechanical stability and strong adherence to the underlying electrode surface. In the following, two different strategies are outlined, which can be successfully applied to eliminate the weaknesses of the individual components [90]. Both subsection is followed by some examples to the synthesis of such nanocomposites, taken from the literature.

2.5.1 Charge carrier transport properties

Low charge carrier mobility results in extensive recombination, which is the one of the main reasons behind the small harvested photocurrents. A possible solution to overcome the limited conductivity of CPs or inorganic SCs is to deposit them on a *highly conductive* nanostructured scaffold. Thus, the distance that charge carriers have to travel toward the solution and the current collector is reduced along with a significant increase in

conductivity. Carbon nanomaterials, such as CNTs and graphene, are attractive candidates in this vein [91,92]. These nanocarbons have already been combined with inorganic SCs and the resulting nanocomposites were already studied in photocatalysis, photovoltaics, and in PEC reactions [93–101]. Some of the benefits of this strategy have been already demonstrated by our research group on the examples of Cu_2O/CNT and Cu_2O/graphene nanocomposites [21,95]. Compared to the bare Cu_2O, the conductivity and photocurrents increased, and the stability improved.

In contrast to the inorganic composites, the beneficial properties of CP/nanocarbon hybrid electrodes have been only exploited in fields outside solar energy conversion, most importantly in energy storage (in supercapacitors) [79,90,102]. There is only one exception, namely the family of CP/fullerene nanocomposites, which are applied in bulk-heterojunction solar cells. In these solar cells both the CP and the fullerene are both photoactive. In the two examples, presented in my dissertation, only the CP is photoactive, while the nanocarbons act as metallic conductors. No CP/nanocarbon hybrids have been applied as photoelectrodes so far, regardless of the many positive examples in the literature on inorganic SC/nanocarbon photoelectrodes.

2.5.2 Synthesis of conducting polymer/nanocarbon composites

The most convenient way to synthesize CP/nanocarbon nanocomposites is electrodeposition [90]. These can be separated in two categories (**Fig. 10**), depending on the 'condition' of the nanocarbon component. The first one is when the nanocarbon particles are dispersed in the polymerization solution along with the monomer and the supporting electrolyte. Subsequently, they are co-deposited on the electrode with the CP [103–106]. The surface modification of the CNTs and graphene flakes by an oxidative acidic treatment is common in these cases. As a result, −COOH, −OH, C=O, $-NH_2$ groups form on the surface of the nanocarbons, therefore making them more hydrophilic [107]. The main purpose of surface modifications is to allow nanocarbons to be dispersed in aqueous media. These charged surface moieties can highly enhance the doping-type incorporation or immobilization of nanocarbons in the CP matrix [107]. Co-deposition methods, unfortunately, are affected by some serious limitations, from which the two most important are that only the CP phase is in contact with the underlying electrode surface, and that nanocarbons are scattered in the CP matrix in an uncontrolled manner. Therefore,

the synergistic features (more efficient charge separation and transport) lying in the hybrid formation, cannot be prevailed.

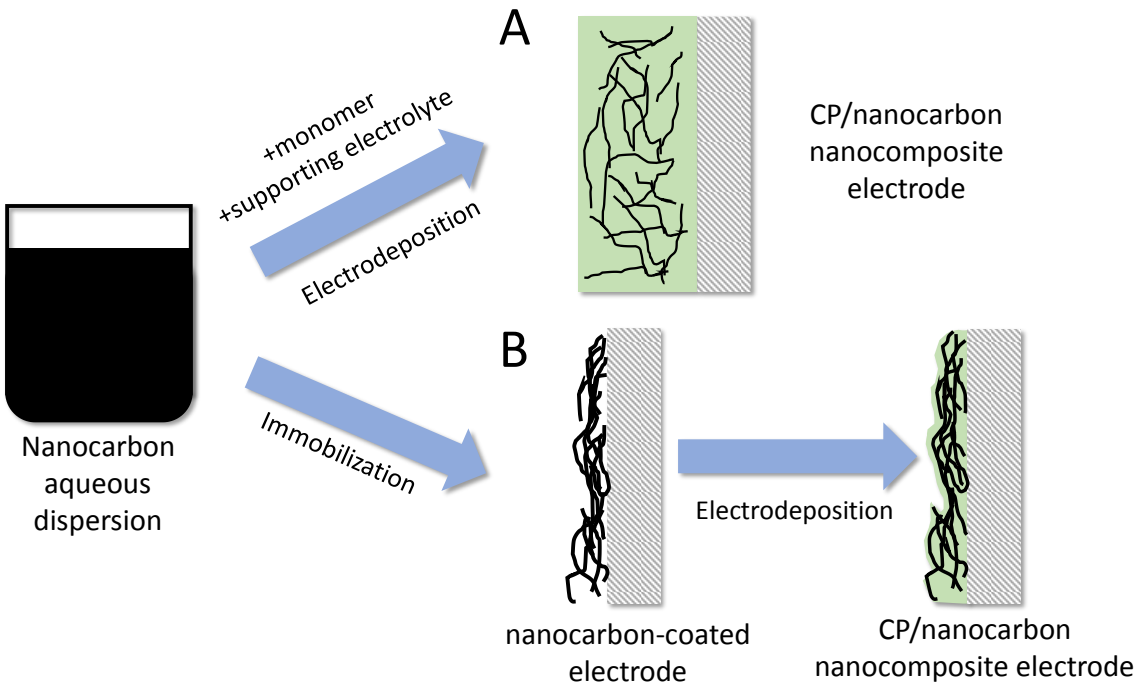

Fig. 10: The two main options for the synthesis of CP/nanocarbon nanocomposite electrodes: (A) co-deposition, (B) electrodeposition of CPs on an immobilized carbon nanonetwork.

The other case is when the nanocarbon is already immobilized on an inert electrode surface (GC, ITO, or noble metal) and this modified electrode is then used as a working electrode for the electrodeposition of the CP (**Fig. 10B**) [102,108–111]. Nanocarbons can be typically immobilized by drop-casting, spray-, or spin-coating from their aqueous dispersions on the working electrode surface. After immobilization of the nanocarbons, it is very important to remove the residual traces of the solvent, and to enhance their adhesion to the supporting electrode surface. Subsequent heat treatment in an oven is the simplest way to achieve that [21]. In contrast to the co-deposition technique, the nanocarbons are directly connected to the supporting electrode surface, therefore the expected enhancement in the charge carrier transport and conductivity can be realized. Furthermore, the amount of nanocarbon and CP in the nanocomposite can be precisely controlled along with the morphology [112]. There are many examples in the literature following this practice: PANI/CNT [108], PANI/CNT array [109], PANI/graphene [111], PEDOT/CNT [110] electrodes were synthesized in this vein. These nanocomposites were

applied almost exclusively as supercapacitors. Another, however much more difficult and expensive strategy for CNT immobilization is to grow aligned CNT forests on for example, an Al_2O_3-coated Si substrate [113], or flexible thin metal foils [114]. The advantage of such nanoarchitectures is the direct electrical contact between every synthesized nanotube and the supporting electrode. On the other hand, if the nanotubes are too long or the forest is too dense, it can negatively affect the light absorption properties of the CP/CNT nanohybrid, hampering their applicability as photoelectrodes. These handicaps can be avoided by carefully choosing the synthesis parameters, both the length, and the density of these forests can be tailored for the need of the desired application [113].

2.5.3 Charge carrier transfer properties

If the transfer of the photogenerated charge carriers (in the case of a p-type SC, electrons) through the SC/liquid interface to the redox active species is *facile*, PEC reactions can be efficiently driven on a SC photoelectrode surface (**Fig. 11A**). Contrastingly, if the transfer of the photoelectrons toward the redox active species is slow, charge carriers tend to recombine or get trapped in the surface states of the SC. Surface states form close to the surface of the SC, which typically caused by grain boundaries or by the termination of the crystal lattice at the SC surface [8]. Electron-hole recombination processes (occurring at the ps-ns timescale) are several orders of magnitudes faster than interfacial charge carrier transfer processes [115].

Combination of a SC with a co-catalyst is a promising avenue to enhance the solar to chemical conversion efficiency through improving the charge carrier transfer properties (**Fig. 11B-D**). In these cases, the SC only acts as a light absorber. After charge separation, the photogenerated charge carriers are transferred to the co-catalyst, on which all redox processes occur. Co-catalysts can be for example, i) metal or metal oxide nanoparticles (**Fig. 11B**), ii) inorganic complexes, or iii) organic molecules, etc. Co-catalysts can be intimately linked to the SC surface (then catalysis occurs on the surface of the catalyst – *heterogeneous* catalysis) or dissolved in the substrate-containing solution (catalysis occurs on the surface of the catalyst, but in the liquid phase – *homogeneous* catalysis see **Fig. 11C, D**). Importantly, the Fermi-level of the applied metal nanoparticle must lie below the E_{CB} of the SC and above the redox potential of the desired reaction to act as an electron shuttle [116]. One of such metals is Pt, which is still considered as the state-of-the-art

electrocatalyst for the electrochemical H_2-evolution. The effect of depositing Pt nanoparticles on a surface of a nanostructured NiO has been investigated in our research group recently [117]. The effect of both the size and loading of the deposited Pt nanoparticles were carefully studied and an overall 20-fold increase was achieved in terms of photocurrents and thus H_2 evolution rates, compared to the bare nanostructured NiO photocathode. This concept has been applied for other SC photocathodes too, utilized in PEC CO_2 reduction processes, such as p-type Si, of which surface was decorated with Cu, Ag and Au [118]. On the modified electrodes methane, ethylene, and carbon monoxide, etc., formed from the PEC CO_2 reduction similarly to the pristine metal electrodes, but at approximately 0.5 V more positive potential and with higher efficiencies. Another prominent example is Co_3O_4, which was decorated with Cu nanoparticles. CO_2 has been photoelectrocatalytically reduced to formate with high yield (6.75 mmol dm^3 cm^{-2} in 8 h) and high selectivity (close to 100%) [119].

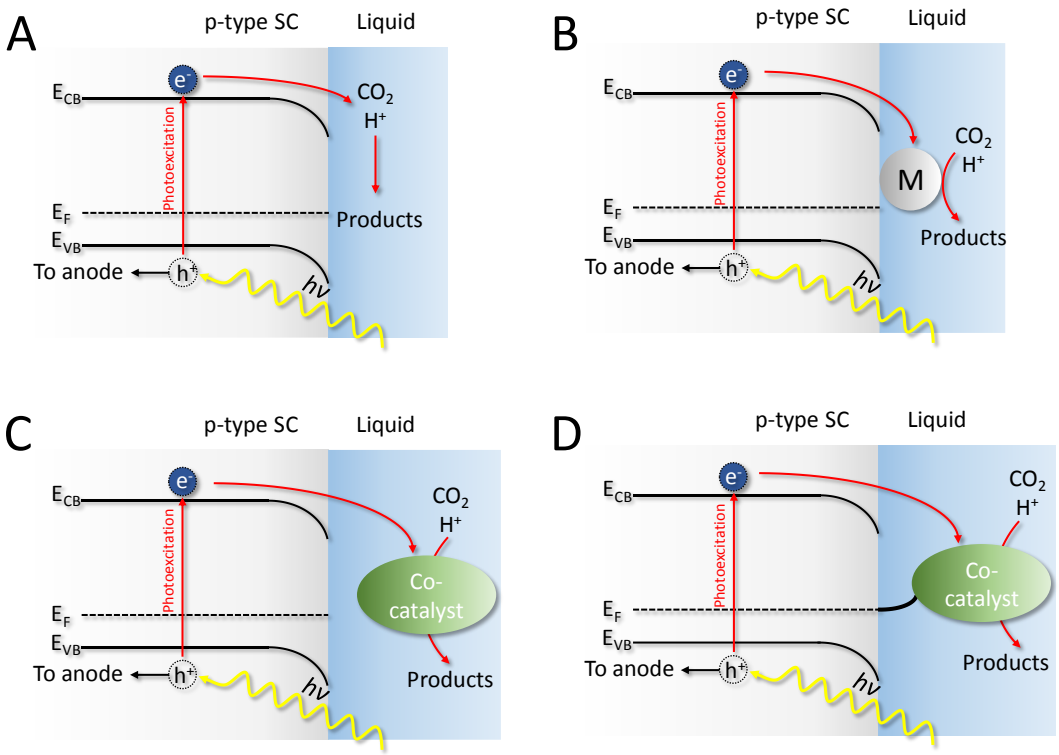

Fig. 11: Schematic diagrams of four different schemes for PEC-assisted CO_2/H^+ reduction on a p-type SC photocathode: heterogenous catalysis on a SC electrode, (B) heterogeneous catalysis on a metal-decorated SC electrode, (C) homogeneous catalysis through a SC/co-catalyst junction and (D) heterogeneous catalysis on a co-catalyst-decorated SC electrode [9].

Another major category of co-catalysts comprises molecular species that can be either present in the electrolyte or anchored to the SC surface. Metal complexes of ruthenium [120], iron [121] and copper [122] are the most well-studied examples. Furthermore, small organic species were also studied, of which one of the most prominent examples is pyridine, which was already used in conjunction with p-GaP for the PEC reduction of CO_2 [123].

CPs are also attractive candidates to act as co-catalysts, because CP-based nanocomposites can be prepared via mild synthetic routes and the polymer structure can be tailored to fit to the requirements of the given application (e.g., higher CO_2-adsorption capacity, added molecular catalysts, etc.) [60,61].

2.5.4 Synthesis of conducting polymer/inorganic semiconductor composites

CP/SiC systems were investigated during my doctoral research, therefore the applicability of CPs as co-catalysts is demonstrated here through the example of various CP/SiC systems, taken from the literature. In this vein, CP/SiC nanocomposites were already synthesized using various CPs, such as PANI [124–127], PPy [128–131], and poly(3-thiophene-acetic-acid) [132]. There are two common attributes in these studies: the nanohybrids were synthesized by chemical polymerization, and the PEC properties of these nanocomposite materials have not been explored yet. Importantly, chemical polymerization methods always lack the precise control over the structure and morphology of the hybrid, although the well-defined structure and morphology are prerequisite to obtain synergistic activity [90]. Thus PC [133] electrochemical [70], and PEC [71] deposition of CPs on the SC surface offer much better alternatives (**Fig. 12**). CP/SiC nanohybrids have not been studied as photoelectrodes, therefore the exploration of their PEC properties, along with the possible synergistic behavior toward the PEC reduction of CO_2, is a very interesting research topic, providing insights into nanocomposite design.

Photocatalysis, occurring at the SC/electrolyte interface is a broadly studied phenomenon [17], mostly in the field of solar energy conversion and environmental remediation. On the other hand, much less attention is devoted to the utility of this phenomenon as a synthesis tool. Biomass valorization using photocatalysis is a promising example [134], but other areas still have to be explored. The limited number of studies on the PC synthesis of hybrid inorganic/organic nanocomposite materials is indeed surprising,

considering the photoactivity of both components. The most important beneficial feature of this approach is that the CP is formed *in situ*, on the surface of the inorganic SC nanostructure, thus bringing the two SCs into intimate contact [135].

The pioneering studies were performed on colloidal-, or nanoparticulate TiO_2 slurries [136,137], using pyrrole as the monomer. In these cases, the nanoparticles were dispersed in the monomer-, and supporting electrolyte-containing solution. The dispersion was illuminated by UV light under continuous stirring and saturation with O_2 (which acted as an electron scavenger). The photogenerated holes oxidized the monomer molecules, dissolved in the polymerization solution. Thus, first oligomers were formed, and then a thin PPy film was subsequently deposited on the surface of the SC (schematic illustration of the synthesis procedure is shown in **Fig. 12A**). Note that the success of this method depends on the valence band energy level (E_{VB}) of the SC and the oxidation potential of the monomer species, present in the solution. Follow-up studies demonstrated the suitability of this method with other SCs, such as CdS [133], CdTe [133], (CdSe@ZnS) [138], and polymers (e.g., PEDOT) [139]; as well as yielded further mechanistic details [140]. Finally two sophisticated variants of this approach are also presented here: PEC polymerization (where external electrical bias is employed instead of chemical electron scavenger) [90,141]; and the PC deposition of CdS on the surface of poly(3-hexylthiophene) (in this case the photoactivity of the CP was exploited) [142].

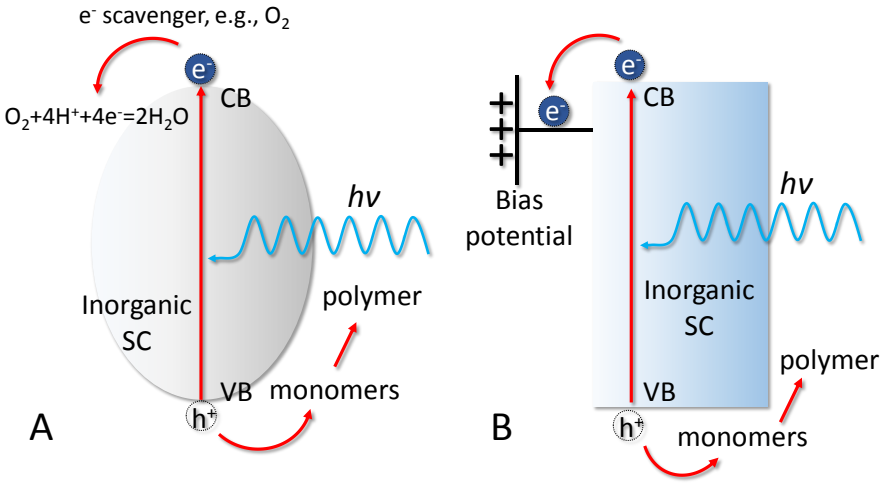

Fig. 12: Schematic illustration of (A) PC and (B) PEC deposition of CPs on the bare SC surface, respectively.

PEC deposition (**Fig. 12B**) differs from photocatalytic polymerization in two aspects: nanoparticles are immobilized on the working electrode's surface, and external bias potential is applied, which role is to drain the photogenerated electrons to the external circuit, thus suppressing recombination. Note that the applied potential is not positive enough to oxidize the monomer molecules (unlike in the case of electrochemical deposition), its only role is to suppress recombination [90]. Here, similarly to the PC deposition method, the photogenerated holes are the ones, oxidizing the monomer molecules.

3. MOTIVATION AND AIMS

The investigation of the synthesis and electrochemical properties of CPs and their nanocomposites in our research group and its predecessor one dates back to the end of the 1980s. However, the applicability of these materials in solar fuel generation processes were not studied, not just in our group, but in the literature in general. When I've started my PhD studies in 2013, our first goal was to merge the knowledge, accumulated over the years in the Electrochemistry Research Group at the University of Szeged and the PEC know-how gathered by my supervisor, Csaba Janáky, during his postdoctoral studies at The University of Texas at Arlington ***to study the fundamental PEC behavior of CP photocathodes and their applicability in the PEC reduction of CO_2***. After understanding the main factors dictating the enhanced PEC activity toward the PEC reduction of CO_2 and identifying the main drawbacks of using only the pristine CPs as photoelectrodes, our focus has turned to CP based nanocomposite electrodes. Such hybrids might eliminate some of the experienced disadvantages, thus resulting in improved PEC properties. Two directions were examined. Flow chart, summarizing the aims of my dissertation are presented in **Scheme 1**.

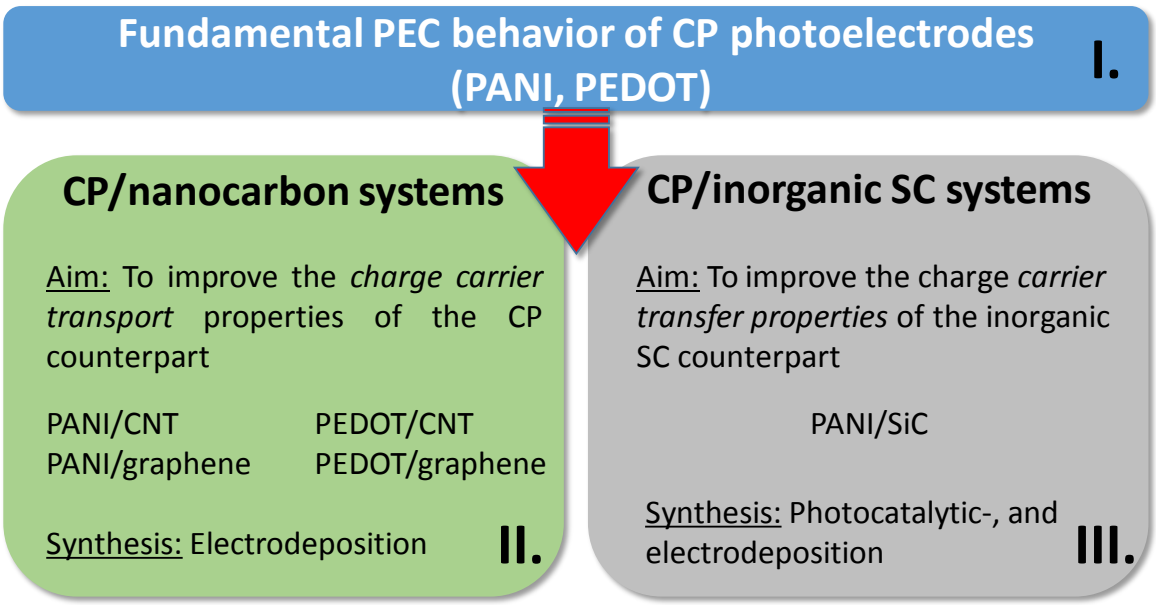

Scheme 1: Flow chart, summarizing the aims of my dissertation.

To improve the charge carrier transport properties, CP/nanocarbon electrodes were synthesized. Our goal was to develop a synthesis procedure through which the

composition of the nanohybrids can be tuned. As a next step, we wanted to study the effect of composition on the PEC behavior and the applicability of these composites in PEC CO_2-, and H^+ reduction processes. Our further object was to explore the effect of the nanocarbon network on the conductivity, light absorption properties and finally, on the amount and distribution of the formed products.

To improve the charge carrier transfer properties of SiC PANI was studied as a co-catalyst on the surface of the SiC nanoparticles. Our goal was to synthesize such nanocomposites by applying both photocatalytic-, and electrochemical deposition techniques, which result in an electroactive CP coating on the surface of SiC. As a next step, we wanted to investigate the PEC properties of the synthesized nanocomposites, along with their applicability as photoelectrodes to the PEC reduction of CO_2.

4. CHEMICALS AND EXPERIMENTAL TECHNIQUES

4.1 Materials

Spray-coating

- Multi-walled carbon nanotubes (MWCNTs) (Cheap Tubes USA)
- Graphene powder (Elicarb®)
- Silicon carbide (SiC; M_r = 40.11; U.S. Research Nanomaterials Inc., $d_{average} \approx 50$ nm)
- Isopropanol (C_3H_8O; M_r = 60.10; VWR)
- Ethanol (C_2H_6O; M_r = 46.07; absolute; Sigma-Aldrich)
- Compressed air (20.5 % O_2, 79.5% N_2; Messer)

All materials were of analytical grade and used without further purification.

Synthesis of CP thin films and nanocomposites

- Aniline monomer ($C_6H_5NH_2$; M_r = 93.13; Sigma-Aldrich)
- 3,4-ethylenedioxythiophene monomer ($C_6H_6O_2S$; M_r = 142.18; Sigma-Aldrich)
- Pyrrole monomer (C_4H_5N; M_r = 67.09; Sigma-Aldrich)
- N-methylaniline monomer ($C_6H_5NHCH_3$; M_r = 107.15; Sigma-Aldrich)
- Sulfuric acid 95% (H_2SO_4; M_r = 98.08; Sigma-Aldrich)
- Sodium dodecyl sulfate (SDS - $NaC_{12}H_{25}SO_4$; M_r = 288.37; Alfa Aesar)
- Oxygen 99.995% (O_2; M_r = 32.00; Messer)

All materials were of analytical grade and used without further purification. All monomers were freshly-distilled prior to each use. Solutions were prepared using ultrapure deionized water (Millipore Direct Q3-UV, 18.2 MΩ cm).

(Photo)electrochemical characterization and product quantification

- Sodium sulfate (Na_2SO_4; M_r = 142.04; VWR)
- Sodium hydrogen carbonate ($NaHCO_3$; M_r = 84.01; VWR)
- Nitrogen 99.995% (N_2; M_r = 28.02; Messer)
- Carbon dioxide 99.995% (CO_2; M_r = 44.01; Messer)
- Helium 99.9999% (He; M_r = 4.00; Messer)
- Argon 99.999% (Ar; M_r = 39.95; Messer)

- Deuterium oxide 99.9 atom% (D_2O; M_r = 20.03; Sigma-Aldrich)

All materials were of analytical grade and used without further purification. All solutions were prepared using ultrapure deionized water (Millipore Direct Q3-UV, 18.2 MΩ cm).

4.2 Experimental techniques

4.2.1 Electrode preparation

Spray-coating

The CNT-containing and the graphene-containing dispersions (the concentration of both dispersions were c = 2 mg ml^{-1}) were spray-coated on a preheated GC electrode surface (which were polished on 50 nm alumina powder prior to spray-coating), employing an Alder AD320 type airbrush and a homemade spray-coater robot (**Fig. 13**) operated with 1 bar compressed air pressure.

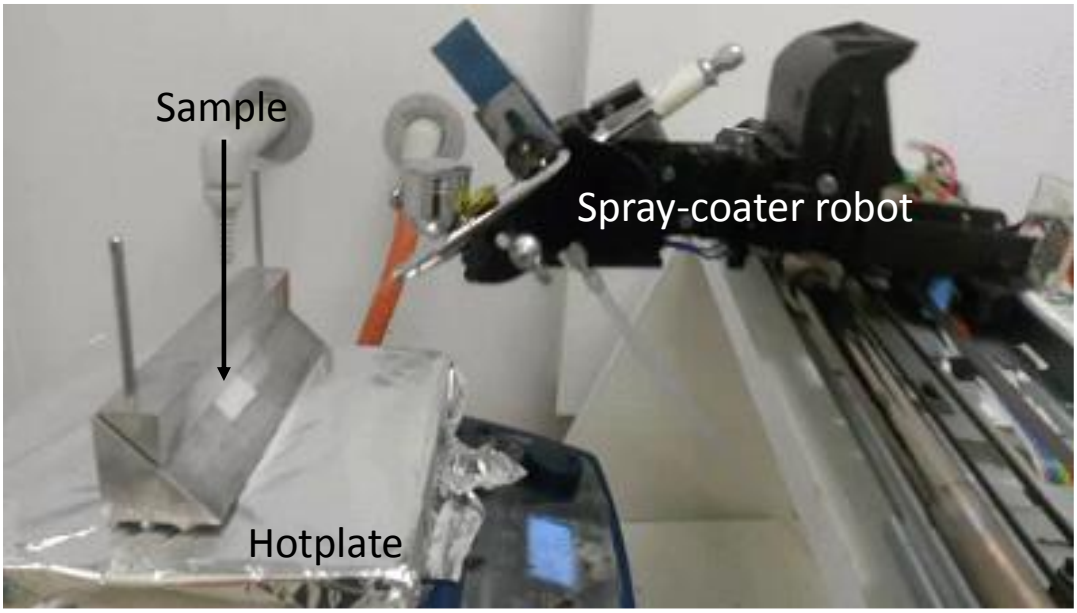

Fig. 13: Photo of the spray-coater robot, used to prepare all nanocarbon-, and SiC-modified electrodes.

The electrodes were heated on a hotplate to 140 °C for the coating process. After spray-coating, the thin films were heat treated in an oven at 180 °C for 30 minutes in the case of the graphene layers and for 1 hour in the case of the CNT layers. This treatment removed the residual traces of the solvent and enhanced the adhesion of the nanocarbon layers to the underlying electrode surface. The precise amount of spray-coated

nanocarbons was monitored by a Mettler Toledo XPE-26 type analytical microbalance. The electrochemical surface area of each nanocarbon-coated electrode was measured prior to the polymerization procedure. After registering the cyclic voltammograms for the various nanocarbon films, the charge capacitance values were calculated and normalized by the value, measured for a 1 cm^2, smooth GC electrode. The results are presented in **Fig. 14** by plotting the normalized charge capacitance versus the spray-coated mass. It can be concluded that the measured charge capacitance increases linearly with the spray-coated mass. Additionally, the charge capacitance values are higher in the case of the GC/CNT layers.

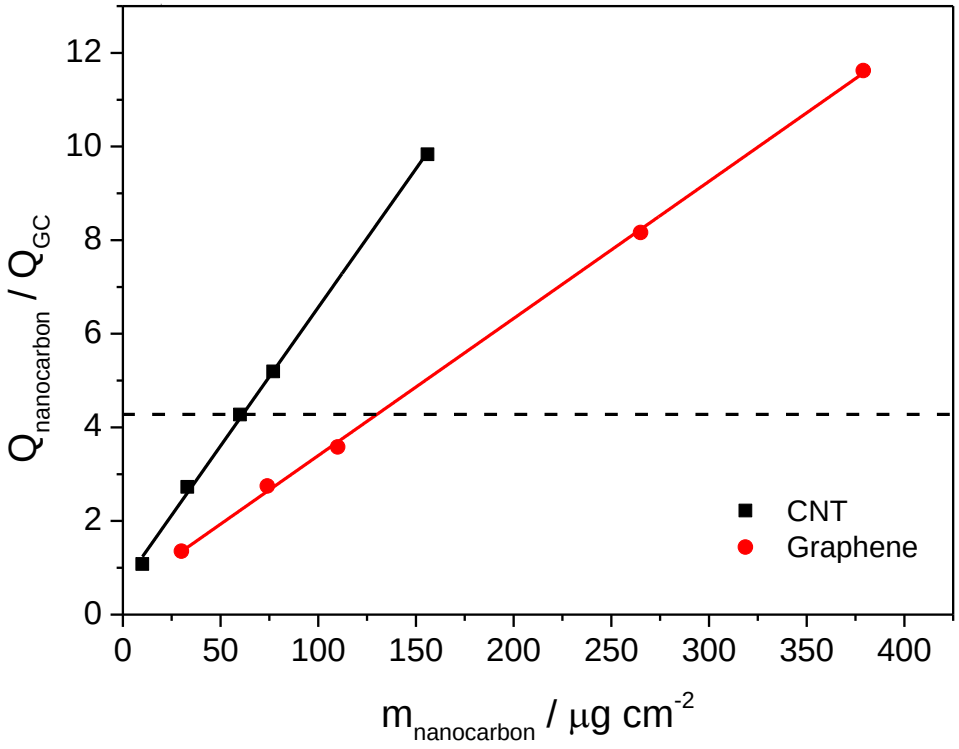

Fig. 14: Normalized charge capacitance vs. spray-coated mass curves calculated for each graphene/GC (black squares) and CNT/GC layer (blue dots). The interception of the fitted linears with the dashed line indicates the mass, which was used during measurements when the electrochemically active surface of the nanocarbons were set to be identical.

There are two main differences between the protocols, applied for the nanocarbons, and the one, used in the case of the SiC nanoparticles. First, the SiC nanoparticles were dispersed in isopropanol (c = 10 mg ml^{-1}) instead of ethanol, and the subsequent heat treatment was omitted for SiC. The mass of the spray-coated SiC was 0.4 mg cm^{-2} for each sample (studies were carried out between 0.1 – 1.0 mg cm^{-2} and 0.4 mg cm^{-2} was found to be optimal).

For the electrochemical characterizations, the nanocomposite samples, prepared by photocatalytic deposition were spray-coated on a Au electrode surface. The dispersion contained 2 mg ml^{-1} nanocomposite (or pristine SiC) and 25% aqueous solution of Nafion® ionomer. The mass of the material on the electrode surface was approximately 2 mg cm^{-2} in each case.

Electrodeposition

All electrochemical measurements were performed using a Metrohm Autolab PGSTAT302 type potentiostat/galvanostat. The electropolymerization of CPs was carried out in a classical three-electrode cell setup, including a Ag/AgCl/3 M NaCl as reference electrode (+0.197 V vs. SHE) and a Pt sheet as a counter electrode. A Au sheet or a GC electrode (bare- or covered with either the nanocarbons or with SiC) was used as working electrodes. Two types of electrodeposition techniques were employed to deposit the CPs on the various electrode surfaces, which were tailored to each monomer.

Aniline was electropolymerized *potentiodynamically* from a solution containing 0.2 M aniline monomer and 0.5 M H_2SO_4. During potentiodynamic deposition, the potential of the working electrode is scanned with a constant rate between two limits, while the current density is measured. When the potential reaches the necessary overpotential, the oxidation of the monomer molecules starts and a thin CP layer forms on the working electrode surface, while at negative enough potentials the deposited CP layer gets reduced. The thickness of the CP can be increased by running consecutive cycles. The polymerization of aniline was performed by scanning the potential between −0.2 V to 0.9 V at 100 mV s^{-1} scan rate. The thickness of the deposited CP layers was controlled by the polymerization charge density in each case. N-methylaniline was electropolymerized by applying the exact same methodology. In some cases (PANI/SiC nanocomposites and the corresponding bare PANI photoelectrodes), the polymerization charge density was so low, that the contribution of charging the double layer to the overall charge seriously affected the amount of the deposited polymer under the coulometric conditions. To avoid this issue, the GC and SiC-coated GC electrodes were pretreated at E = 0.6 V for 120 s.

PEDOT was electrodeposited employing *potentiostatic* electropolymerization, while PPy was electrodeposited utilizing *galvanostatic* deposition. By applying such static

techniques, either the potential- or the current density is maintained at a constant value, while the current density or potential is measured. Importantly, the amount of the deposited polymer can be controlled precisely. Indicating if the deposition parameters are chosen carefully, side-reactions (such as water oxidation, irreversible overoxidation of the monomer, etc.), potentially damaging the deposited polymer can be fully avoided. PEDOT was electropolymerized from a solution containing 0.02 M EDOT monomer and 0.05 M SDS by applying E = 0.9 V constant potential. PPy was electrodeposited from a solution containing 0.1 M pyrrole monomer and 0.05 M SDS by applying j = 3 mA cm^{-2} current density. Thickness of the deposited polymers were controlled by varying the polymerization charge density.

To ensure the proper wetting of the nanocarbon-modified electrodes, they were pretreated prior to electropolymerization by cycling the potential between 0 V and 0.5 V 10 times, applying a sweep rate of 50 mV s^{-1}.

Photocatalytic deposition

A solution (V_{total} = 5 ml), containing 0.2 M aniline, 10 mg SiC nanoparticles, and 0.5 M H_2SO_4 was prepared for each synthesis. The slurries were put in a quartz or Pyrex ® photoreactor depending on the type of illumination (Pyrex® absorbs all the components of the irradiating light below 300 nm, while quartz transmits the whole spectra). The dispersion was constantly stirred and saturated with O_2 during the synthesis and illuminated by a 300 W Hamamatsu L8251 Hg-Xe arc lamp. Time of irradiation was varied (5, 10, 30 and 60 minutes). After the nanocomposite synthesis, the samples were centrifuged with a VWR 1814 centrifuge, washed, and centrifuged two more times. Finally, the samples were dried under vacuum at 80 °C for 4 hours.

4.2.2 Physical characterization

Raman spectroscopy

Raman spectroscopy was employed to verify the formation of the CP thin films and the CP-based nanocomposites. Furthermore, studying the Raman spectrum of a composite material, a specific interaction can be suspected from the shift of the bands characteristic to the neat components [143,144]. Raman spectra were recorded using a DXR Raman

microscope (Thermo Scientific, Waltham, USA) using a λ = 532 nm green laser, operating at typically 5 − 10 mW laser power.

Fourier-transform infrared spectroscopy (FT-IR)

ATR-FT-IR spectroscopy was used to confirm the formation of the CP-based nanocomposites. Since several vibrations appear exclusively on either the Raman or FT-IR spectra, due to the different selection rules, these were employed as complementary techniques. ATR-FT-IR studies were performed using a Bio-Rad Digilab Division FTS-65A/896 FT-IR spectrometer, equipped with a Harrick's Meridian® SplitPea single-reflection diamond ATR accessory. Infrared spectra were recorded between 4000 and 400 cm^{-1}. All spectra are an average of 256 interferograms with 4 cm^{-1} optical resolution.

Vibrational spectroscopic changes upon CO_2 adsorption were monitored by FT−IR spectroscopy using an Agilent 670 Fourier-transform infrared spectrometer equipped with a Harrick's Praying Mantis™ Diffuse Reflection Accessory. All infrared spectra were recorded between 6000 and 600 cm^{-1}, at 2 cm^{-1} optical resolution, by averaging 16 interferograms. The background spectra were recorded at room temperature after a 60 minutes pretreatment in He, at 200 °C. Subsequently, the chamber was purged with CO_2 and a series of IR spectra were recorded with increasing contact time. Finally, He was purged to the chamber again, and IR spectra were recorded.

Scanning electron microscopy (SEM)

SEM was employed to characterize the morphological features of both the synthesized nanohybrids, and their constituents. Furthermore, this technique was used to estimate the thickness of CPs in the case of PANI/CNT and PEDOT/CNT nanocomposites. A Hitachi S-4700 field emission scanning electron microscope was used for the SEM measurements, operating at an accelerating voltage of 10 kV.

Transmission electron microscopy (TEM)

TEM images were used to estimate the average size of the SiC nanoparticles, CNTs and graphene flakes. Moreover, this tool was applied in conjunction with SEM to prove that CPs were deposited on the surface of the nanoparticles, nanotubes or nanoflakes. The thickness

of PANI was estimated in the case of the photocatalytically synthesized PANI/SiC nanocomposites. Size distribution histograms were constructed from at least 300 measurement points. TEM images were taken by using a FEI Tecnai G^2 X-Twin type instrument, operating at an accelerating voltage of 200 kV.

CO_2-Adsorption studies

Carbon dioxide adsorption on the polymer films was monitored by quartz crystal microgravimetry (QCM) technique using a Stanford Research Systems QCM 200 instrument. The polymer films were deposited using a charge density of 100 mC cm^{-2} on gold-coated quartz crystal (5 MHz resonance frequency). The polymer films were first incubated in N_2 for 30 min; then the atmosphere was periodically changed from N_2 to CO_2 and vice versa every 5 min in a sealed cell. The mass changes were calculated from the measured frequency changes using the calibration constant of the crystal.

Thermogravimetric analysis

TGA was used in conjunction with TEM to quantify the amount of CP, deposited on the surface of the SiC nanoparticles by varying the time of synthesis. Thermoanalytical measurements (TG & dTG) were performed on a TA Q800 TGA instrument. In a typical experiment, 3-5 mg of the samples were heated in synthetic air (20.5 % O_2 in N_2) from room temperature to 800 °C with a heating rate of 10 °C/min.

Kelvin probe microscopy-coupled ambient UV photoelectron spectroscopy

Measurements were performed using the KP Technology APS04 instrument [145]. First, the contact potential difference (CPD) was measured between the sample and the Kelvin-probe after electric equilibrium was reached. A d = 2 mm diameter gold alloy-coated tip was vibrated above the sample surface at a constant height (≈ 1 mm) and amplitude (0.2 mm), with a constant frequency (70 Hz). Ambient pressure UV photoelectron spectroscopy (UV–APS), measurements were carried out with a stationary Kelvin-probe tip. The sample surface was illuminated with a 5 mm spot sized, variable energy UV light source. The UV light generates an electron cloud from the SC if $h\nu \geq E_{VB}$. Under atmospheric conditions, this is followed by the formation of secondary ions (N_2^-, O_2^-). These ions can be then collected

by the Kelvin-probe tip; thus, a current is measured. In the case of semiconductors, a cube-root dependence of this current was found from the excitation energy [145]. The intersection of the baseline and the rise in the cube root of the photoemission current can be then related to the VB of a given SC. Prior to measurements, the Fermi level of the gold alloy-coated tip was determined, by measuring the Fermi level (E_F) of a Ag target ($E_{F,\,Au\text{-}tip}$ = 4.67 eV). These two techniques were used to construct the band diagram of PANI and PEDOT and their nanocomposites.

4.2.3 (Photo)electrochemical measurements

Linear sweep photovoltammetry

During linear sweep photovoltammetry measurements, the potential of the working electrode is scanned with a constant speed to one direction in a potential window, while the surface of the working electrode is irradiated periodically (an example is shown in **Fig. 15A**). Linear sweep photovoltammetry is a very informative and the most basic PEC characterization technique to the characterization of SC photoelectrodes. The most important advantages and parameters which can be gleaned from such measurements:

- The momentary value of the dark-, and photocurrent can be visualized on one plot.
- The type of SC can be immediately suggested from the sign of the photocurrent; cathodic photocurrents – p-type SC, anodic photocurrents – n-type SC.
- The flatband potential can be obtained from the onset of the photovoltammogram, which can be correlated to E_{VB} in the case of a p-type SC and to E_{CB} in the case of an n-type SC (**Fig. 15B**) [146].
- The shape of the transients can imply if significant recombination occurs on the SC/electrolyte interface (spikes).

The easiest tool for the investigation of PEC processes. Two photovoltammograms are recorded using the same sample, one in the absence of the targeted reactant (e.g., CO_2) and one in the presence of it. If the investigated photoelectrode shows any PEC activity toward the conversion of the substrate, higher photocurrents are measured in the latter case. This excess in the harvested photocurrents can be correlated to the selective oxidation/reduction of the substrate molecules, however these observations must be supported by product detection results. Owing to these unequivocal advantages, linear

sweep photovoltammetry experiments are always among the first ones that are carried out, before sophisticated PEC measurements can be designed.

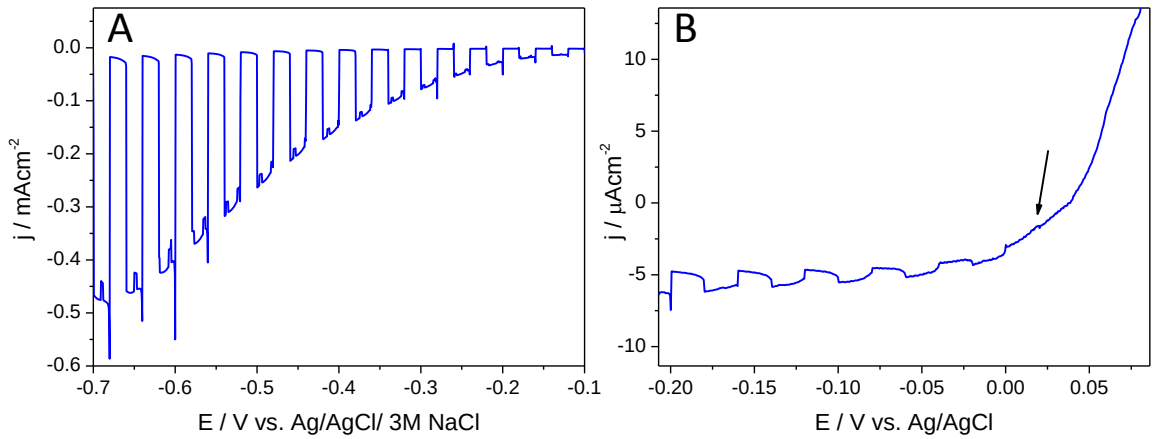

Fig. 15: (A) An example to a linear sweep photovoltammogram, recorded for a p-type SC and (B) inset, taken from (A), a black arrow shows the place of the onset potential on the photovoltammogram.

All photoelectrochemical measurements were performed using a Metrohm Autolab PGSTAT302 type potentiostat/galvanostat. Linear sweep photovoltammograms were recorded in a sealed, custom-designed one-compartment, three-electrode quartz cell. The working electrode was always covered with the CP or nanocomposite to be examined, while a Pt sheet and Ag/AgCl/3M NaCl were employed as the counter-, and reference electrodes respectively. Two light sources were applied during these measurements:

- A Newport LCS-100 type *solar simulator* operated at full output. The solar simulator source was placed 5 cm away from the illuminated working electrode surface (200 mW cm^{-2} flux), which was irradiated through a quartz window.
- A Hamamatsu L8251 300 W *Hg-Xe arc lamp*, operated at full output. The lamp was placed 5 cm away from the illuminated working electrode surface (180 mW cm^{-2} flux), which was irradiated through a quartz window. The irradiation spectra of both lamps are presented in **Fig. 16**.

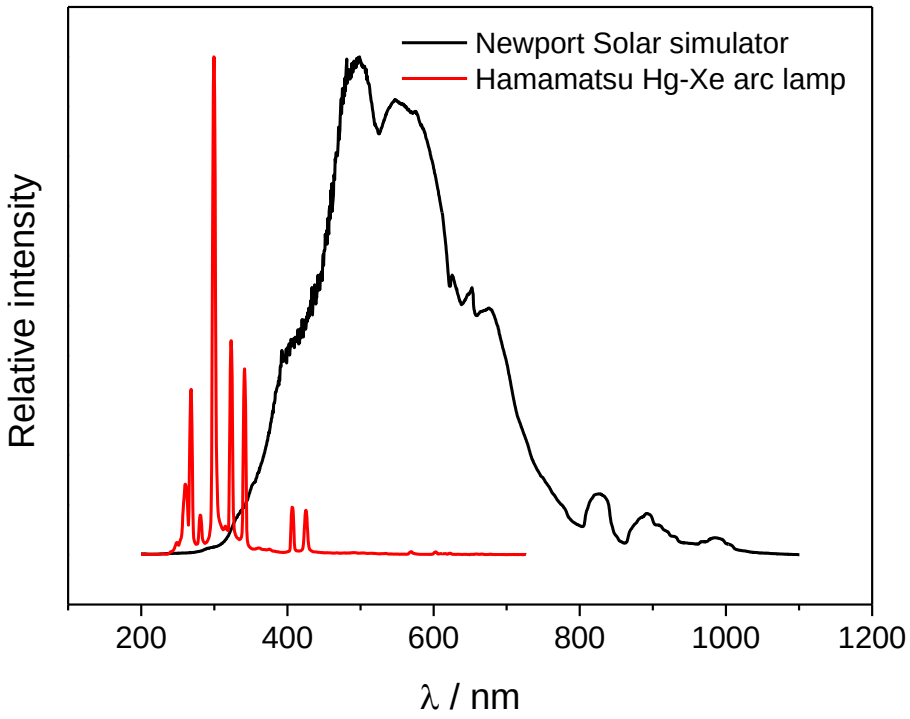

Fig. 16: Irradiance spectra of the lamps, employed in all PEC experiments in this work.

The sealed cell was saturated with Ar, N_2 or CO_2 as needed, by 30 minutes of continuous bubbling prior to each measurement. The gas-flow was continuous above the saturated electrolytes during the measurements. To compare the results, obtained from the N_2-, and CO_2- saturated electrolytes, all measurements were carried out at the same pH value, which was ensured by using two types of electrolytes: 0.1 M Na_2SO_4 saturated by N_2 and 0.1 M $NaHCO_3$ saturated by CO_2, respectively (pH ≈ 7.00). If the PEC H^+ reduction was studied, 0.1 M Na_2SO_4 was used as an electrolyte, which was saturated by Ar. Before the PEC measurements, a potentiostatic pretreatment procedure was applied for three minutes, to make sure that the given CP is in its fully reduced state. The pretreatment was applied at E = −0.4 V in the case of PANI or PANI-containing nanocomposites and at E = −0.9 V in the case of PEDOT or PEDOT-containing nanocomposite electrodes. Photovoltammograms were recorded using a slow potential sweep (2 mV s^{-1}) in conjunction with periodically interrupted irradiation (0.1 Hz).

Due to the slow surface kinetics, observed in the case of bare SiC (see **Fig. 3** for further details), photovoltammograms were recorded using even a slower potential sweep (0.5 mV s^{-1}) and chopping frequency (0.05 Hz), even in the case of the bare CP layers and CP/SiC nanohybrids.

Incident photon-to-current efficiency

Incident photon-to-current efficiency (IPCE) or external quantum efficiency (EQE) is one of the most important diagnostic figures of merit for PEC systems. It describes the photoelectrons collected per the incident photon flux as a function of the illumination wavelength (Eq. 1). IPCE combines the efficiencies of three fundamental processes, involved in photoelectrochemistry [147]:

- photon absorptance – the fraction of the electron-hole pairs generated per incident photon flux,
- transport of the photogenerated charge carriers toward the electrode/electrolyte interface and finally,
- efficiency of the interfacial charge transfer.

$$IPCE = EQE = \eta_{e^-/h^+}\eta_{transport}\eta_{interface} = \frac{Number\ of\ photoe^-/t}{Incident\ photon\ flux} \times 100\% \qquad (1)$$

In a PEC system, IPCE data are usually derived from chronoamperometric measurements. A constant bias potential is applied to the working electrode (typically at which the photocurrent is high enough, but the investigated system is still stable) followed by the periodic illumination of its surface with a monochromatic light at various wavelengths. To translate Eq. 1 to the language of experiments, IPCE corresponds to the photocurrents, derived from the chronoamperometric curve (converted to an electron rate) versus the rate of incident photons, converted from the calibrated power of the employed light source. In our setup a Si detector was used for this purpose, prior to each measurement.

Several useful parameters can be derived from IPCE measurements:

- The wavelength-range, in which the studied sample is photoactive – ideal if this window and the maximum of the curve overlaps with the absorption spectrum of the material,
- device efficiency in terms of “electrons out per photons in”, also considering the spectral variation of incident photons at each energy,
- the bandgap of the investigated SC by fitting a linear to the cutoff-region of the IPCE curve and

- the total solar-to-electron-conversion efficiency by integrating the IPCE data over the solar spectrum.

IPCE measurements were performed on a Newport Quantum Efficiency Measurement System (QEPVSI-B) in a single compartment, three-electrode quartz electrochemical cell. Two wavelength-ranges were applied, depending on the photoactivity window of the investigated CPs: 250 − 500 nm in the case of PANI and its nanocomposites, and 350 − 800 nm in the case of PEDOT and its nanocomposites. The resolution was kept at $\Delta\lambda$ = 10 nm. Measurements were carried out in either 0.1 M $NaHCO_3$ saturated with CO_2 or in 0.1 M Na_2SO_4 saturated with Ar.

Electrochemical impedance spectroscopy

The effect of the composition of the nanocomposites on the electric properties was studied by electrochemical impedance spectroscopy (EIS). Electrochemical impedance spectra of all investigated photoelectrodes were recorded in a 1 M Na_2SO_4 solution saturated with Ar, at E = −0.4 V (PANI and PANI-based nanocomposites) or at E = −0.9 V potential (PEDOT and PEDOT-based nanocomposites), in the 10 Hz to 100 kHz frequency range, using a sinusoidal excitation signal (10 mV RMS amplitude). Similar pretreatment procedure was applied to each layer as the one during the photovoltammetry experiments. Modulus weighted fitting was performed using the Nova Software of the Autolab Instrument.

EIS data were quantified by fitting an equivalent circuit to the experimental data (**Fig. 17**). The circuit consists the following elements: an equivalent solution resistance (R_s), a charge transfer resistance (R_{ct}), a Warburg diffusion element, attributable to SO_4^{2-} anions moving in and out of the CP layer (measurements were conducted in 1M Na_2SO_4), a Faradaic pseudocapacitance (C_F) assigned to the polymer film, and a double-layer capacitance (C_{dl}) [148–151].

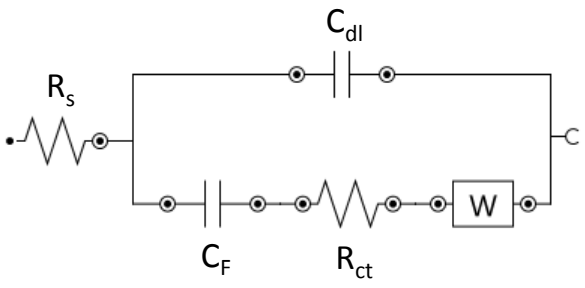

Fig. 17: Equivalent circuit fitted to the measured EIS data.

Fast current transient measurements

To study the charge carrier recombination process occurring at the SC/electrolyte interface, transient PEC measurements were performed [152,153]. During these measurements, the photocurrent was traced at various cathodic potentials, after the illumination was turned on. To fit the most precise model to the experimental data (i.e., to detect even the slightest change as fast as possible) the resolution of the detection must be as high as possible. In our current instrumental setup, the highest possible resolution is around 50 µs. An example to a transient photoresponse is presented in **Fig. 18**. A transient photoresponse can be divided in two parts: i) a fast increase, where the maximum photocurrent evolves, and ii) a slower decaying section, where the photocurrent decreases up to point where it reaches its steady-state value. The first part is related to the hole-transport through the electrode assembly, while the second one can be correlated to the surface recombination process [50].

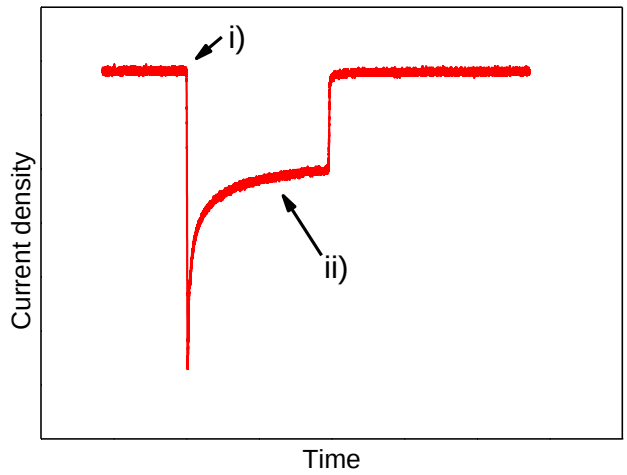

Fig. 18: A typical transient photoresponse. i) and ii) shows the two parts to which the photoresponse can be divided.

To quantify these observations, the experimental data was fitted, and time constants were determined for all systems. The transient photoresponse curves can be modeled by a simple binomial exponential function [154]:

$$j = j_0 + A_1 \cdot \exp\left(-t/\tau_1\right) + A_2 \cdot \exp\left(-t/\tau_2\right) \quad (2)$$

The first exponential is related to the transport of the majority carriers (in all cases presented in my dissertation these are the holes) through the electrode assembly, which is

characterized by a time-constant called τ_1. The second exponential is corresponded to the surface recombination process, which is characterized by an other time-constant, τ_2. The two pre-exponential factors provide numerical information about two extreme situations. A_1 gives the value of the maximum harvestable photocurrent, when no recombination occurs, and A_2 gives the harvestable photocurrent, when maximal recombination occurs.

Fast transient measurements were performed in the same, custom-designed, sealed three-electrode quartz cell as the one which was used during the linear sweep photovoltammetry experiments. Measurements were carried out in both 0.1 M Na_2SO_4 saturated with Ar or N_2 and in 0.1 M $NaHCO_3$, saturated with CO_2 as needed in a potential regime, ranging from E = −0.3 V to E = −0.6 V with a resolution of ΔE = 0.05V. The duration of illumination was two seconds, while the current was traced for four seconds.

4.2.4 Product detection and quantification

Long-term PEC measurements were carried out in a sealed two-compartment cell ($V_{solution}$ = 40 cm^3) where the compartments were separated by a Nafion117® membrane. The working electrode was a CP, or a CP-based nanocomposite modified GC (A = 4 cm^2) or Au (A = 4 cm^2). A Pt sheet was applied as a counter, and a Ag/AgCl/3 M NaCl as a reference electrode. The applied potential was E = −0.4 V (if PANI was the investigated CP) or E = −0.9 V (in the case of PEDOT) during the measurements. The electrodes were pretreated at the same potential for 300 s without illumination to ensure, that the CPs are in their fully reduced state and to minimize dark current during the measurement. Measurements were carried out in both 0.1 M Na_2SO_4 saturated with Ar or N_2 and in 0.1 M $NaHCO_3$, saturated with CO_2 as needed. During the reaction, gas samples were taken at 30, 60, 90, and 120 minutes via an on-line detection system, which was coupled to the cathode compartment of the cell. Liquid phase aliquots were taken from the cathode compartment of the cell at the same time as gas phase samples with a Hamilton-syringe, via a septum-sealed hole on the top of the cell.

Gas chromatography equipped with a dielectric barrier discharge ionization detector

Gas phase samples were analyzed via an on-line detection system, using a gas chromatograph, equipped with a dielectric barrier discharge ionization detector (BID). The use of an on-line system is essential to obtain accurate quantities and Faradaic efficiencies,

especially if H_2 is among the formed products. Schematic illustration of the whole on-line setup is presented in **Fig. 19**.

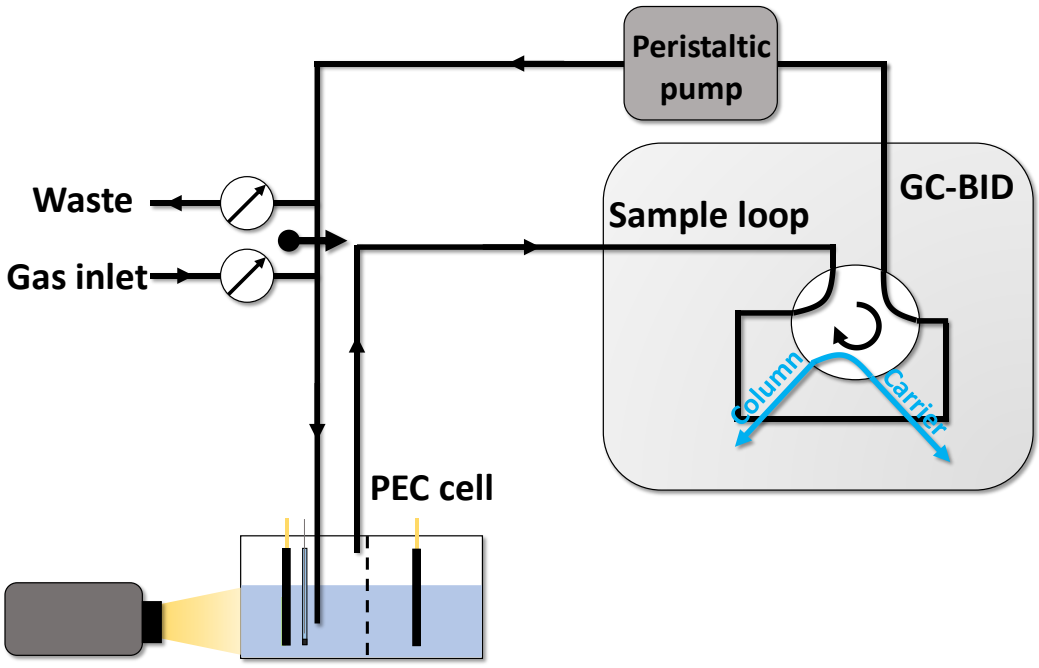

Fig. 19: Schematic illustration of the GC-BID on-line setup used during the long-term photoelectrolysis experiments.

As a first step, the PEC cell must be saturated with either Ar or CO_2 as needed. To achieve this, both stopcocks are in an open position and the needle valve is closed. In this way, the electrolyte and the gas chamber above the solution can be saturated, while the waste can be flushed to a beaker, filled with water. After purging the solution for at least 30 mins, stopcocks are closed, and the needle valve is opened (this results in a closed loop). As a next step, the measurement can be started and prior to sampling, the gas in the closed loop has to be circulated by a peristaltic pump. To inject the sample, the 6-port external volume sample injector automatically turns to the second position and at the same time the sample is automatically injected to the column.

Products in the gas phase were separated with a ShinCarbon ST column and analyzed with a Shimadzu GC-2010 Plus gas chromatograph equipped with a BID detector. This type of detector utilizes atmospheric non-equilibrium plasma. The main advantage of employing a BID detector compared to FID or TCD constructions are:

- a much more stable baseline can be obtained,

- superior sensitivity to FID with respect to chlorine-containing samples and alcohols (**Fig. 20A**),
- BID achieves at least 100 times the signal/noise ratio of TCD for inorganic gases and finally,
- H_2 can be detected simultaneously with other gas phase products, which is not possible with FID or TCD constructions (**Fig. 20B**) [155].

This latter feature is very important from our perspective, because H_2 is always one of the forming products in PEC CO_2 reduction processes, therefore it is possible with this configuration to measure all gas phase products in one sample.

The optimized sampling parameters were the following: carrier gas: helium; oven program: T_{start} = 35°C (2.5 min), ΔT_{ramp} = 20 °C min^{-1}, T_{end} = 270 °C (3 min); injection temperature: T = 150 °C; linear velocity was controlled by the pressure p_{start} = 250 kPa (2.5 min) Δp_{ramp} = 15 kPa min^{-1} p_{end} = 400 kPa (7.5 min); and split ratio: 10. Prior to evaluate the amount of the formed product, calibration measurements were performed, using a gas mixture containing H_2, CO, CH_4 and C_2H_4, in concentrations, ranging from 0.1 V/V% up to 10 V/V%.

Finally, after calculating the amount of the products in the gas phase, Faradaic efficiencies can be obtained using Eq. 3 [8]:

$$FE\% = \frac{Q_{product}}{\Sigma Q} \times 100\% = \frac{n_{product} \times F \times z}{\Sigma Q} \times 100\% \quad (3)$$

where $n_{product}$ is the moles of product evolved, F is the Faraday-constant and z is the number of electrons needed for the formation of the given product. ΣQ can be derived by integrating the chronoamperometric curve, recorded during the long-term photoelectrolysis experiment. Faradaic efficiency is one of the most important figures of merit for a PEC system because it is possible to characterize the investigated photoelectrocatalyst in terms of selectivity. In an ideal system, ΣFE% is close to 100%. However, values below 100% can be measured if i) not a closed-loop system is used for product detection or if ii) the amounts of the formed products are falling to the detection limit (or below) of the given analytical technique and finally, if iii) any side-reaction occurs during the long-term PEC measurement (photocorrosion, side-reactions, which products can't be detected, etc.).

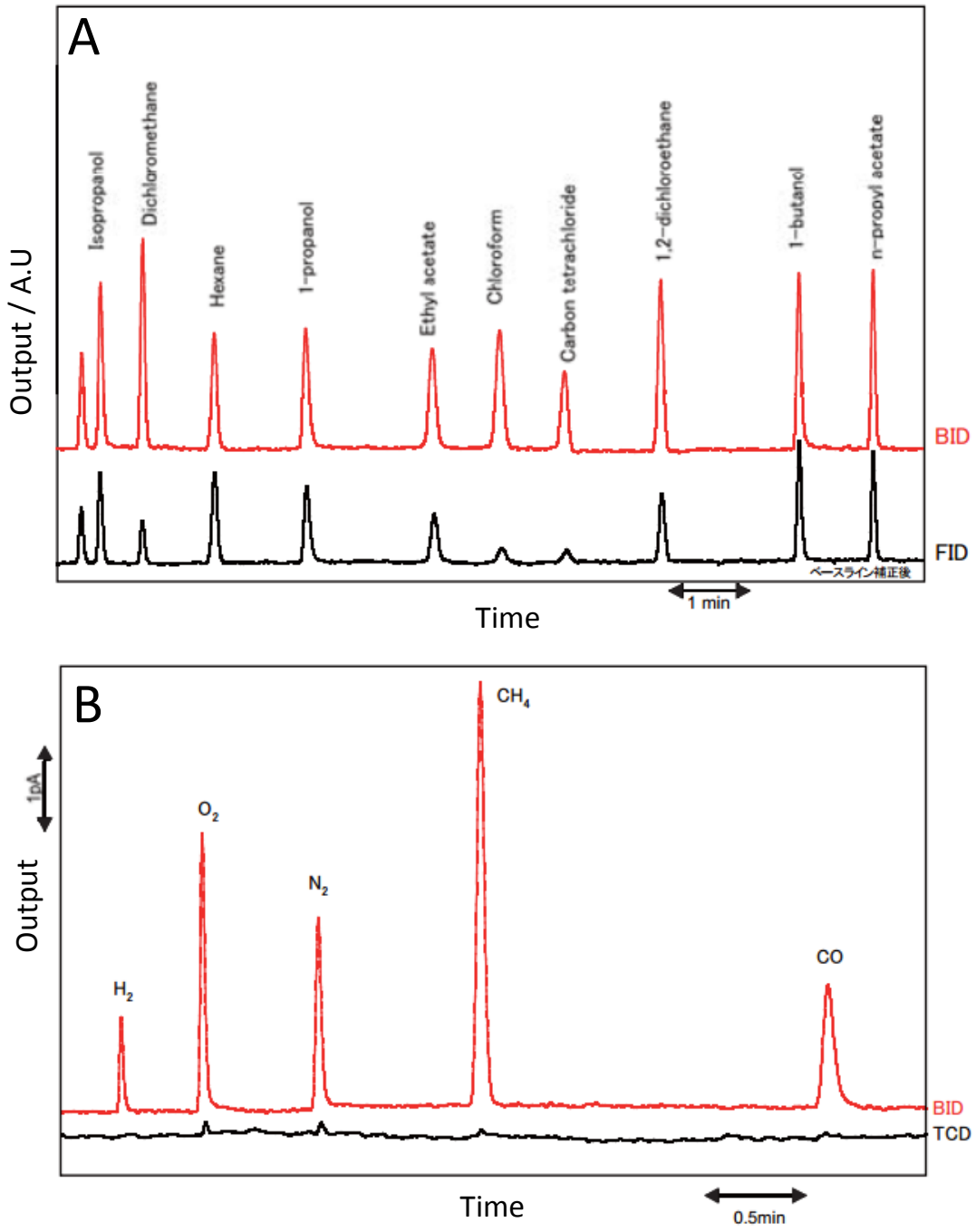

Fig. 20: (A) Chromatogram of a chlorine-containing sample and alcohol mixture (10 ppm each component). The relative response of BID and FID normalized by peak area of n-hexane. (B) Chromatogram of gas mixture of hydrogen, oxygen, nitrogen, methane, and carbon monoxide (10 ppm each component) using a BID (red curve) and a TCD (black curve) detector [155].

Gas chromatography equipped with a mass spectrometer detector

The liquid aliquots were injected into a Shimadzu GC-MS 2010SE chromatograph coupled with a MS QP2010 detector. The chromatographic column was Stabilwax-DA (30 m length

and 0.32 mm inner diameter) set at 40 °C, the gradually reached injection temperature was 220 °C. The MS detector was set at 200 °C, and helium was used as the carrier gas. Qualitative detection was afforded by selective ion monitoring (SIM)-MS, while the total ion chromatogram was used for the quantification of methanol and ethanol.

5. RESULTS AND DISCUSSION

5.1 Photoelectrochemical properties of conducting polymer electrodes

5.1.1 Electrosynthesis of the studied conducting polymers

All polymers were electrodeposited on a Au or GC working electrode from the respective monomer-containing solutions and the employed electrodeposition method was tailored to each monomer. Representative polymerization curves for EDOT, pyrrole, aniline and N-methylaniline are presented in **Fig. 21** (detailed description of the polymerization procedures is shown in section 4.2.1). The polymerization charge density (i.e., the thickness of the electrodeposited CP) was similar in all four cases, 150 mC cm^{-2}.

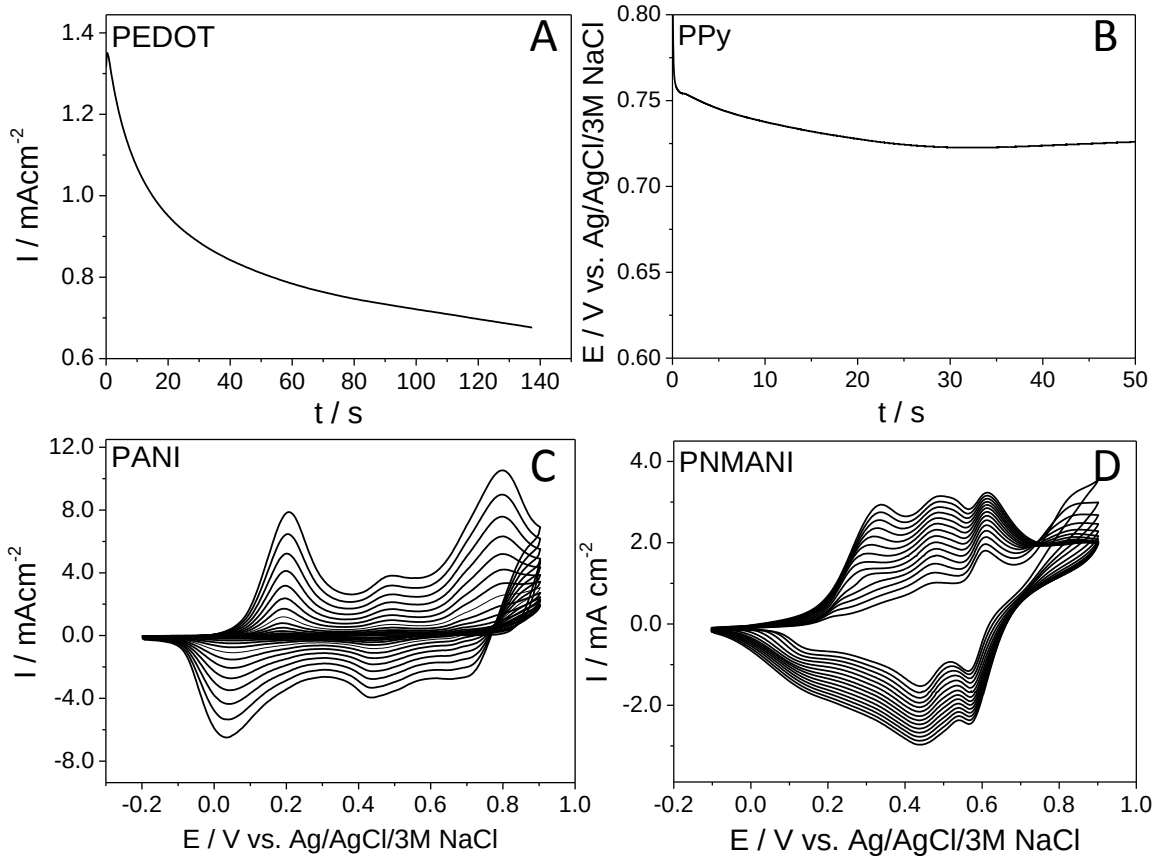

Fig. 21: Representative polymerization curves for the studied polymers. (A) 0.01 M EDOT; 0.05 M SDS; *E* = 1.1 V; (B) 0.1 M pyrrole, 0.05 M SDS; *i* = 3mA cm^{-2} (C): 0.2 M aniline, 0.5 M H_2SO_4; 100 mV s^{-1} (D): 0.1 M N-methylaniline; 1.0 M $HClO_4$; 100 mV s^{-1}. All polymers were deposited with a charge density of 150 mC cm^{-2}.

The intrinsic electroactivity of the CPs was evaluated by performing cyclic voltammetry experiments (in 0.1 M Na_2SO_4 saturated with N_2), applying a sweep rate of

100 mV s^{-1}. The potential regime was identified where conducting polymers behave as SCs (rather than as a semi-metal). This behavior is associated with the fully reduced state of the polymers, indicated with black arrows on **Fig. 22**. Both PANI and PNMANI get in their reduced state around 0.1 V, while several hundred millivolts more negative potential must be applied in the case of PEDOT and PPy to reach the same state. These determined potential values served as the basis of the photovoltammetry experiments.

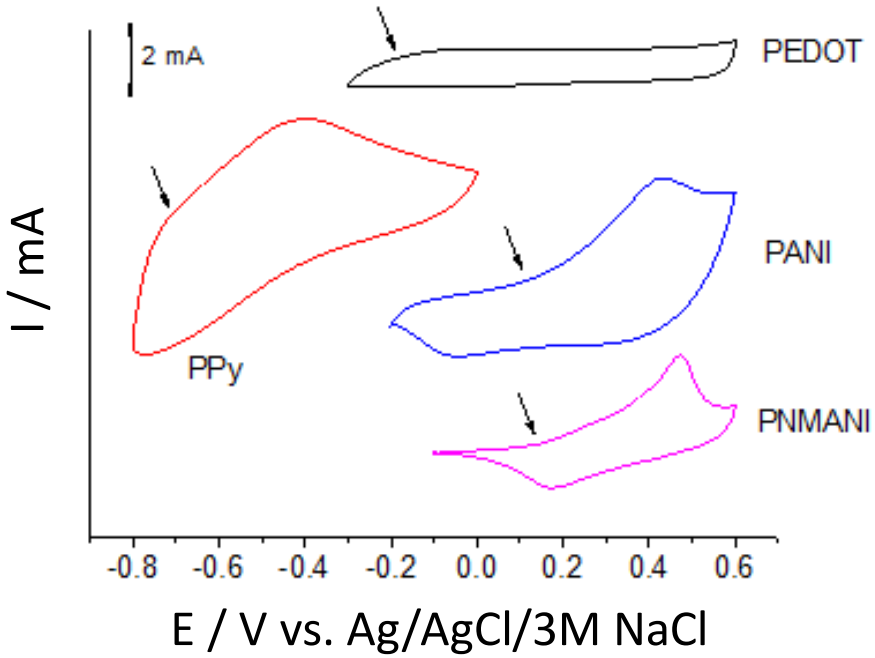

Fig. 22: CV traces registered in 0.1 M Na_2SO_4 in water at 100 mVs^{-1} scan rate, for PEDOT, PPy, PANI and PNMANI. The arrows indicate the onset potential value of electrochemical oxidation.

5.1.2 Photoelectrochemical behavior of poly(3,4-ethylelenedioxythiophene) electrodes

The PEC behavior of PEDOT photoelectrodes, electrodeposited with different polymerization charge densities, was studied by linear sweep photovoltammetry (**Fig. 23A**). The thickness of the polymer was in the 5 – 75 nm range [156].The maximum photocurrents were harvested at approximately −1 V vs. Ag/AgCl/3M NaCl. Photocurrents are cathodic in polarity, indicating that PEDOT behaves as a p-type SC, and the photocurrent can be attributed to PEC H^+-reduction.

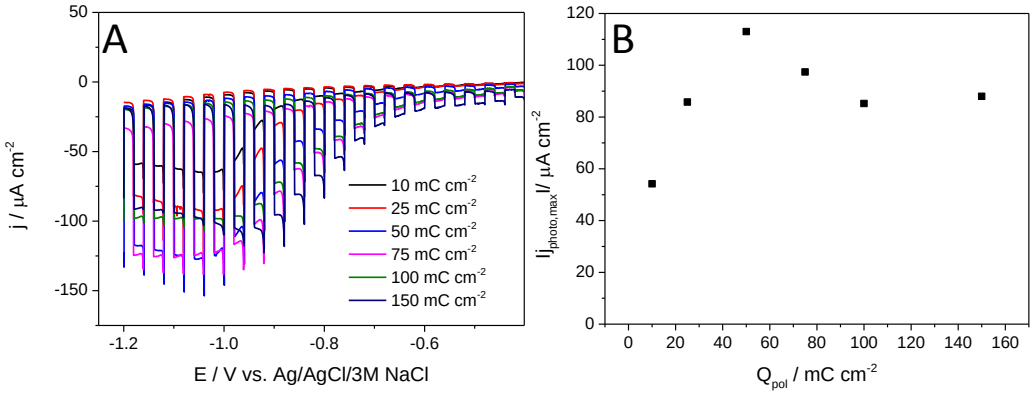

Fig. 23: (A) Photovoltammograms recorded in 0.1 M Na_2SO_4 saturated with Ar for PEDOT films, electrodeposited with different polymerization charge densities on GC electrode. The sweep rate was kept at 2 mV s^{-1}, while a solar simulator was applied as a light source and the light-chopping frequency was 0.1 Hz. (B) Maximum photocurrent vs. polymerization charge density plot, derived from the data presented in (A).

As a next step, the effect of CP layer thickness on the measured photocurrents was studied. In this vein, PEDOT layers were electrodeposited by varying the polymerization charge density. The photocurrent reached its highest value at 50 mC cm^{-2} PEDOT loading, and a notable decrease was seen at higher loadings. The reason behind these phenomena is the low charge carrier mobility of PEDOT [67]. PEC activity of PEDOT has been also tested towards the reduction of CO_2. As shown in **Fig. 24**, no enhancement was detected, the two photovoltammograms recorded in the presence/absence of CO_2 are similar in terms of both the shape and the magnitude of photocurrents.

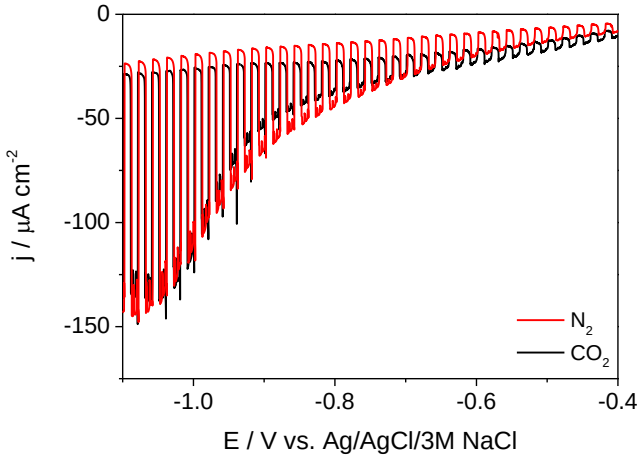

Fig. 24: Photovoltammograms recorded in 0.1 M Na_2SO_4 saturated with Ar and in 0.1 M $NaHCO_3$ saturated with CO_2 for PEDOT films, electrodeposited with 50 mC cm^{-2} polymerization charge densities on GC electrode. The pH was similar in both cases (pH ≈ 7.00) The sweep rate was kept at 2 mV s^{-1}, while a solar simulator was applied as a light source and the light-chopping frequency was 0.1 Hz.

Long-term measurements further corroborated these qualitative observations. A photocurrent transient evolved immediately upon illumination, which was followed by the rapid decrease of the photocurrent to a steady-state value, which was reached after around 50 − 60 min. (**Fig. 25A**). The formed gas-phase products were quantified by gas chromatographic analysis, applying a BID detector. Hydrogen was the only product which was identified (**Fig. 25B**), and its amount gradually increased during the photoelectrolysis (see the inset in **Fig. 25A**). The Faradaic efficiency was between 80 − 100%.

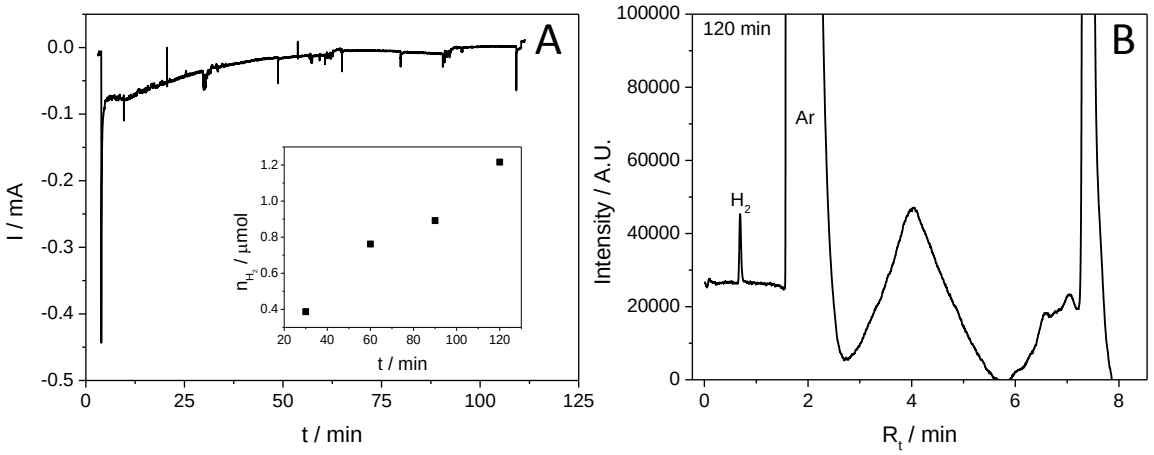

Fig. 25: (A) Long-term chronoamperometry data registered for PEDOT layers at E = −1.0 V potential (vs. Ag/AgCl/3M NaCl). A solar simulator was applied as a light source. (B) Gas-chromatogram, recorded during the long-term photoelectrolysis experiment, performed on a PEDOT photoelectrode in Ar-saturated 0.1 M Na_2SO_4.

5.1.3 Photoelectrochemical behavior of polyaniline electrodes

As a first step, the PEC behavior of PANI was investigated with linear sweep photovoltammetry. The photovoltammograms presented in **Fig. 26** bear all the hallmarks associated with the behavior of a *p-type* SC [146]. The photocurrents are cathodic in polarity, originating from the reduction of either H^+ ions or CO_2 at the conducting polymer/electrolyte interface. Photoexcitation of an electron from the valence band to the conduction band (via UV or visible light irradiation) is followed by electric-field separated photoelectrons being driven to the surface of the *p*-type SC where they can react with solution-confined species such as protons or CO_2. The reducing ability of the photogenerated electrons is dictated by the position of their surface quasi-Fermi level and the SC conduction band edge (**Fig. 7**). Therefore, it is possible to *photoreduce H^+ or CO_2 at a less negative* potential ("underpotential") relative to the thermodynamic reduction

potential; the principal role of external bias potential is to augment the built-in electric field to separate the photogenerated charge carriers. This observation highlights the benefit of the PEC method over its "dark" electrochemical counterpart where usually high overpotential (thus high energy input) is needed to drive the reaction due to the kinetic constraints of CO_2 reduction or H_2-evolution.

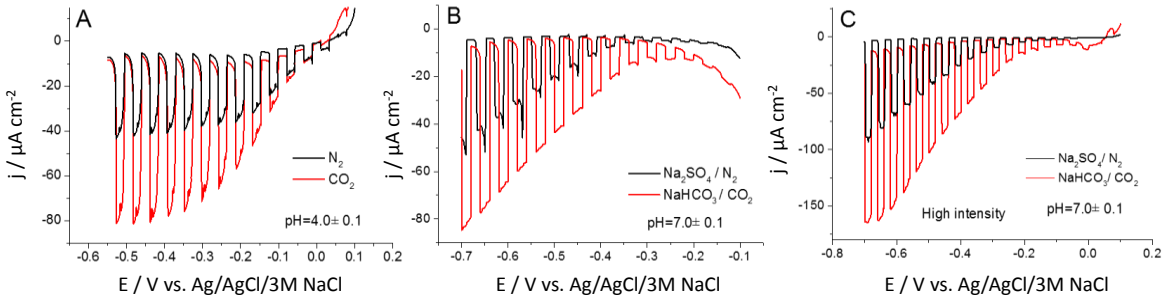

Fig. 26: Representative photocurrent-potential profiles for an electrodeposited PANI layer under chopped UV-vis illumination (Xe-Hg Arc lamp, 100 W output) in (A) N_2- and CO_2-saturated 0.1 M Na_2SO_4 aqueous solution where the N_2-saturated solution was buffered to *pH* = 4.0; (B) N_2- saturated 0.1 M Na_2SO_4 and CO_2-saturated $NaHCO_3$ aqueous solutions (*pH* = 7.0); (C) Same measurement as in (B), but with increased light intensity (Xe-Hg Arc lamp, at 300 W output).

Comparing the two curves in **Fig. 26A**, a two-fold increase was seen in the cathodic photocurrents in the plateau region in the presence of CO_2. What is also important, the onset potential (+0.1 V vs. Ag/AgCl/3M NaCl) observed at the maximum light intensity (**Fig. 26C**) was several hundred mV *less negative* than the thermodynamic potential of most of the CO_2 reduction processes, and in particular the CO_2/CH_3OH redox process (see **Fig. 7**) which lies at -0.41 V vs Ag/AgCl/3M NaCl at pH = 4.

The pH strongly affects both the (photo)electroactivity of PANI [157] as well as the H^+ reduction (H_2-evolution) process. To separate the intrinsic contribution of CO_2 from the more trivial pH-effect (caused by the increased H^+ concentration because of the CO_2 dissolution), the control measurement under N_2 atmosphere was recorded in a buffered solution having exactly the same pH as measured in CO_2 saturated solution (*pH* = 4.0 ± 0.1, **Fig. 26A**). Similar comparison was performed in $NaHCO_3/CO_2$ solution (*pH* = 7.0 ± 0.1, **Fig. 26B**), and very similar conclusions were drawn, together with the observation of a 150 mV shift in the onset potential, which indicated the participation of H^+ ions in the CO_2 reduction. Finally, the photon flux was increased to the maximum output of the lamp (300 W), which resulted in an almost three-fold increase of the photocurrents (with a maximum

of 170 µA cm^{-2}, see **Fig. 26C**). This proportional increase in the photoconversion rate with the photon flux suggests that carrier-recombination processes are not yet rate-limiting in the overall process.

As a next step, the effect of CP layer thickness on the measured photocurrents was studied in CO_2-saturated 0.1 M $NaHCO_3$ solution (**Fig. 27A**). Similarly to PEDOT, the photocurrent reached its maximum value at 50 mC cm^{-2} PANI loading (**Fig. 27B**), without further enhancement by increasing the layer thickness (moreover, a slight decrease was observed at very high loadings). This behavior is rooted in the low charge carrier mobility, which is characteristic to CPs (see also chapter 2.4). Consequently, it is not possible to increase the polymer thickness to a level where light absorption is sufficient, because the photogenerated charge carriers recombine before they could be fully extracted.

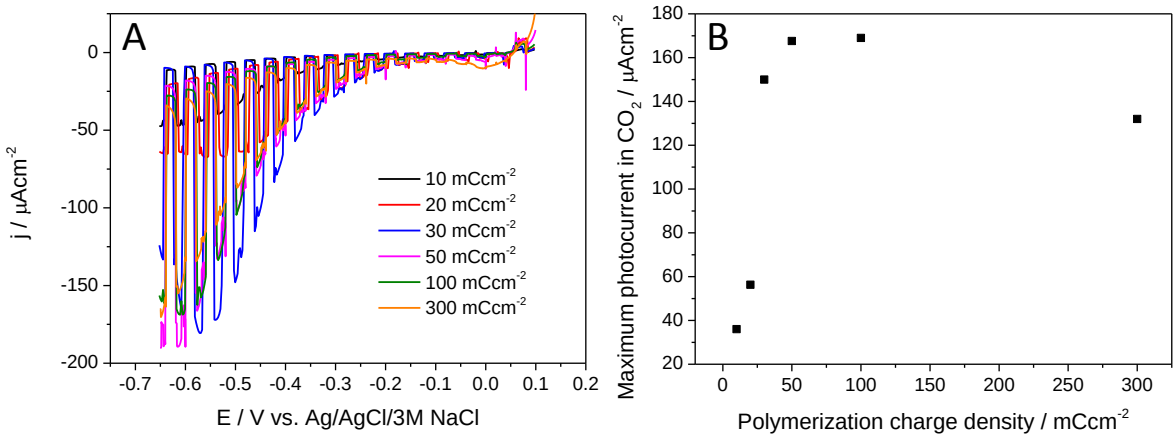

Fig. 27: (A) Photovoltammograms recorded in 0.1 M CO_2-saturated $NaHCO_3$ (*pH* ≈ 7.0) for PANI films, electrodeposited on Au by varying the polymerization charge densities. The sweep rate was kept at 2 mV s^{-1}, while the light-chopping frequency was 0.1 Hz. A 300W Hg-Xe lamp was used as a light source. (B) Maximum photocurrent vs. polymerization charge density plot, derived from the data presented in (A).

To further examine the photoreduction process, photoaction spectra were measured to determine IPCE. As seen in **Fig. 28A,** the obtained photoaction spectra perfectly overlapped with the UV-vis spectrum of PANI (**Fig. 28B**), recorded under identical circumstances (i.e., E = −0.4 V external bias potential). This means, that PANI absorbs photons in the same wavelength range in which it is photoactive.

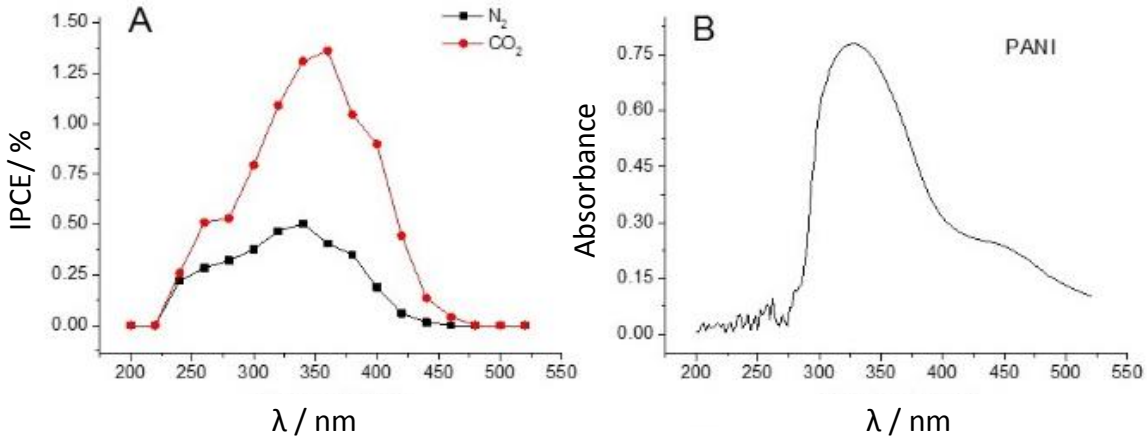

Fig. 28: (A) Photoaction spectra of PANI registered at E = −0.4 V in N_2- and CO_2-saturated 0.1 M Na_2SO_4 aqueous solution. (B) UV-vis spectrum of PANI registered at E = −0.4 V in CO_2-saturated 0.1 M Na_2SO_4 aqueous solution.

The threshold energy determined from the photoaction spectra (440 nm, 2.8 eV) nicely agreed with the bandgap energy (2.8 eV) obtained from the UV-vis spectra (Tauc-plot). Photovoltammograms were also recorded by irradiating the photocathode with simulated sunlight yielding very similar profiles (**Fig. 29**) both in terms of shape and the enhancement, as in the UV-vis-illuminated case (**Fig. 26B**).

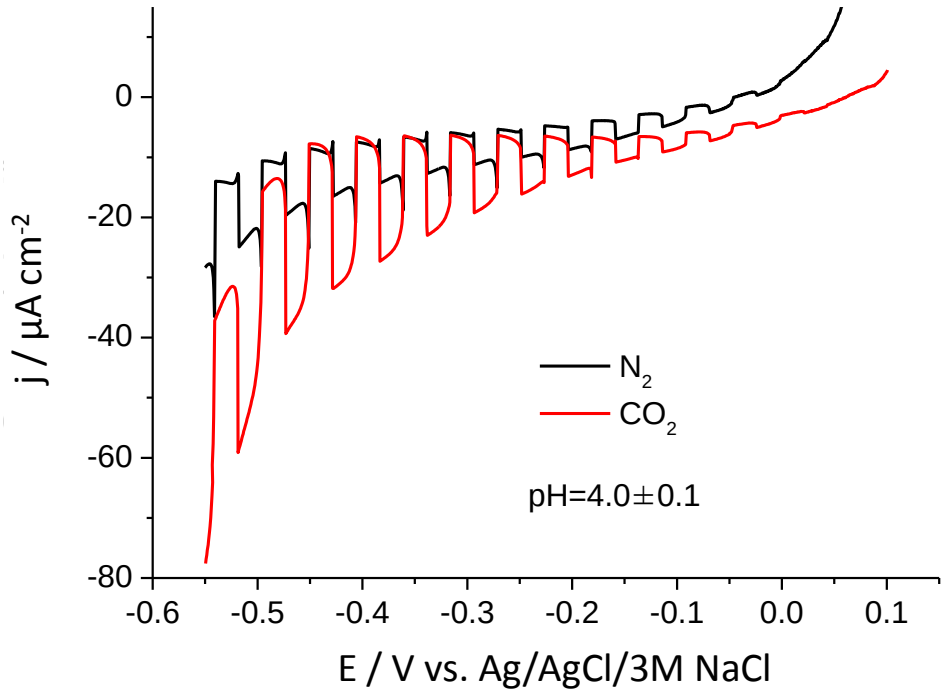

Fig. 29: Representative photocurrent-potential profiles for an electrodeposited PANI layer under simulated sunlight illumination (100 mW cm^{-2}) in N_2- and CO_2-saturated 0.1 M Na_2SO_4 aqueous solution (pH = 4.0±0.1).

5.1.4 Long-term photoelectrolysis measurements

Long term constant-potential electrolysis was performed at E = −0.4 V (**Fig. 30A**), and the formed products were analyzed using GC and GC-MS (**Fig. 30B**) for the gas and liquid phase, respectively. The striking difference in the stationary currents (20 μA vs. 70 μA) recorded after 2 h in the two cases suggests that the PANI layer, at least partially, maintained its PEC efficacy for the studied time period. While in the gas phase only H_2 was detected as the product in both cases (through proton reduction), methanol and ethanol (together with some minor traces of formaldehyde) were detected in the solution for CO_2-saturated samples. Importantly, no such products could be detected under N_2-saturation. In the CO_2-saturated case, it was found that 20% of the transferred charge (Faradaic efficiency) accounts for H_2 formation, while the rest is responsible for the alcohol formation with an approximately 2:1 methanol/ethanol molar ratio (≈ 43% and ≈ 20%).

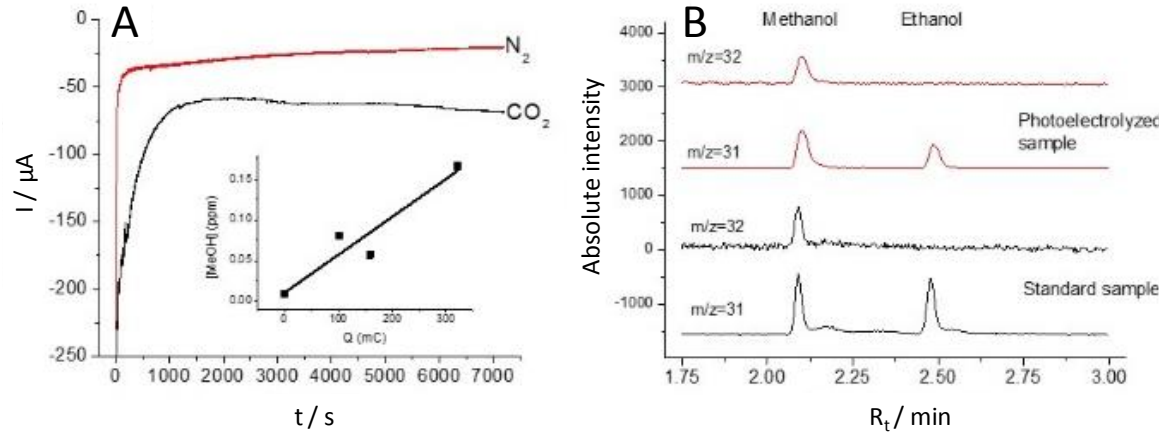

Fig. 30: (A) Current/time profiles under continuous UV-vis light irradiation at E = −0.4 V vs. Ag/AgCl/3M NaCl in a sealed two-compartment PEC cell containing a PANI layer photocathode. Electrolyte was 0.1 M $NaHCO_3$ saturated with CO_2 (pH ≈ 7.0) or N_2-saturated 0.1 M Na_2SO_4. The inset shows the increasing methanol concentration with the transferred charge, as deduced from data shown in (B). (B) GC-MS profiles registered using selective ion monitoring (SIM) for the sample after photoelectrolysis shown in (A) as well as for a standard solution containing 0.5 ppm methanol and ethanol respectively.

During the long term photoelectrolysis, an initial decrease in the photocurrents was always observed (see also in **Fig. 30A**). At the same time, the intrinsic *electro*activity of the PANI films did not change significantly (as probed by cyclic voltammetry before and after photoelectrolysis, see **Fig. 31**). This fact confirms that no a molecular or supramolecular degradation is the process behind the decrease of the PEC performance.

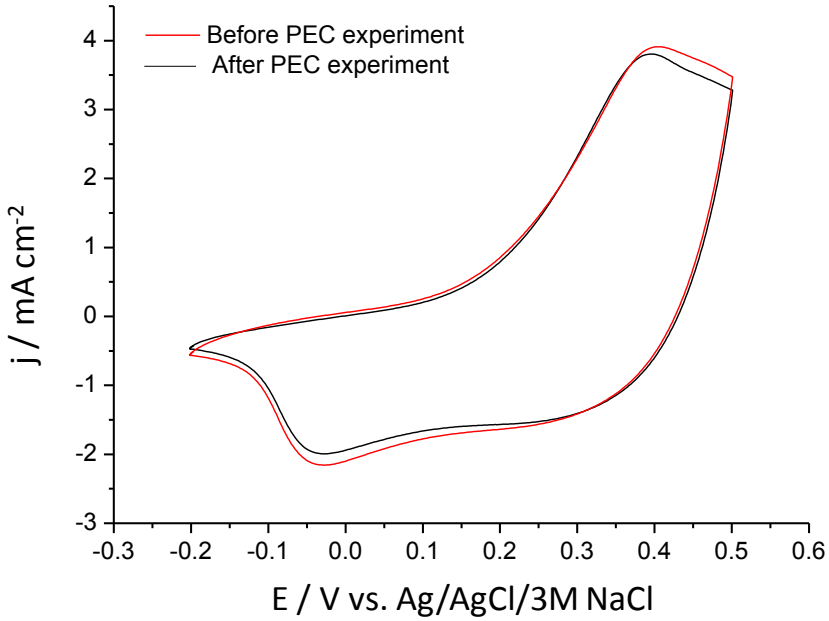

Fig. 31: CV traces registered in 0.1 M Na_2SO_4 in water at 100 mVs^{-1} scan rate, for a PANI film, before and after performing photoelectrolysis (as presented in **Fig. 30A**).

SEM images furnished insights on this peculiar phenomenon, namely that the decrease in the PEC activity is predominantly rooted in the melting of the polymer (**Fig. 32**). Melting of the PANI film causes a decrease in the surface area, thus the majority of the photoactive material becomes inaccessible for the CO_2 saturated solution. Such light-induced melting was reported earlier for PANI [158], and in our case the local heating, induced by charge carrier recombination, can be responsible for this phenomenon.

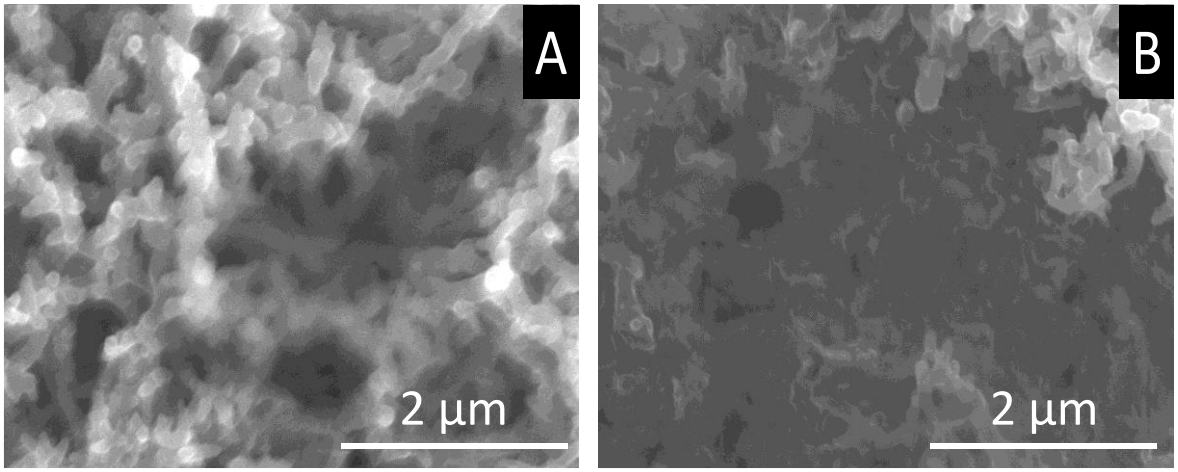

Fig. 32: SEM images of electropolymerized PANI films (with a charge density of 150 mC cm^{-2}), before (A) and after (B) a 2 h CO_2 photoelectrolysis at E = −0.4 V. Continuous UV-vis illumination (Xe-Hg Arc lamp, 300 W output) was employed.

5.1.5 Factors behind the photoelectrochemical activity toward the reduction of CO_2

To probe the factors behind the PEC activity, similar data as in **Fig. 26** are shown in **Fig. 33** for PPy, poly(N-methylaniline) (PNMANI) and PEDOT. Photovoltammograms, recorded for PEDOT and PPy show negligible photoeffects from CO_2 reduction. The conduction band edge positions of these CPs are located negative enough to reduce CO_2 (**Fig. 7**). Therefore, the lack of photoactivity clearly does not reside with smaller driving force for photoinduced electron transfer relative to PANI. In other words, factor(s) beyond thermodynamics must control the rather unique ability of PANI to photoelectroreduce CO_2. With the notion that the chemical environment of the *N*-atom in PANI must be of special importance, similar experiments were carried out with PNMANI. The only difference here from PANI is the lack of *H*-substituent on the *N*-atom in the conjugated structure, the hydrogen being substituted by a methyl group. Importantly, the enhanced PEC behavior seems to be unique to PANI, because no such increase can be seen for its $–CH_3$ derivative (**Fig. 33B**); clearly this small structural difference exerts a huge impact on CO_2 photoreduction efficacy.

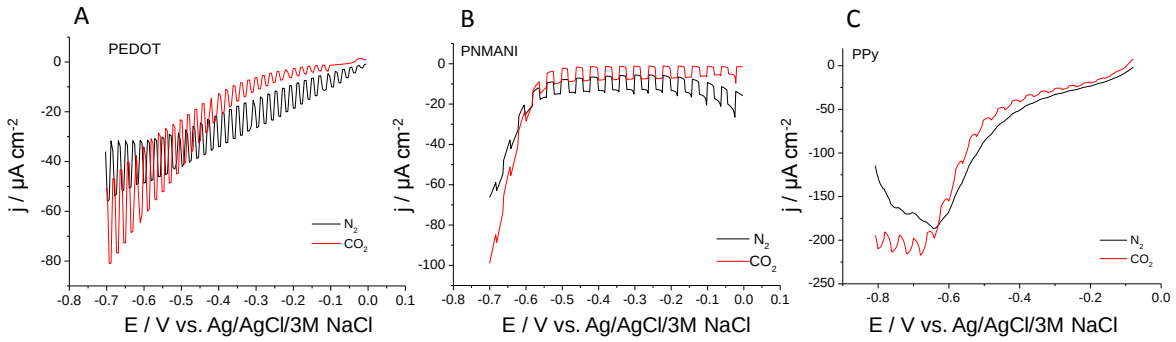

Fig. 33: Representative photocurrent-potential profiles of an electrodeposited PEDOT (A), PNMANI (B), and PPy (C) layers under chopped UV-vis illumination (Hg-Xe Arc lamp, 100 W output) in a N_2- and CO_2-saturated 0.1 M Na_2SO_4 aqueous solution.

The interaction of CO_2 with PANI is a very important factor, which might significantly affect the PEC properties of the CP, therefore it had to be studied thoroughly. As a first step, the adsorption of CO_2 on the studied CPs was investigated with quartz crystal microgravimetry (QCM) measurements. **Fig. 34A** compares three adsorption/desorption sequences for the above-discussed polymers on gold supporting electrodes, as derived from QCM measurements. The largest adsorbed amounts were detected for PANI, and also somewhat surprisingly, for PPy. In addition, careful comparison of the desorption portion of these data revealed striking differences: while for PNMANI, the mass decreased rapidly

upon N_2 purging (10 – 15 s), in the case of PANI it took 300 s to reach the original mass value. Note that all these polymer films were electrodeposited with identical charge density; therefore, their thickness was also very similar. Consequently, we have to assume that there is specific chemical interaction between PANI (and PPy) and the CO_2 molecules beyond simple physisorption, which clearly does not exist for PEDOT and PNMANI.

To shed further light on the underlying surface chemistry, a series of diffuse reflectance FT-IR spectra were recorded for both PANI and PMANI, both before and after being in contact with CO_2 (**Fig. 34B**). The difference is striking: while a set of new vibrations was visible for PANI, there was no change for PNMANI (**Fig. 34B**). The changes observed for PANI are the superposition of the alteration of the original PANI spectrum (because of protonation, see **Scheme 2**) [159] and the bands related to the chemisorbed CO_2. The appearance of the ν(C=O) at 1680 cm^{-1} (in carbamic acid) as well as the $\nu_{as}(COO^-)$ and $\nu_s(COO^-)$ vibrations at around 1530 cm^{-1} and 1450 cm^{-1} respectively[160,161] confirmed the formation of carbamic acid and carbamate (see **Scheme 2**) as reported for primary and secondary amine-containing (non-conductive) polymers [161]. Importantly, the vibrations related to physisorbed CO_2 were of very similar intensity in the two cases (not shown here).

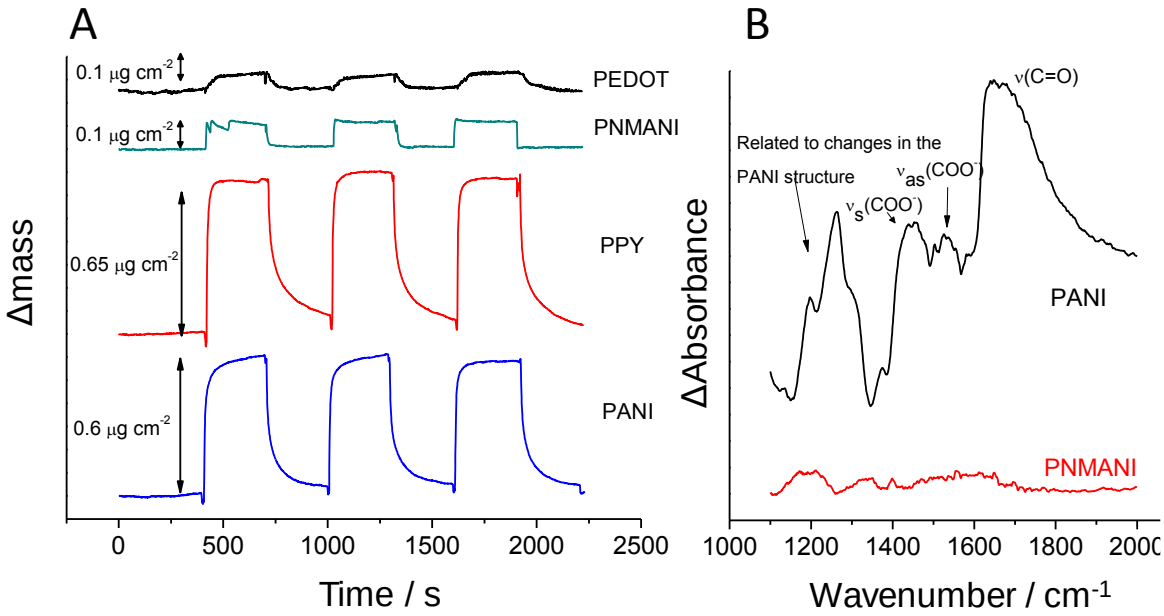

Fig. 34: (A) Subsequent mass changes upon CO_2 and N_2 exposure for the various conducting polymer films, as registered by QCM. (B) Changes in the FT-IR spectra of PANI and PNMANI upon exposure to CO_2 for 5 min; the background was the respective polymer pre-treated in He in both cases (refer to Section 4.2.2).

Taking all the findings from this study together as a whole, the following reaction scheme is suggested for the PEC reduction of CO_2 by PANI. The formation of protonated PANI explains the observed color change upon CO_2 adsorption and is a necessary but not sufficient criterion. Adsorption of CO_2, while important, is also not enough as seen by the example of PPy. The polymer band edge positions (see **Fig. 7**) are critical in at least two aspects: i) the CB edge (LUMO band position) of the CP has to be negative enough for the photogenerated electrons to reduce CO_2; ii) The VB edge (HOMO band position) has to be positive enough, to make the conducting polymer behave as a SC (rather than as a semi-metal) at the potential where the PEC experiment is performed. In the latter case, the polymer electroactivity would dominate, as exemplified here by the PPy case (**Fig. 22**).

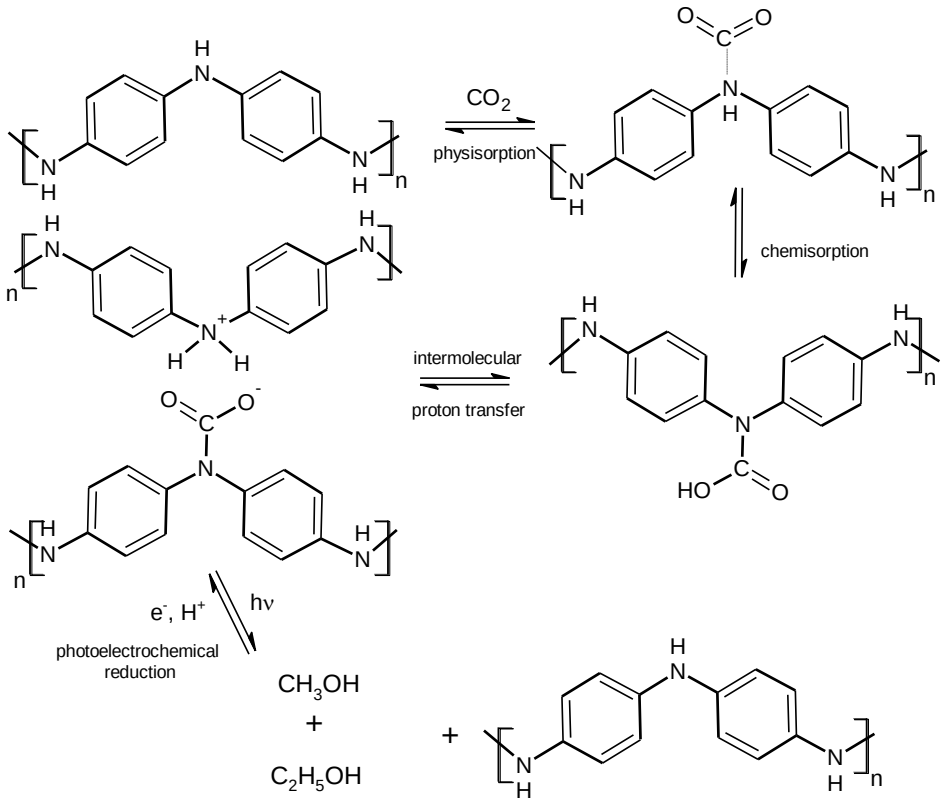

Scheme 2: Possible mechanistic pathway for CO_2 adsorption and photoelectroreduction on PANI.

It has been showed in this chapter, that CPs are attractive photoelectrode candidates, which can be used to drive PEC H^+-, and CO_2 reduction processes. However, two major drawbacks were identified: low conductivity, which resulted in enhanced recombination, thus small photocurrents and poor photostability. A possible way to overcome the experienced low conductivity of CPs is to deposit them on a high-surface

area, highly conductive nanostructured scaffold. Therefore, after these preliminary studies, our focus turned to CP/nanocarbon systems, which results are presented in the following chapter.

5.2 Photoelectrochemical behavior of conducting polymer/nanocarbon electrodes

5.2.1 Electrodeposition of poly(3,4-ethylenedioxythiophene) on the nanocarbons

After immobilizing the CNT or graphene scaffolds on the GC working electrode surface, PEDOT was electrodeposited potentiostatically. Systematic variation of the polymerization charge density during the synthesis resulted in nanocomposite layers with different PEDOT/nanocarbon ratio. In the case of the nanocarbons higher currents flowed during the potentiostatic polymerization, compared to the bare GC, because of their higher surface area (see an example in **Fig. 35**).

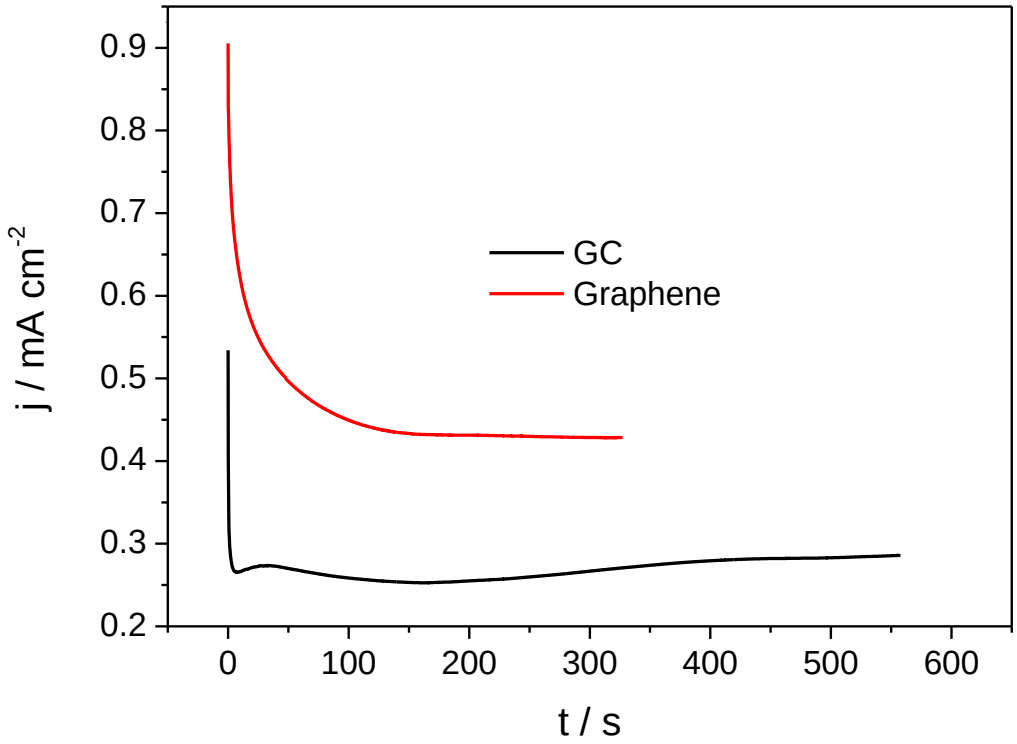

Fig. 35: Chronoamperometric polymerization curves, recorded during the electrodeposition of PEDOT on the surface of a bare GC (black curve), and a graphene-coated GC (red curve) electrode ($m_{graphene}$ = 110 µg cm^{-2}, Q_{pol} = 150 mC cm^{-2}).

CVs were recorded for each nanocomposite sample in an Ar saturated 0.1 M Na_2SO_4 solution to determine their charge capacitance. The CVs and the charge capacitance vs. polymerization charge density curves, collected for the PEDOT/graphene nanocomposite electrodes, are shown in **Fig. 36**. The linear relationship between the polymerization charge density and the electroactivity of the obtained PEDOT, confirmed the continuous growth

of the polymer on the nanocarbon support. Similar observations were made in the case of the PEDOT/CNT layers.

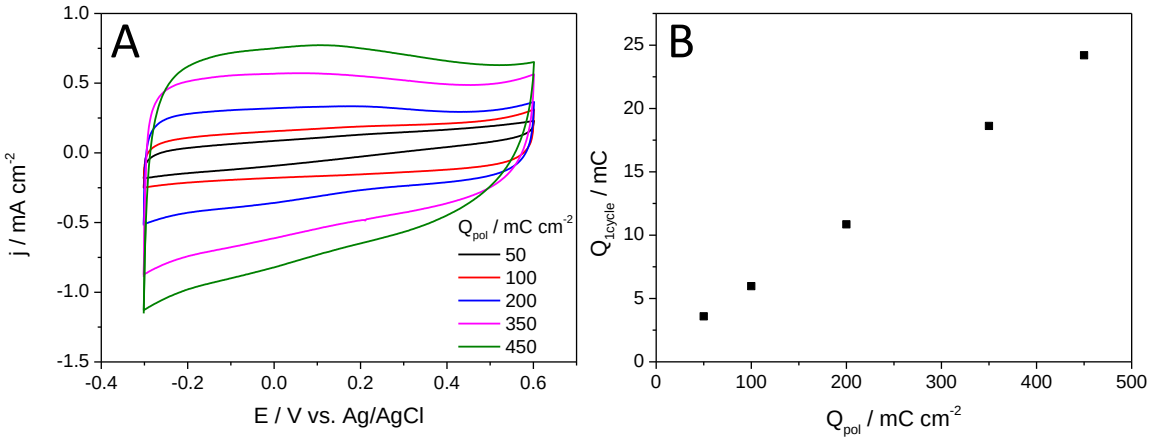

Fig. 36: (A) Comparison of CVs recorded for PEDOT/graphene nanocomposite electrodes ($m_{graphene}$ = 110 µg cm^{-2}) synthesized with different PEDOT loading in 0.1 M Na_2SO_4 solution, saturated with Ar (υ = 50 mV s^{-1}) (B) Total integrated charge passed during the cycle vs. polymerization charge density plot for various PEDOT/graphene electrodes.

5.2.2 Morphological and physical characterization

Morphological features of the pristine components and the nanocomposites were investigated with SEM and TEM. The bare PEDOT formed a continuous sponge-like coating on the GC electrode surface (**Fig. 37**), which is characteristic to the electrodeposited PEDOT when SDS is applied as supporting electrolyte.[162]

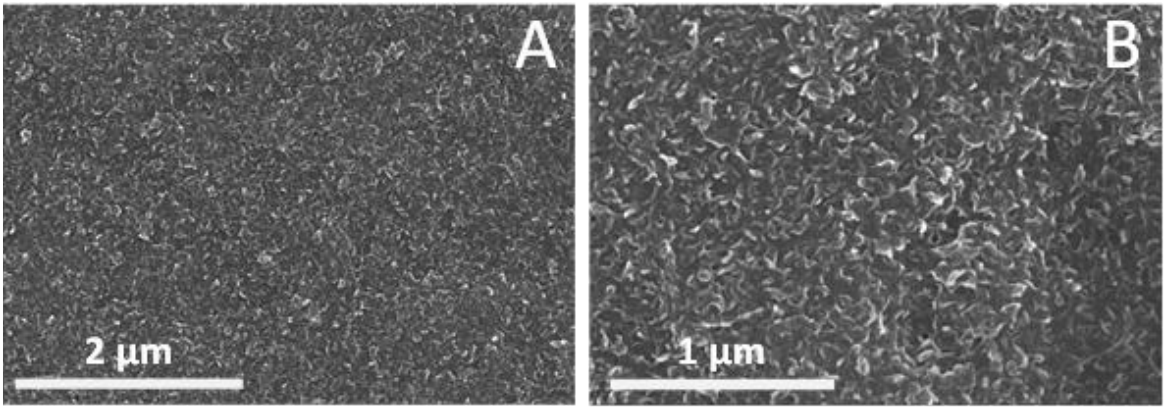

Fig. 37: SEM images of a bare PEDOT layer electrodeposited on a GC electrode (Q_{pol} = 50 mC cm^{-2}).

Fig. 38 shows SEM images of the bare nanocarbons (A, D) and the respective nanocomposite samples (B, C, E, and F). SEM images confirmed that both the bare CNT and

the graphene covered the GC surface completely. The average diameter of the nanotubes was 15 ± 4 nm (see also **Fig. 39** for the size distribution histogram, derived from the SEM measurements), while the average graphene flake size was 1088 ± 49 nm.

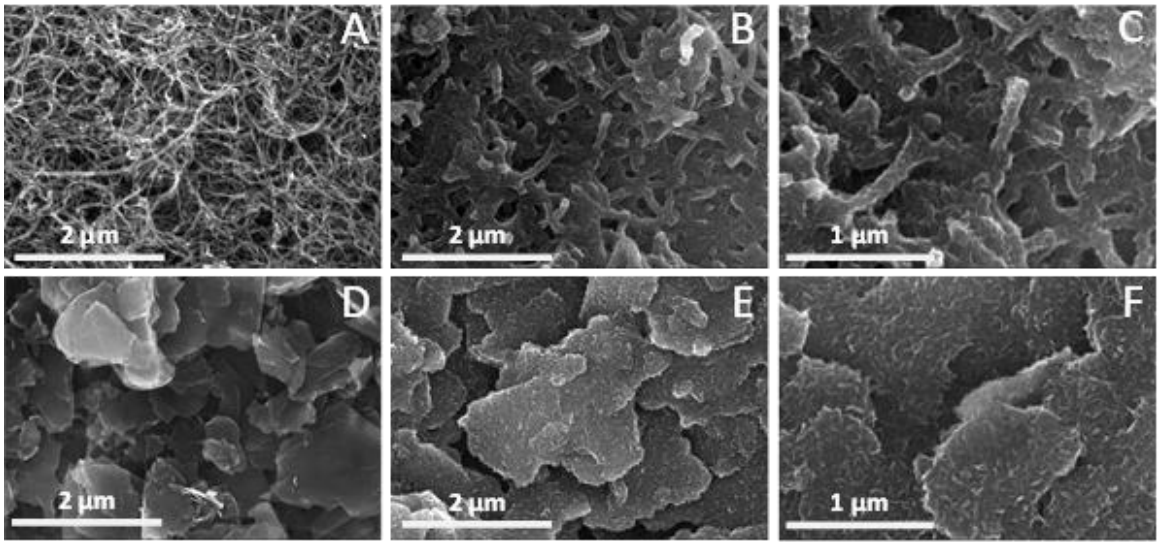

Fig. 38: (A) SEM images of a bare CNT layer on GC (m_{CNT} = 60 µg cm^{-2}), (B, C) PEDOT/CNT nanocomposite layer on GC (m_{CNT} = 60 µg cm^{-2}), Q_{pol}= 400 mC cm^{-2}, (D) graphene layer on GC ($m_{graphene}$ = 110 µg cm^{-2}) (D), and (E, F) PEDOT/graphene layer on GC ($m_{graphene}$ = 110 µg cm^{-2}), Q_{pol}= 200 mC cm^{-2}.

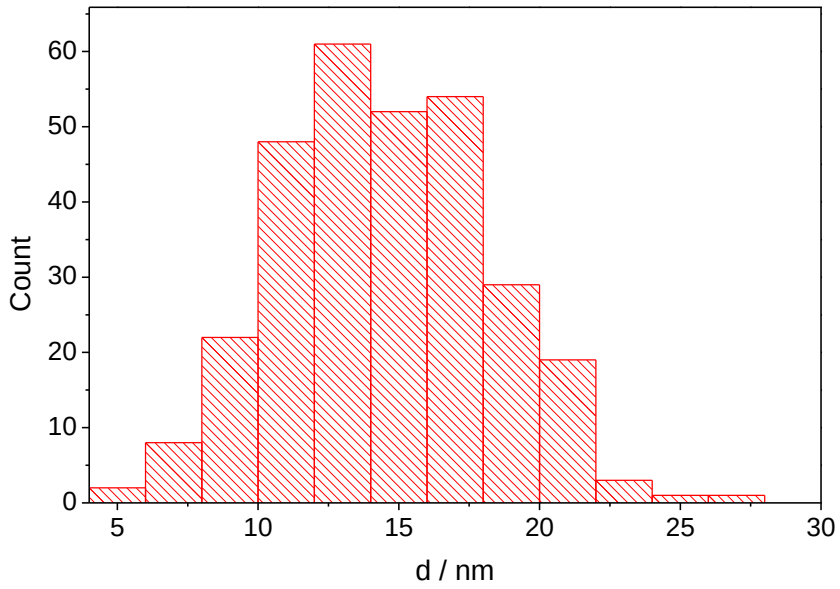

Fig. 39: Diameter of the bare CNTs, calculated from the SEM images that are presented in **Fig. 38A**.

SEM images of a PEDOT/CNT nanocomposite demonstrated that the carbon nanonetwork was entirely covered by the polymer (**Fig. 38B, C**). The thickness of the deposited PEDOT layer can be calculated with the following equation:

$$d_{PEDOT} = \frac{d_{CNT+PEDOT} - d_{CNT}}{2} \quad (4)$$

The histogram, presented in **Fig. 40**, shows that the PEDOT thickness was in the 20–80 nm range, with an average of 40 ± 11 nm. This observation stands only for the layers, where the polymerization charge density was maintained at 400 mC cm^{-2}, while the amount of the spray-coated CNT was fixed at 60 μg cm^{-2}. The layer thickness, however, can be tuned up to an extent, where PEDOT forms a constant layer filling up the gaps between the individual CNTs. Similar observations were made for the PEDOT/graphene nanocomposites, where PEDOT coated the surface of the nanoflakes evenly (**Fig. 38E**, **F**).

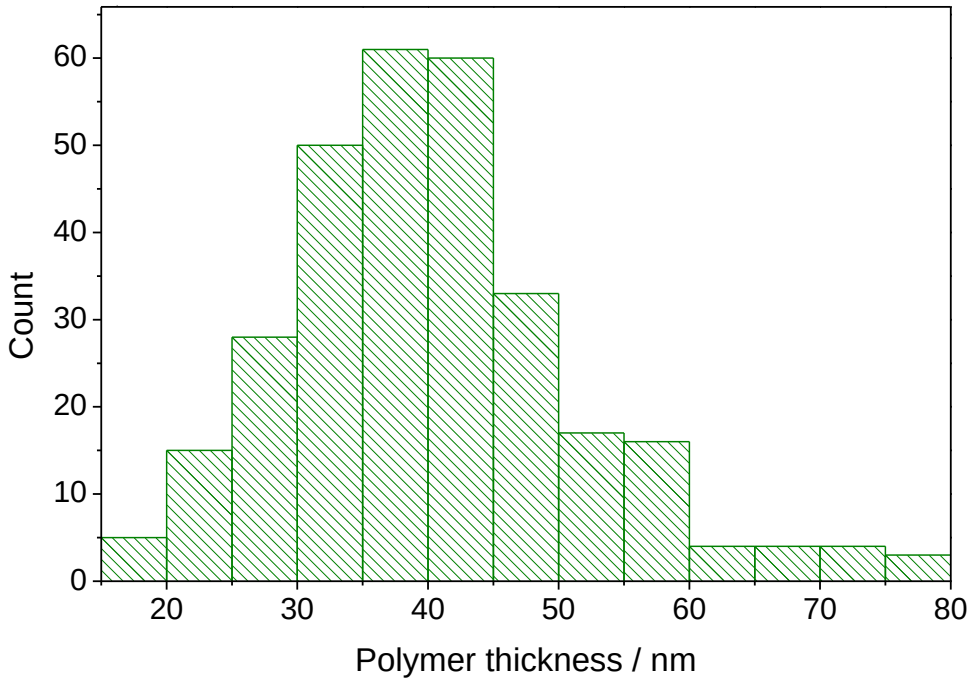

Fig. 40: PEDOT layer thickness on the CNTs, as calculated from **Fig. 38A**, **B** and **C**.

TEM images of the bare CNTs and a PEDOT/CNT nanocomposite (m_{CNT}= 60 μg cm^{-2}, Q_{pol} = 400 mC cm^{-2}) revealed that the polymer completely enfolded the nanotubes (**Fig. 41A-C**). This was further visualized by HR-TEM images (**Fig. 42**), where a 10 – 15 nm thick PEDOT film was spotted around the carbon nanotube. Pristine graphene appeared on the TEM images as large, two-dimensional sheets (**Fig. 41D**). As for the nanocomposite, less sharp and less well-defined edges formed, indicating the presence of PEDOT on the surface of the nanoflakes (**Fig. 41E and F**).

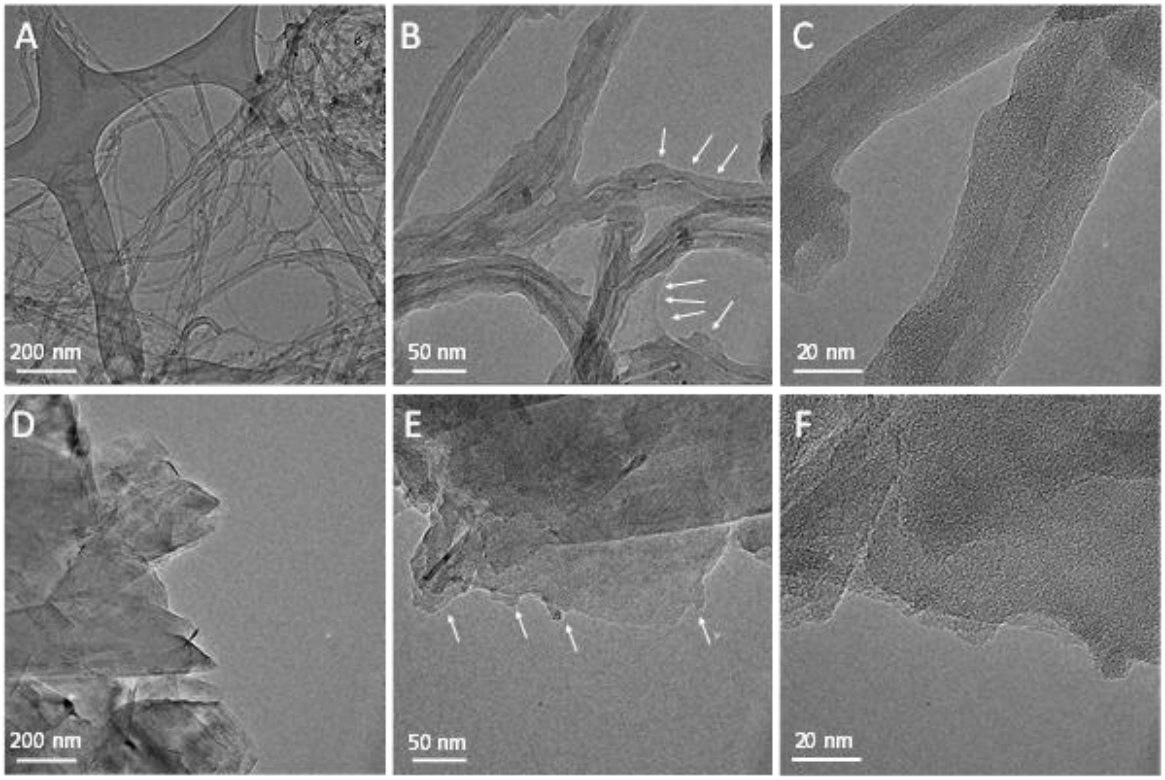

Fig. 41: TEM images captured for the (A) bare CNTs, (B, C) PEDOT/CNT layer (m_{CNT} = 60 μg cm^{-2}, Q_{pol} = 400 mC cm^{-2}), (D) bare graphene, (E, F) PEDOT/graphene ($m_{graphene}$ = 110 μg cm^{-2}, Q_{pol} = 200 mC cm^{-2}) nanocomposites. The white arrows highlight the presence of the polymer on the surface of the nanocarbons.

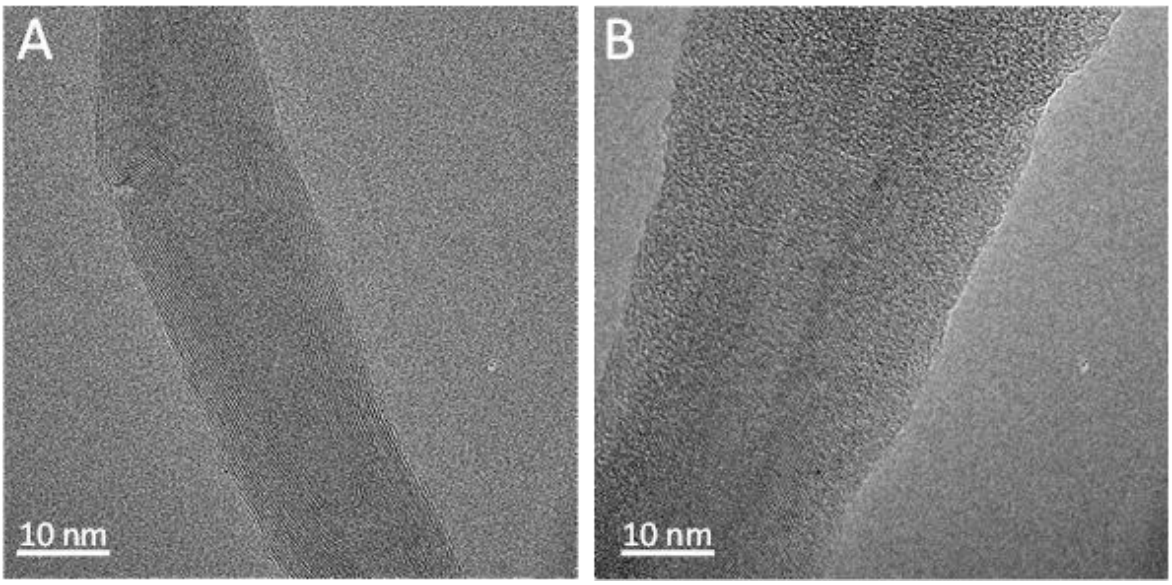

Fig. 42: HR-TEM images captured from a (A) bare CNT, and (B) PEDOT/CNT nanocomposite layer.

To gain further insights into the structural properties of the nanocomposite samples, Raman spectroscopy was employed (**Fig. 43**). The spectrum of the CNT film

showed two typical broad bands (black), characteristic to all carbon nanomaterials. One of them is centered at 1588 cm^{-1} (G band) and the other one is at 1347 cm^{-1} (D band) [163]. The spectrum of the bare PEDOT layer is presented in **Fig. 43A** (blue curve). The assignation of the observed bands is presented in **Table 2**, which confirmed the presence of conjugated PEDOT [164–167]. All these characteristic bands are visible on the spectrum of the PEDOT/CNT nanocomposite without any significant and characteristic shift compared to that of the bare constituents.

The graphene-containing electrodes showed similar trends to the PEDOT/CNT samples (**Fig. 43B**). There are three characteristic bands on the spectrum: a sharp G band centered at 1570 cm^{-1} (attributed to the vibration of the sp^2 hybridized carbon atoms), the D band, centered at 1340 cm^{-1} (corresponding to the sp^3 defects in the graphene layers) and the 2D band, centered at 2689 cm^{-1} (attributed to the double resonant scattering process from zone-edge phonons) [168,169]. The small D/G ratio (0.17) and the shape and position of the 2D band suggests that a high-quality, few-layer graphene was applied in this study [170,171]. Conclusions that were drawn from the spectrum of the PEDOT/graphene sample are similar to PEDOT/CNT nanocomposites.

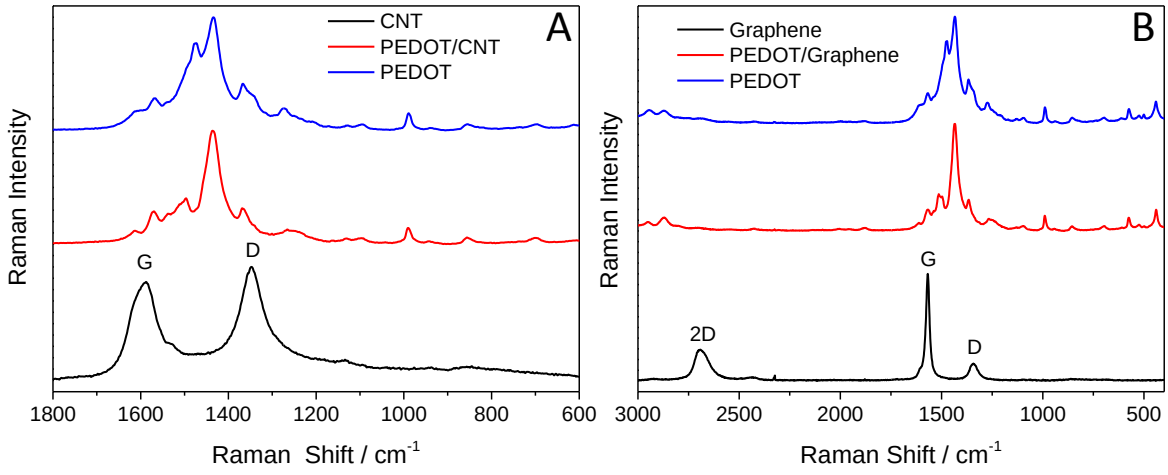

Fig. 43: Raman spectra of (A) CNT (black line), PEDOT (blue line) and PEDOT/CNT (red line) samples (m_{CNT} = 60 µg cm^{-2}, Q_{pol}= 400 mC cm^{-2}), and (B) graphene (black line), PEDOT (blue line) and PEDOT/graphene (red line) samples ($m_{graphene}$ = 110 µg cm^{-2}, Q_{pol} = 200 mC cm^{-2}).

Table 2: Assignation of the characteristic Raman bands of PEDOT.

Raman Shift / cm^{-1}	**Assignment**[164–167]
578 991	Oxyethylene ring deformation
699	Symmetric C–S–C deformation
1090 1124	C–O–C deformation
1270	C_α–$C_{\alpha'}$ (inter-ring) stretching
1368	C_β–C_β stretching
1434	symmetric C_α=C_β(–O) stretching

5.2.3 Photoelectrochemical behavior

Given that the PEC attributes are highly dependent on the morphology and composition of the nanohybrid photoelectrodes, two directions were followed to optimize their performance. First, to find the optimal PEDOT/nanocarbon ratio, the amount of CNT and graphene on the electrode surface was kept constant, while the amount of PEDOT was varied systematically by changing the polymerization charge. After determining the optimal PEDOT/nanocarbon ratios (one for CNT and another for graphene), the effect of carbon loading was investigated. In these experiments, the PEDOT/CNT and PEDOT/graphene ratio was held constant and the amount of the nanocarbon (and thus the nanocomposite) was varied. The polymer content had a major effect on the maximum photocurrent (**Fig. 44**): at ideal PEDOT/CNT ratio, almost *four times higher* photocurrents were recorded compared to the pristine PEDOT layers (see dashed line in **Fig. 44B**). Error bars were calculated from three different measurement in each cases. When less polymer was deposited on the conducting CNT network, the photocurrents were notably inferior, together with the cases, when the polymerization charge density exceeded the optimal value. When the amount of polymer was less than the optimal value, the surface of the nanotubes was not covered completely, and the electrodeposited polymer layer was too thin to absorb the illuminating light completely. When the PEDOT layer was thicker (more than 100 mC cm^{-2}), the PEC properties of the bulk polymer dominated, and the photocurrents approached the values measured for the pristine PEDOT.

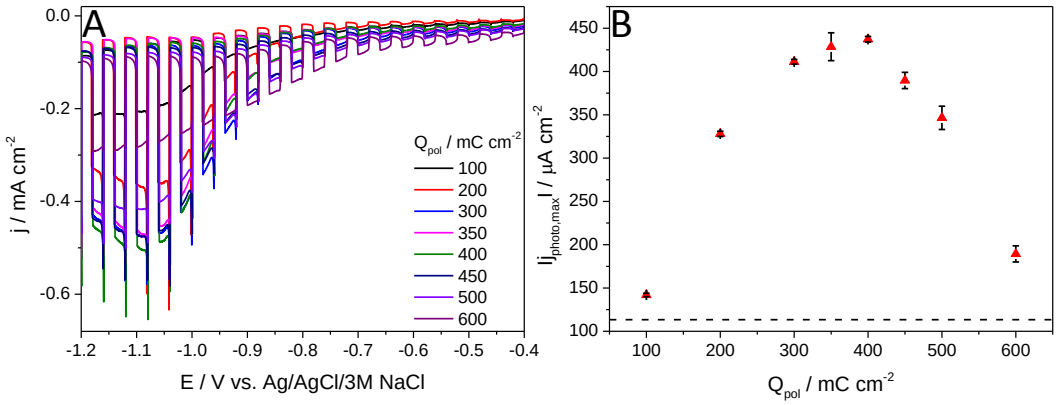

Fig. 44: (A) Comparison of the photovoltammograms recorded in Ar-saturated 0.1 M Na_2SO_4, for the nanocomposites prepared with different PEDOT/CNT ratio by varying the polymerization charge density (m_{CNT} = 60 µg cm^{-2}). Measurements were carried out applying 2 mV s^{-1} sweep rate, 0.1 Hz chopping frequency, and a solar simulator as the light source. (B) Maximum photocurrent vs. polymerization charge density plot, calculated from the data presented in (A). The dashed line marks the highest photocurrent, recorded for the best-performing bare PEDOT photoelectrode.

As the next step, the PEDOT/CNT ratio was held constant (at the one which gave the highest photocurrents) and the effect of the nanocomposite loading was investigated (**Fig. 45**). The photocurrent reached its maximum value at a CNT loading of 60 µg cm^{-2}. When the spray-coated amount of CNT was less, the effect of the CNT network could not prevailed, because only a very thin film formed on the Au surface, leading to smaller photocurrents. If the mass of the CNTs was above 60 µg cm^{-2}, the photocurrent values reached a plateau around the value measured previously for the best performing PEDOT/CNT nanocomposite photoelectrode

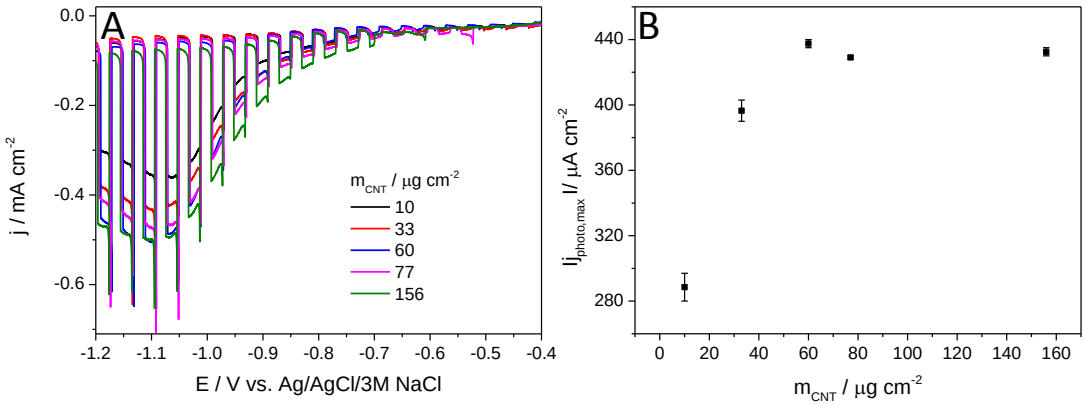

Fig. 45: (A) Comparison of the photovoltammograms recorded in Ar-saturated 0.1 M Na_2SO_4 for the nanocomposites prepared with the same PEDOT/CNT ratio, but varying the CNT loading. (B) Maximum photocurrent vs. spray-coated CNT mass plot, calculated from the data presented in (A). Measurements were carried out applying 2 mV s^{-1} sweep rate, 0.1 Hz chopping frequency, and a solar simulator as a light source.

The overall trend was similar for the graphene containing electrodes (**Fig. 46** and **Fig. 47**), but some differences can also be pointed out: the highest obtainable photocurrent was approximately 1.5 times smaller compared to the CNT-case (293 µA cm^{-2} vs. 437 µA cm^{-2}), but significantly less polymer was needed to reach the optimal PEDOT/graphene composition (200 mC cm^{-2}).

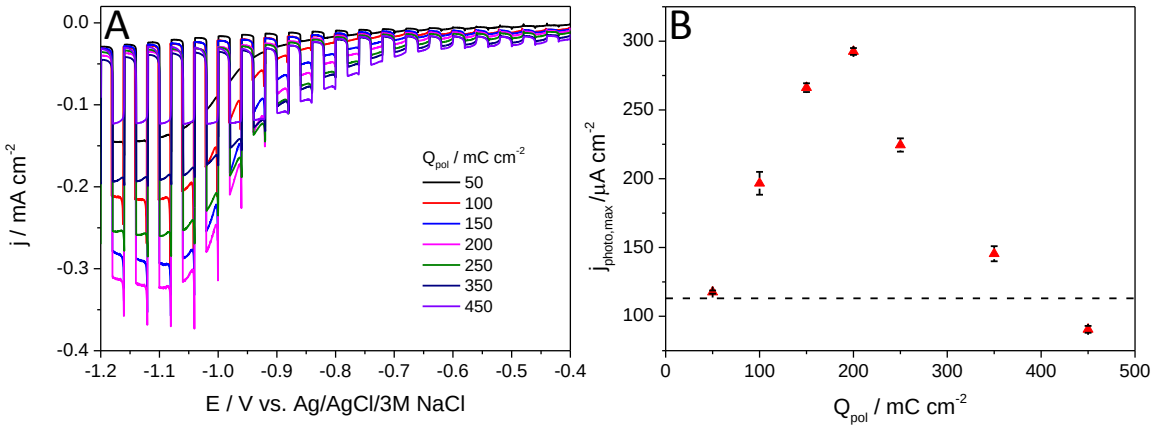

Fig. 46: (A) Comparison of the photovoltammograms recorded in Ar-saturated 0.1 M Na_2SO_4 for the nanocomposites prepared with different PEDOT/graphene ratio by varying the polymerization charge density ($m_{graphene}$ = 110 µg cm^{-2}). Measurements were carried out applying 2 mV s^{-1} sweep rate, 0.1 Hz chopping frequency, and a solar simulator as a light source. (B) Maximum photocurrent vs. polymerization charge density plot, calculated from the data presented in (A). The dashed line marks the highest photocurrent, harvested for the best-performing bare PEDOT photoelectrode.

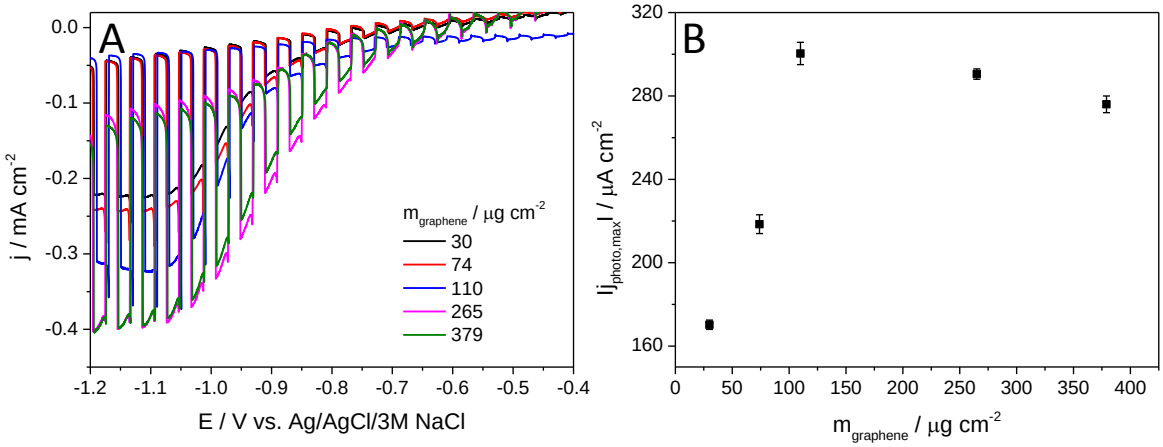

Fig. 47: (A) Comparison of the photovoltammograms recorded in Ar-saturated 0.1 M Na_2SO_4 for the nanocomposites prepared with the same PEDOT/graphene ratio, but varying the graphene loading. (B) Maximum photocurrent vs. spray coated graphene mass plot, calculated from the data presented in (A). Measurements were carried out applying 2 mV s^{-1} sweep rate, 0.1 Hz chopping frequency, and a solar simulator as a light source.

To study the effect of the nanocarbons on the light absorption properties of the nanocomposite samples, IPCE measurements were performed (**Fig. 48A**). The electrochemically active surface area of the nanocarbons were set to be identical (loadings: 60 μg cm^{-2} for CNT and 130 μg cm^{-2} for graphene – for more detailed information, see **Fig. 14**). The characteristics of the three curves are similar and the order of the maximum IPCE was in line with the photovoltammetry data (the highest values were measured for PEDOT/CNT, which was followed by the values, obtained for PEDOT/graphene and finally, PEDOT). The bandgap was calculated by fitting a linear to the cutoff region of each spectrum and extrapolating to the wavelength axis. A bandgap energy of 1.7 eV was estimated, which was similar for all three systems and is in good agreement with the literature values [172,173]. This is a direct evidence that the absorption range has not broadened in the case of the nanocomposites compared to the bare PEDOT, therefore it cannot be accounted for the enhanced PEC performance.

To determine the Fermi levels and to construct band energy diagrams for both PEDOT and the PEDOT/nanocarbon electrodes, Kelvin probe microscopy measurements were carried out, coupled with APS [145]. Similar E_{VB} values were found for all three systems: −4.49 eV for PEDOT, −4.45 eV for PEDOT/CNT and −4.40 eV for PEDOT/graphene (see the corresponding APS data in **Fig. 49A–C**). Fermi levels were calculated from the CPD measurements (**Fig. 49D–F**, described in detail in the Experimental Section). The E_F values fall close to the E_{VB} of all three systems, which is characteristic to p-type SCs [174]. Additionally, by electrodepositing PEDOT to the surface of both CNTs and graphene, E_F slightly shifted toward more negative energies. This trend can be explained with the more negative E_F values, of CNT ($E_{F,CNT}$ = −4.74 eV) and graphene ($E_{F,graphene}$ = −4.85 eV), moving $E_{F,nanocomposite}$ in between the E_F values, measured for its pristine counterparts (i.e., Fermi level equilibration). After obtaining both E_{VB} and E_F for all three systems, E_{CB} were calculated using the optical bandgap, determined from the UV−vis and IPCE measurements previously. Finally, band diagrams were constructed (**Fig. 48B**).

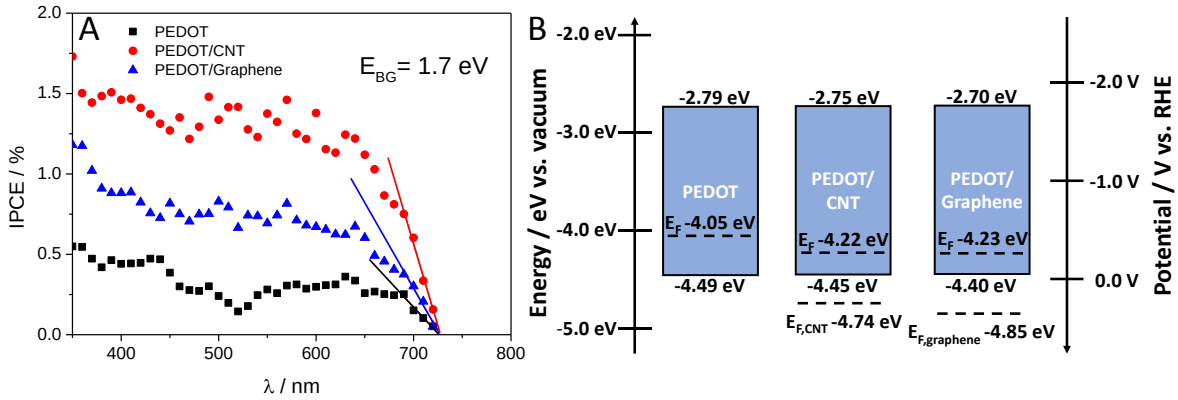

Fig. 48: (A) IPCE curves recorded for a PEDOT, a PEDOT/CNT and for a PEDOT/graphene photoelectrode; in 0.1 M Na_2SO_4 saturated with Ar at E = −1.0 V constant potential. (B) Band diagrams constructed for the three electrode materials.

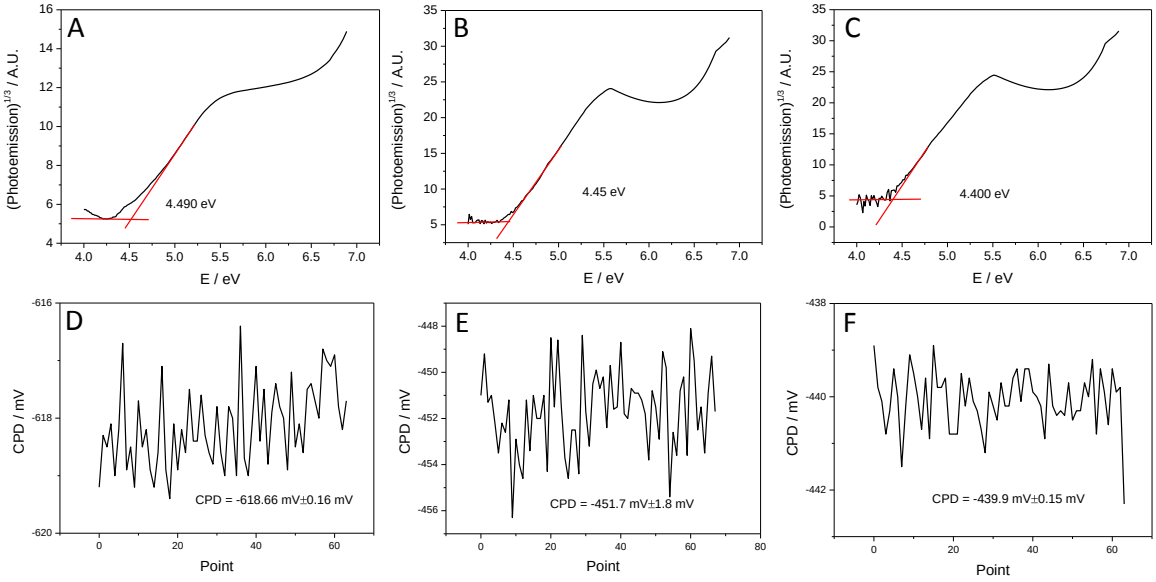

Fig. 49: APS measurements, recorded for (A) PEDOT (Q_{cutoff} = 50 mC cm^{-2}), (B) PEDOT/CNT (m_{CNT} = 60 µg cm^{-2}, Q_{cutoff} = 400 mC cm^{-2}) and (C) for PEDOT/graphene ($m_{graphene}$ = 110 µg cm^{-2}, Q_{cutoff} = 200 mC cm^{-2}). CPD measurements recorded for (D) PEDOT (Q_{cutoff} = 50 mC cm^{-2}), (E) PEDOT/CNT (m_{CNT} = 60 µg cm^{-2}, Q_{cutoff} = 400 mC cm^{-2}) and (F) for PEDOT/graphene ($m_{graphene}$ = 110 µg cm^{-2}, Q_{cutoff} = 200 mC cm^{-2}).

5.2.4 Electrochemical impedance spectroscopy

To study the effect of different nanocarbons on the electrical properties of the nanocomposites, EIS measurements were carried out. **Fig. 50A** shows the Nyquist plots recorded for the bare PEDOT and CNT layers, and for the PEDOT/CNT nanocomposites prepared with different PEDOT loadings. Similar data, recorded for PEDOT/graphene is shown in **Fig. 51**. In the case of PEDOT, a distinct semicircle was identified in the high-frequency range, corresponding to the charge-transfer limited process, whereas the linear

part, observed in the lower-frequency range can be assigned to the diffusion-limited electron-transfer process [175,176]. In the case of the CNT and graphene, a straight line with an almost 90° inclination and with a very small semicircle portion was observed. This is characteristic to the capacitive behavior of both nanocarbons [176].

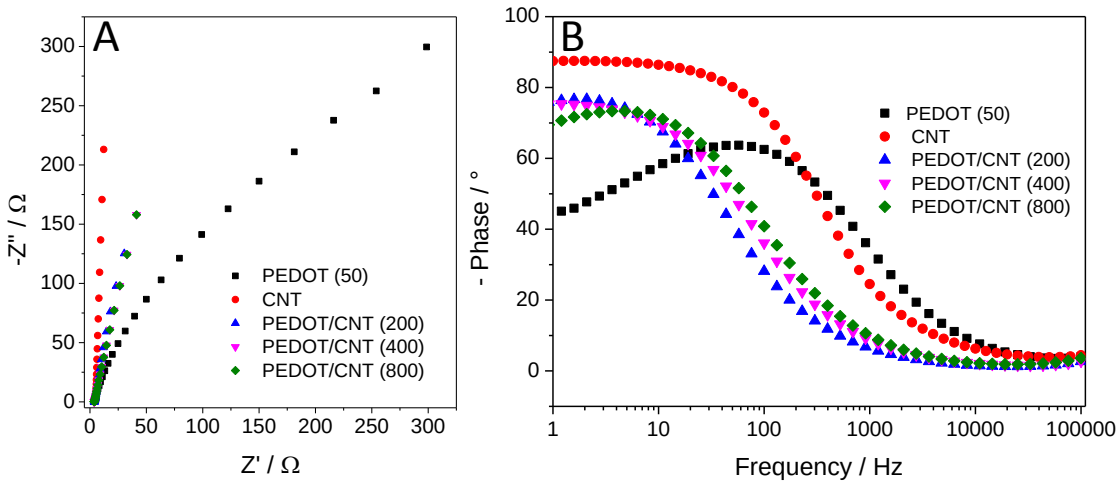

Fig. 50: (A) Nyquist plots recorded for PEDOT and PEDOT/CNT composites with varying PEDOT content, and (B) Bode plots recorded for PEDOT and PEDOT/CNT composites with varying PEDOT content. Data were recorded in 1 M Na_2SO_4 solution saturated with Ar at *E* = −0.9 V potential, in the 0.1 Hz-100 kHz frequency range. The values in the brackets are indicating the polymerization charge density (mC cm^{-2}) used to deposit the PEDOT layers.

There are two important trends upon composite formation: the diameter of the semicircle in the high-frequency range shrunk compared to the bare PEDOT, along with the inclination of the linear section of the curves, in the low-frequency range. These phenomena have been already discussed in the literature for both PEDOT /nanocarbon [177–179] and for other CP/nanocarbon electrodes [148,180]. By electrodepositing PEDOT on any type of conducting nanocarbon network, the electric conductivity of the nanocomposite layers improved compared to the polymer. This results in better charge carrier transport, therefore suppressed charge carrier recombination, which might explain the higher photocurrents in the case of the PEDOT/CNT and PEDOT/graphene layers in our study. The increasing thickness of PEDOT in both nanocomposites lead to semicircles with slightly larger diameters. However, the diameter of these semicircles in the high-frequency portion of the Nyquist-plots was less than ≈ 10 Ω, even when the highest amount of PEDOT was present on the CNT surface. These observations were also confirmed by the Bode-plots where the shape of the curves was almost identical for all three PEDOT/CNT nanohybrids

(**Fig. 50B** and **Fig. 51B** for the PEDOT/graphene system).

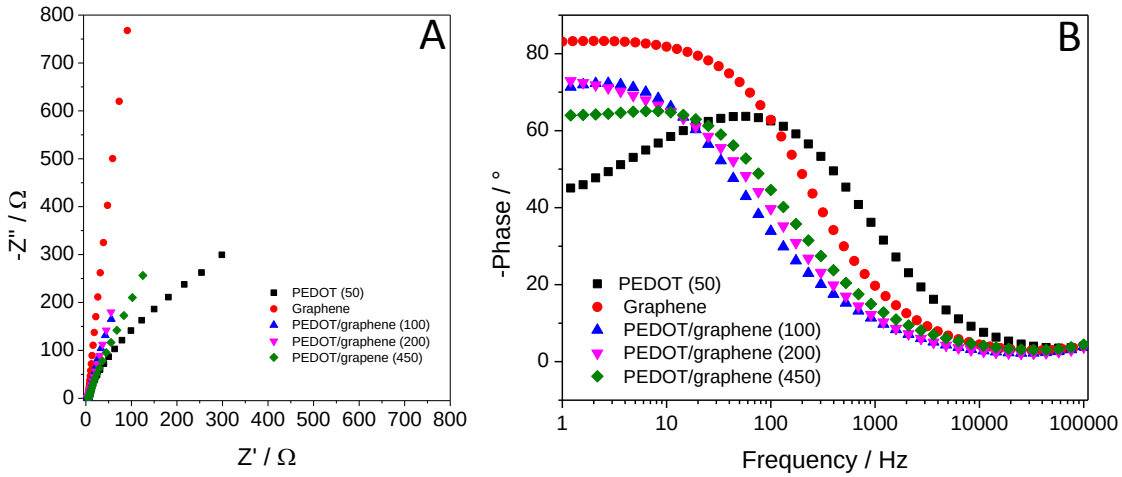

Fig. 51: Nyquist plots recorded for PEDOT and PEDOT/graphene composites with varying PEDOT content (A) and Bode plots recorded for PEDOT and PEDOT/graphene composites with varying PEDOT content (B), in 1 M Na_2SO_4 solution saturated with Ar at E = −0.9 V potential, in the 0.1 Hz-100 kHz frequency range. The values in the brackets are indicating the polymerization charge density (mC cm^{-2}) used to deposit the PEDOT layers.

These qualitative observations were quantified by fitting an equivalent circuit to the experimental data. The fitted equivalent circuit is discussed in detail in the Experimental Section (**Fig. 17**). Examples, regarding the precision of the fit are presented in **Fig. 52**. The calculated charge transfer resistance (R_{ct}) was 406 Ω for the pristine PEDOT, which value is higher than the ones, reported in the literature earlier. This difference can be explained by the fact that our EIS measurements were carried out at a potential (E = −0.9 V), where PEDOT was in its fully reduced state, instead of the open circuit conditions or potentials, where PEDOT is slightly or fully oxidized. The R_{ct} values were very small for the CNT and graphene (2 Ω and 5 Ω) films, verifying that these nanocarbons have high electrical conductivity. Electrodepositing PEDOT on the surface of the nanocarbon scaffolds only slightly changed their charge transfer properties (i.e., R_{ct} was less than 10 Ω in all cases). In conclusion, by electrodepositing PEDOT on the surface of both CNTs and graphene, the conductivity of these composites can be highly improved compared to the neat polymer, which might result in better charge carrier transport.

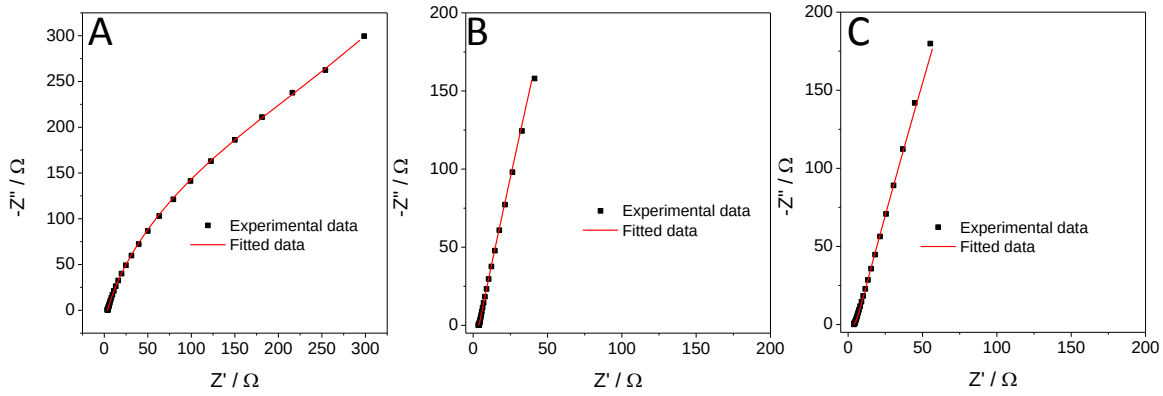

Fig. 52: Accuracy of the fit, using the equivalent circuit presented in **Fig. 17**, demonstrated on the data, recorded for a (A) PEDOT (Q_{cutoff} = 50 mC cm^{-2}), a (B) PEDOT/CNT (m_{CNT} = 60 µg cm^{-2}, Q_{cutoff} = 400 mC cm^{-2}), and (C) for a PEDOT/graphene layer ($m_{graphene}$ = 110 µg cm^{-2}, Q_{cutoff} = 200 mC cm^{-2}) in 1 M Na_2SO_4 solution saturated with Ar, at −0.9 V potential, in the 0.1 Hz to 100 kHz frequency range.

5.2.5 Long-term photoelectrolysis

The photostability of both the bare PEDOT and the PEDOT/nanocarbon photoelectrodes was investigated by long-term chronoamperometry measurements. In the case of the PEDOT layers, a photocurrent transient evolved right after illuminating the electrode surface, which was followed by a rapid decay in the photocurrent. The photocurrent reached its steady-state value after 50 − 60 min (10 − 15 µA, black curve in **Fig. 53A**). Similar characteristics can be identified on the curves, measured for both the PEDOT/CNT and the PEDOT/graphene layers (red and blue curves in **Fig. 53A**), but the values of the steady-state photocurrents are higher, compared to the pristine PEDOT (≈ 20 − 30 µA).

To quantify the evolved product(s) during the long-term PEC measurements, gas chromatographic analysis was performed. Only hydrogen was identified in the gas phase for all systems, the amount of which gradually increased during the photoelectrolysis (**Fig. 53B**). The lower stability of the PEDOT/CNT layers were also reflected in the smaller amount of the hydrogen evolved during the experiments, compared to the PEDOT/graphene system. The Faradaic efficiency was between 80 − 100% in all cases.

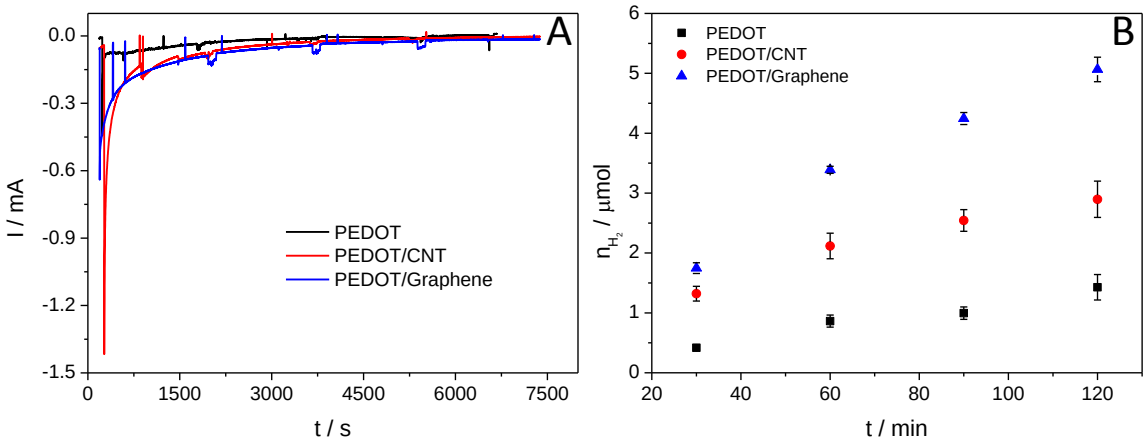

Fig. 53: (A) Long-term chronoamperometry data registered for PEDOT, PEDOT/CNT and PEDOT/graphene layers, at *E* = −1.0V potential (vs. Ag/AgCl/3M M NaCl) in 0.1 M Na_2SO_4, saturated with Ar. A solar simulator was used as a light source. (B) Amount of H_2 formed during the photoelectrolysis experiments, presented in (A).

5.2.6 Photoelectrochemistry of polyaniline/nanocarbon electrodes

The previously presented methodology can be applied to other CPs too. Therefore, as a next step, PANI/CNT and PANI/graphene nanocomposite electrodes were synthesized. For the sake of brevity, only the most relevant results are presented here.

Similar morphological characteristics can be identified in the case of the PANI/ nanocarbon hybrids as shown for the PEDOT/nanocarbon composites. The surface of both the CNTs and the graphene flakes are evenly coated with the polymer (**Fig. 54A-E**). The histogram, presented in **Fig. 54F**, shows that the PANI thickness was dominantly in the 25 – 50 nm range (38 ± 12 nm). This observation stands for the layers, where the polymerization charge density was 100 mC cm^{-2}. Analogous conclusions can be made for the PANI/graphene nanocomposites. PANI has coated the surface of the nanoflakes evenly, however the presence of the PANI layer is less conspicuous. The only was the higher roughness of the nanosheets in the case of the nanocomposites, and a few fiber-like structures extended from the surface of the graphene layers, corresponding to PANI.

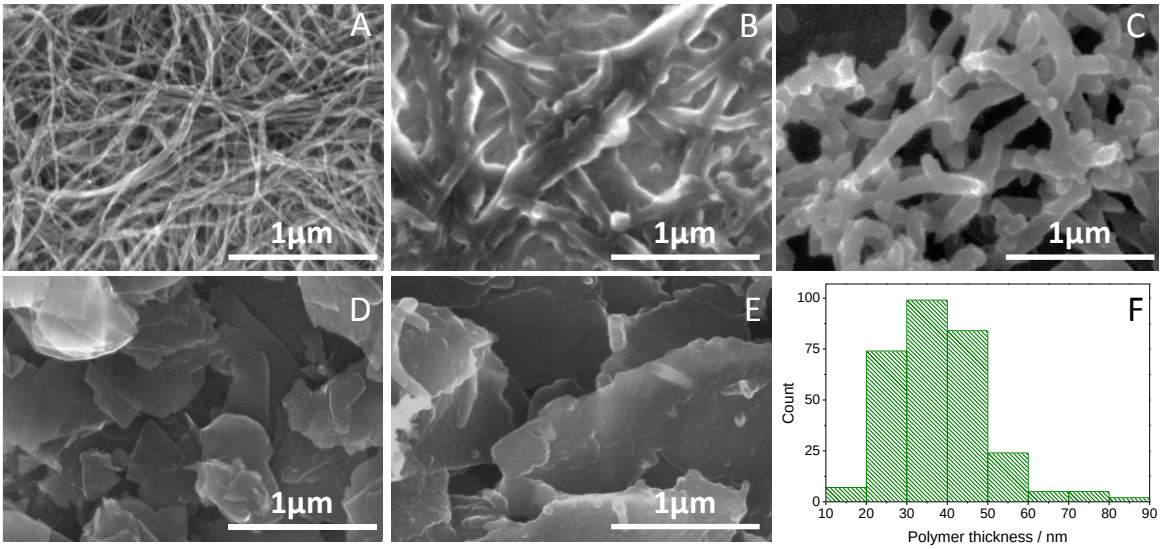

Fig. 54: SEM images of (A) bare CNT layer on Au (m_{CNT} = 100 µg cm^{-2}), (B) PANI/CNT nanocomposite layer on Au (m_{CNT} = 100 µg cm^{-2}), Q_{pol} = 150 mC cm^{-2}, (C) pristine PANI layer on Au, Q_{pol} = 150 mC cm^{-2}, (D) graphene layer on Au (m_{CNT} = 60 µg cm^{-2}), and (E) PANI/graphene layer on Au (m_{CNT} = 60 µg cm^{-2}), Q_{pol} = 300 mC cm^{-2}. (F) PANI thickness distribution calculated from (A) and (B).

The performance of the photoelectrodes was optimized following the strategy described for the PEDOT/nanocarbon electrodes (**Fig. 55A** and **Fig. 56A)** Measurements were carried out in both N_2-saturated 0.1 M Na_2SO_4 and in CO_2-saturated 0.1 M $NaHCO_3$ solutions. The shape of the photovoltammograms was identical to the ones, registered for the bare PANI electrodes (**Fig. 26**). The maximum photocurrent varied like a maximum-curve, the highest values were obtained when the polymerization charge density reached 100 mC cm^{-2} (**Fig. 55B** and **Fig. 56B**). The achieved photocurrents were slightly smaller than in the PEDOT/nanocarbon case, but followed the same order. The smallest photocurrents were detected in the case of the bare PANI, which was followed by PANI/graphene, and the highest ones were obtained for PANI/CNT layers. When the effect of the nanocarbon loading was studied, the shape of the obtained maximum photocurrent vs. $m_{nanocarbon}$ plot was similar to the one, constructed in the case of the PEDOT/nanocarbon photoelectrodes.

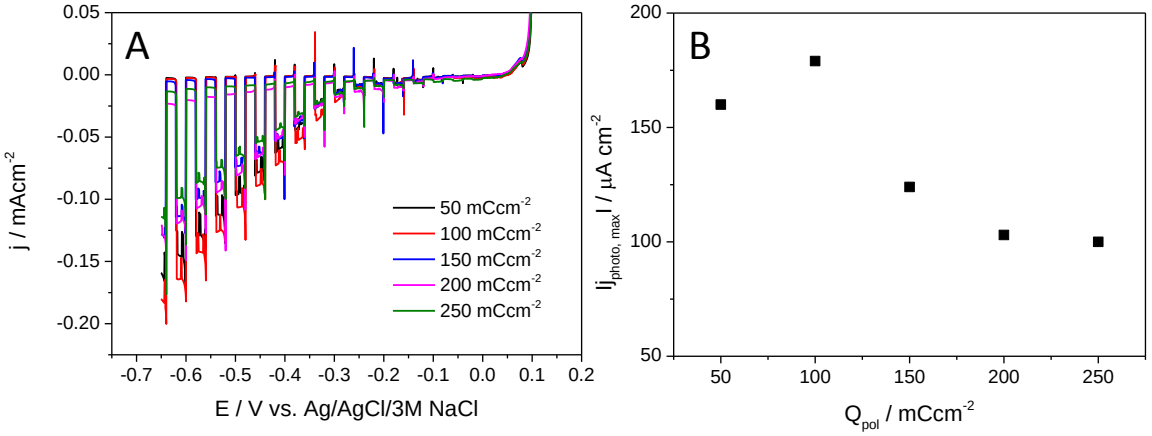

Fig. 55: (A) comparison of the photovoltammograms, recorded in N_2-saturated 0.1 M Na_2SO_4 for the nanocomposites prepared with different PANI/CNT ratio by varying the polymerization charge density (m_{CNT} = 100 µg cm^{-2}) 2 mV s^{-1} sweep rate, 0.1 Hz chopping frequency, 300 W Hg-Xe lamp. (B) Maximum photocurrent vs. polymerization charge density plot, calculated from the data presented in (A).

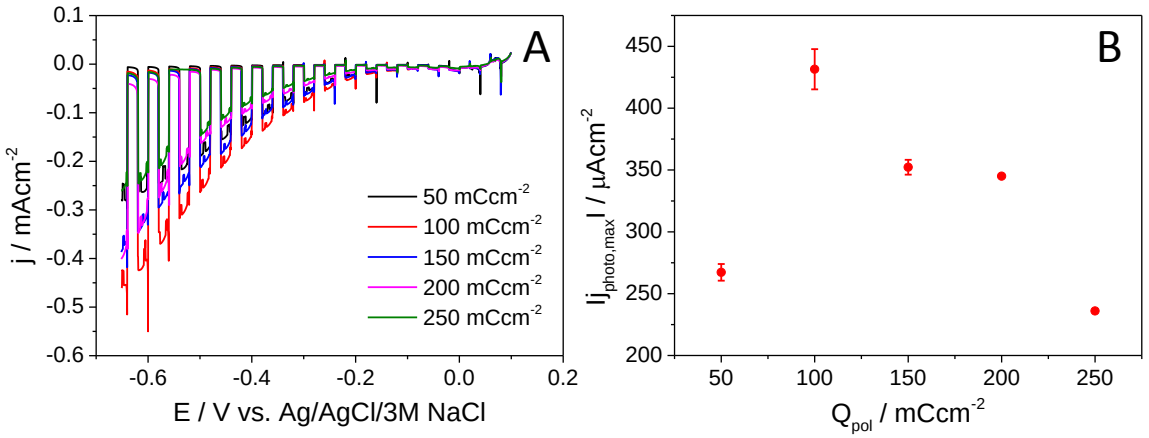

Fig. 56: (A) comparison of the photovoltammograms, recorded in CO_2-saturated 0.1 M $NaHCO_3$ for the nanocomposites prepared with different PANI/CNT ratio by varying the polymerization charge density (m_{CNT} = 100 µg cm^{-2}) 2 mV s^{-1} sweep rate, 0.1 Hz chopping frequency, 300 W Hg-Xe lamp. (B) Maximum photocurrent vs. polymerization charge density plot, calculated from the data presented in (A).

To glean further insights on the charge carrier recombination process, transient PEC measurements were performed (**Fig. 57**) [152,153]. The most important goal was to elucidate the effect of the nanocarbons in these nanocomposite systems. In a N_2-saturated solution, a sharp transient emerged, followed by a slow decay of the generated photocurrent. Contrastingly, when the solution was saturated with CO_2, smaller spikes were observed both for the pristine polymer and the nanocomposites. Furthermore, both conducting nanoscaffolds had unequivocal effect on the shape of the transients. On one hand in the case of the PANI/CNT nanocomposite, the value of the steady-state

photocurrent increased. However the size of the spike was slightly bigger compared to the pristine polymer. On the other hand, in the case of the PANI/graphene layer, the increase in the photocurrent was less pronounced, but below −0.5 V applied potential, almost no spike could be seen.

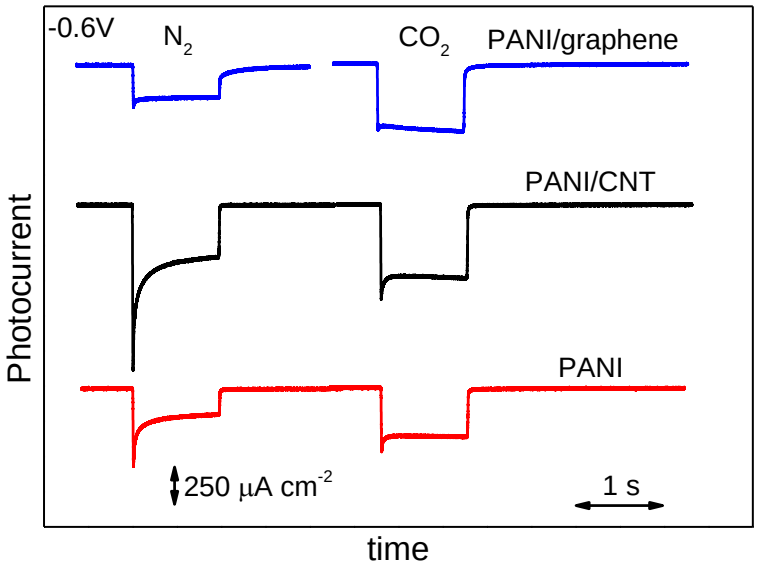

Fig. 57: Photocurrent transients recorded for a PANI, PANI/CNT and PANI/graphene layers in both N_2-saturated 0.1 M Na_2SO_4-, and CO_2-saturated 0.1 M $NaHCO_3$ solutions (the pH of both solution was ≈ 7.0), at E = −0.6 V potential. A 300 W Hg-Xe lamp was used as a light source and the time of illumination was 1 s in each case. The polymerization charge density was 150 mC cm^{-2} in all cases, and the electrochemically active surface area of both spray-coated nanocarbons was identical.

To quantify these observations, the transient photocurrent curves were fitted, and time constants were determined for all three systems. The transient photoresponse curves can be described by a simple binomial exponential function (see Equation 2). Interestingly, the profile of the curves and the τ_2 values are similar for all three systems, but there was a notable difference between the results, measured in N_2-, and CO_2-saturated solutions (**Fig. 58**). When the electrode surface is illuminated, after the charge separation process, the photogenerated minority carriers (electrons) are driven toward the electrode/electrolyte interface by band bending, and the holes rapidly travel toward the supporting Au electrode surface. *This latter process can be affected* by the conducting CNT-, and graphene networks underneath the PANI layer by accelerating charge-carrier transport. The plotted time constants are in the ms timescale, but bulk electron-hole recombination processes usually occur on the ns timescale [154], that is the reason why almost no difference can be seen

between the behavior of the three systems. However, a huge difference was experienced in the values of the steady-state photocurrents, which is a strong evidence, that the highly conducting carbon nanostructures facilitated the transport of the photogenerated charge carriers. When the solution was saturated with N_2, the more negative potential resulted in higher time constants, which means that the decay of the generated photocurrent was slower, in other words; the recombination was suppressed by the increasing outer constraint (higher negative potential). On the other hand, in the CO_2-saturated solutions the time constants were almost identical in the whole investigated potential window. The explanation to this phenomenon is that a faster process occurred, which syphoned the photogenerated charge carriers from the electrode/electrolyte junction. This might be in connection with the selective adsorption and PEC reduction of CO_2 on the electrode surface, however detailed mechanistic insights are still to be explored.

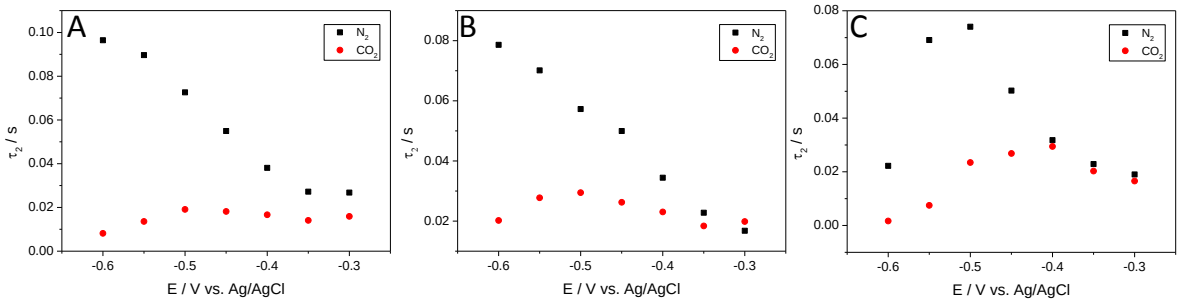

Fig. 58: Potential dependence of the τ_2 time constants derived for (A) a PANI, (B) a PANI/CNT and (C) a PANI/graphene photoelectrode. The transient PEC measurements were carried out in N_2-saturated 0.1 M Na_2SO_4-, and CO_2-saturated 0.1 M $NaHCO_3$ solutions (the pH of both solution was ≈ 7.0). A Hg-Xe lamp was used as a light source and the time of illumination was 1 s in each case. The polymerization charge density was 150 mC cm^{-2} in all cases, and the surface area of both spray-coated nanocarbon was identical.

5.3 Controlled photocatalytic synthesis of core-shell polyaniline/SiC hybrid nanostructures

Two major drawbacks have been identified if CPs alone are used as photoelectrodes: low conductivity and poor photostability. Conductivity issues have been successfully addressed by electrodepositing CPs on a conducting nanocarbon matrix, however photostability was not improved. In the following, a different approach is presented, where a robust, stable inorganic SC is used and the CPs is only added to the system to act as co-catalyst, which might result in enhanced PEC properties. Results on the various synthesis strategies and PEC behavior of PANI/SiC nanocomposite photoelectrodes are presented in the last two chapters.

5.3.1 Synthesis of the core-shell nanocomposites

PANI/SiC core-shell nanocomposites were first obtained via photocatalytic deposition (**Fig. 59**). In this process, SiC nanoparticles were dispersed in the solution of the aniline monomer and the sulfuric acid supporting electrolyte, stirred constantly, ensuring that the incident photon flux reached evenly the surface of the SiC nanoparticles. As a result of UV-vis light irradiation, electron-hole pairs are formed in the SiC nanoparticles. After charge separation, some of the photogenerated charge carriers reach the particle surface before they could recombine. These charge carriers can initiate various reactions at the SiC/electrolyte interface. In our case, the holes oxidized the aniline monomers, generating radical cations, which first formed oligomers in the solution, close to the surface of the SC nanoparticles. After that a constant (few nm thick) polymer coating deposited on the surface of the nanoparticles. In parallel, the photogenerated electrons react with dissolved O_2, which is present in the solution as an e^- scavenger. The polymerization can be terminated in two ways: either by turning off the illumination, or by coating evenly the surface of the SiC nanoparticles with the PANI film, which cause optical shielding by absorbing the irradiating light.

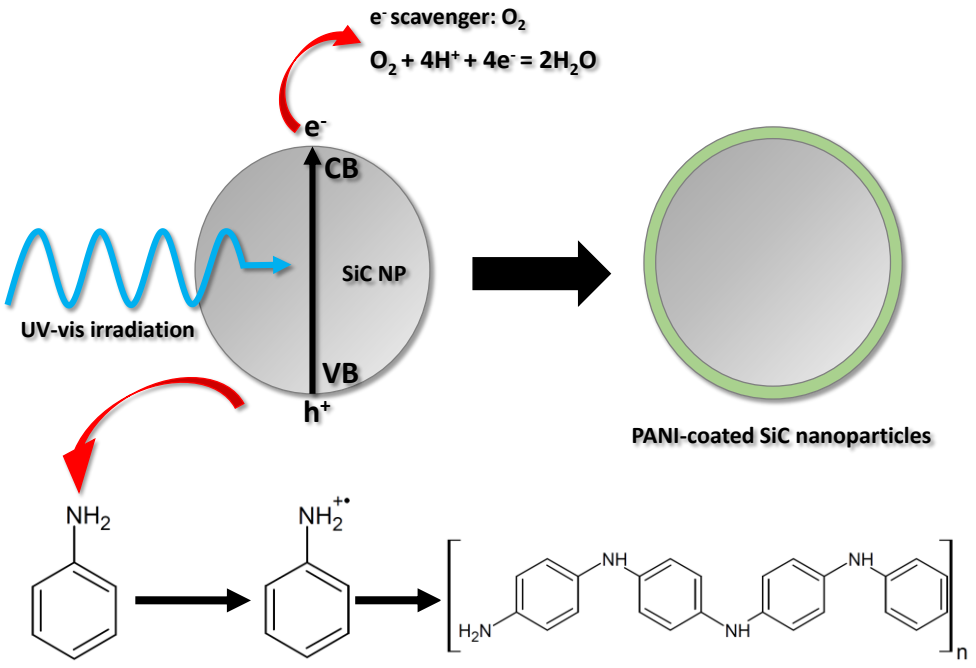

Fig. 59: Schematic illustration of the PANI/SiC nanocomposite synthesis.

Nanocomposites were synthesized using two types of illumination: a 'UV-filtered' (the irradiation below 300 nm was filtered out) and a 'UV-illuminated' (the full UV-vis lamp output was used). The first spectacular difference between the different illuminations manifested in the color of the solution after centrifuging the PANI/SiC nanoparticles. The one, irradiated with the full lamp output, turned dark red, while the other one remained almost transparent. After centrifuging and filtering, the UV-vis spectra of the two residual solutions were measured (**Fig. 60**). Beyond the obvious low-wavelength band of the monomer, two wide bands appeared in the case of the UV-illuminated sample: one corresponds to the formed oligomers with low segment number, the other one to the polymer fragments in the solution [181]. Contrastingly, on the spectrum recorded for the UV-filtered sample, there is no band which could correspond to the polymer/oligomers. There are at least three possible factors contributing to these observations: i) because of the hard-UV illumination more polymer forms and the excess stays in the solution causing the dark reddish color, ii) upon hard-UV illumination, aniline is directly photopolymerized in the solution; iii) finally it is also possible that the high energy UV-illumination degrades PANI, already formed on the SiC surface of the nanoparticles, which thus may leach to the solution.

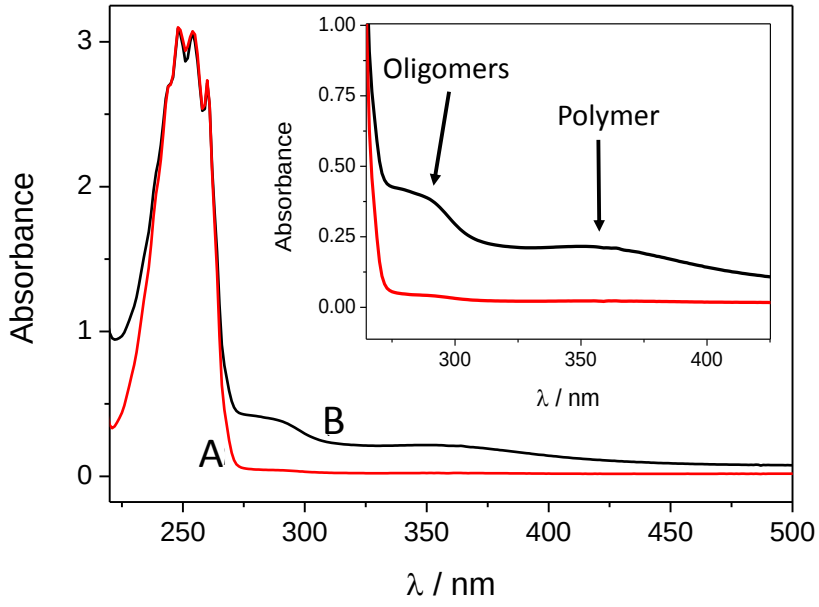

Fig. 60: UV-vis spectra of the filtered and centrifuged polymerization dispersions after 60 min illumination. (A) UV-filtered (B) UV-illuminated case.

TGA was employed to determine the amount of the formed PANI after certain irradiation time periods, and thus to assess the composition of the various nanocomposite samples. As a first step, the pure SiC was studied, where an 18% mass increase was observed between 330 °C – 800 °C, attributed to the oxidation of SiC nanoparticles (black line in **Fig. 61A**). As for the pure PANI sample, two major decomposition steps occurred in the range of 25 – 660 °C. In the first step (25 – 275 °C), the weight loss of 22 % can be attributed to the water and SO_x desorption (from the HSO_4^- dopant ions) from the sample. In the second step (275 – 660 °C), the complete oxidation of the polymer backbone was observed (blue trace in **Fig. 61A**) [182].

For all PANI/SiC composites (**Fig. 61B**), a two-step weight loss was occurred in the range of 25 °C – 485 °C attributed to the thermal degradation of PANI and a two-step weight increment due to the oxidation of SiC in the range of 330 °C – 800 °C. The TG curves are the superposition of those observed for the pure materials (presented in **Fig. 61A**). In the first step (25 – 250 °C), the water and dopant content desorbed, followed by the degradation of the PANI polymer chain in the range of (250 – 500 °C). As the irradiation time was increased from 5 min to 60 min, the maximum weight loss (at elevated temperatures) increased from 1.9 % to 3.9 % showing the gradually growing portion of PANI in the composites (**Fig. 61C**). In addition, at elevated temperatures (330 – 800 °C), the oxidation of SiC occurred in a two-step process, as opposed to pure SiC, where only one step oxidation was witnessed. We

suspect that some carbon-based residual of PANI may influence the oxidation and sintering of SiC nanoparticles.

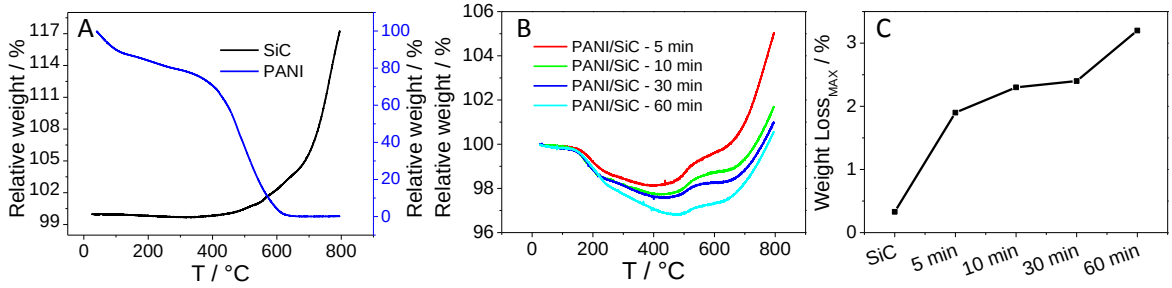

Fig. 61: TGA curves recorded in air for (A) SiC, PANI, (B) and the various PANI/SiC hybrids. (C) Comparison of the PANI content of the various PANI/SiC hybrids.

5.3.2 Structural characterization

Raman spectra of the core-shell PANI/SiC nanoparticles (the irradiation was cut below 300 nm), the bare SiC, and the pure PANI are compared in **Fig. 62A**. There are three strong bands on the spectrum of the SiC nanoparticles (curve 'a'). The one, centered at 790 cm^{-1} is attributed to the lattice-vibration of the material, specifically to the zone-center transverse optical (TO) phonons of 3C-SiC [183]. There are two additional characteristic bands, centered at 1334-, and at 1595 cm^{-1}, corresponding to the vibrational properties of isolated carbon arrangements [183,184], indicating the presence of carbon traces in the sample.

The characteristic Raman bands of PANI are summarized in **Table 3**. The bands, appearing on the spectra of the nanocomposite samples are marked with grey. In the series of spectra with increasing illumination time (b – e), the quantity of the deposited polymer increases. Note that the intensity ratio of the bands, centered at 1334-, and 1595 cm^{-1} completely flipped over (because these bands are overlapping with the bands of the deposited PANI). In addition, most of the characteristic bands of PANI appeared on the spectra of the nanocomposite, proving the formation of the PANI/SiC hybrid. If the hard UV-component of the illumination was not removed, some of the characteristic bands can still be identified (others are completely vanished), but with a much smaller intensity (**Fig. 62B**).

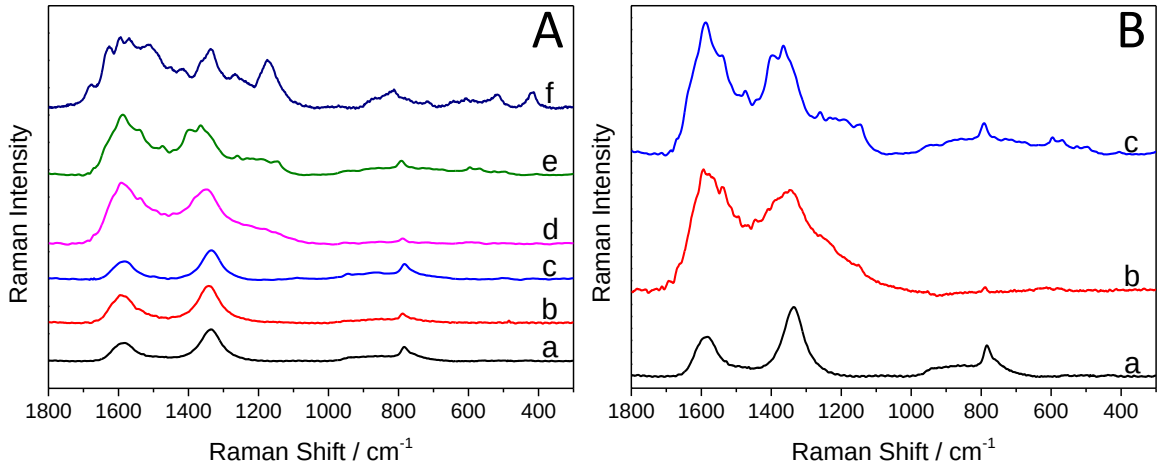

Fig. 62: (A) Raman spectra of the synthesized nanocomposite samples (having the UV component filtered below 300 nm). a.) SiC as-is, b.) PANI/SiC 5 min of illumination, c.) PANI/SiC 10 min of illumination, d.) PANI/SiC 30 min of illumination, e.) PANI/SiC 60 min of illumination, f.) PANI. (B) Raman spectra of the synthesized nanocomposite samples. a.) SiC as-is, b.) PANI/SiC 60 min of illumination, UV-illuminated c.) PANI/SiC 60 min of illumination, UV-filtered.

Table 3: Characteristic Raman bands of PANI. The bands appearing on the spectra of the SiC/PANI nanocomposites are marked with grey.

Wavenumber / cm^{-1}	**Assignment** [185–187]
517	Amine in-plane deformation
610	Ring deformation
720	Imine deformation
818	Amine deformation (C-N-C bending)
868	Ring deformation
1180	C–H bending in leucoemeraldine
1418	C–C stretching in quinoid type ring
1595	C–C stretching in quinoid type ring
1625	C–C stretching in benzene type ring

IR spectra of the synthesized samples with the longest irradiation time (60 min) are presented in **Fig. 63**. In the spectra of SiC (black curve) only one sharp, characteristic band is visible, which corresponds to the Si–C stretching vibration, and there is an additional rather weak band, centered around 1090 cm^{-1}, which can be assigned to the stretching vibration of Si–O–C and Si–O–Si bonds [132]. **Table 4** contains the characteristic IR vibrations of PANI, with the bands appearing on the spectra of the PANI/SiC

nanocomposites, marked with grey. Note that on the spectra of the UV-illuminated composite there are no characteristic PANI peaks, which may indicate that the deposited polymer layer is overoxidized. Contrastingly, almost all the characteristic bands of the PANI appear on the spectra of the UV-filtered sample, which is another direct evidence that this milder synthesis procedure results in SiC/PANI nanocomposites containing PANI with a conjugated structure.

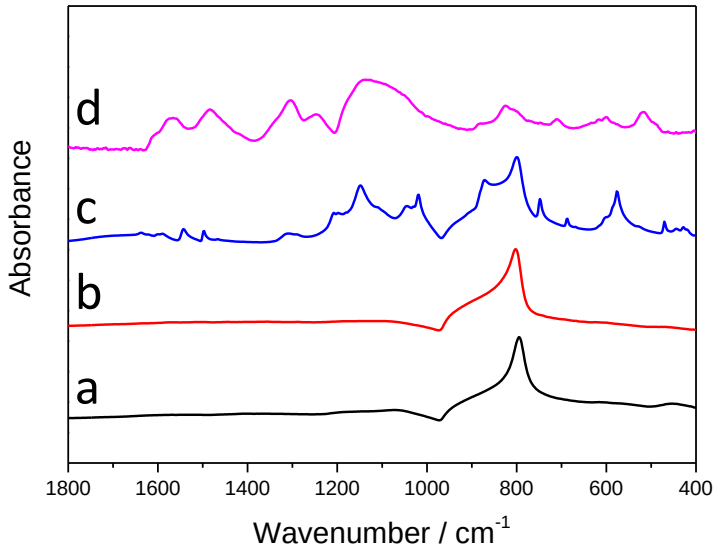

Fig. 63: IR spectra of the synthesized nanocomposite samples and their components. a.) SiC, b.) SiC/PANI 60 min UV-illuminated, c.) SiC/PANI 60 min UV-filtered d.) bare PANI.

Table 4: Characteristic IR bands of PANI. The bands appearing on the spectra of the nanocomposites are marked with grey.

Wavenumber / cm^{-1}	**Assignment** [188,189]
515	Aromatic ring deformation
828	C–H out-of-plane bending benzenoid type ring
882	C–H out-of-plane bending
1070	NH_2 rocking, ring deformation
1146	C–H in-plane-bending, ring deformation
1246	C–N stretching
1304	C–N stretching
1485	Benzenoid type ring stretching
1568	Quinoid type ring stretching
1610	N–H bending

5.3.3 Morphological characterization

The morphological characteristics of the PANI/SiC samples were first investigated by TEM. **Fig. 64** shows TEM images recorded for the pristine SiC and for the PANI/SiC nanocomposites, synthesized with the shortest (5 min) and longest (60 min) irradiation time. The size of the pristine SiC nanoparticles is diverse, with an average diameter is around $d_{SiC} \approx 50$ nm (**Fig. 65**). The first conspicuous difference between the SiC and the nanocomposite samples is that the degree of aggregation was higher in the PANI-containing materials, despite the thorough mixing during the synthesis. The images, taken at higher magnification, allowed us to visualize both the lattice fringes of the SiC nanoparticles and the deposited PANI, as a few nm thick amorphous film, on the surface of the NPs. Note that in the case of the pristine SiC, the lattice fringes were visible till the edge of the nanoparticles, but in the case of the nanocomposites an outer shell could be spotted, corresponding to the formed PANI film.

The thickness of the deposited polymer layer was also determined. **Fig. 66** shows the distribution of the thickness of the PANI shells, thus allowing quantitative comparison. With increasing illumination time, the average film thickness was increasing as well (from 1.0 to 2.5 nm), indicating that the thickness of the deposited PANI can be regulated by varying the time of the illumination. In addition, the formed PANI also glued together the individual SiC nanoparticles, as seen in the HR-TEM images (**Fig. 64 D, E**). Importantly, there was no major difference between the thicknesses of the synthesized PANI layers deposited with different light irradiations.

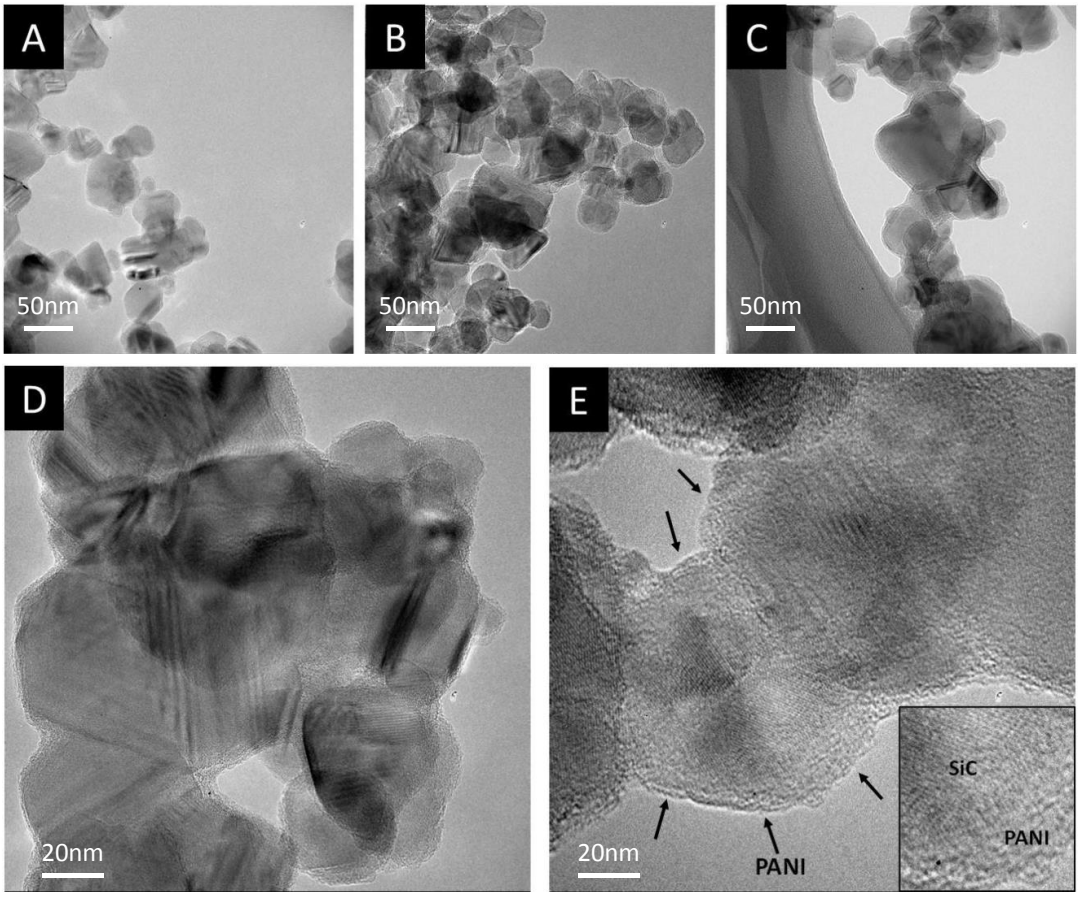

Fig. 64: TEM images, captured for (A) SiC, (B) PANI/SiC after 5 min of illumination, (C) PANI/SiC after 60 min of illumination. (D), (E) HR-TEM images taken for the PANI/SiC nanocomposite synthesized with 60 min of irradiation.

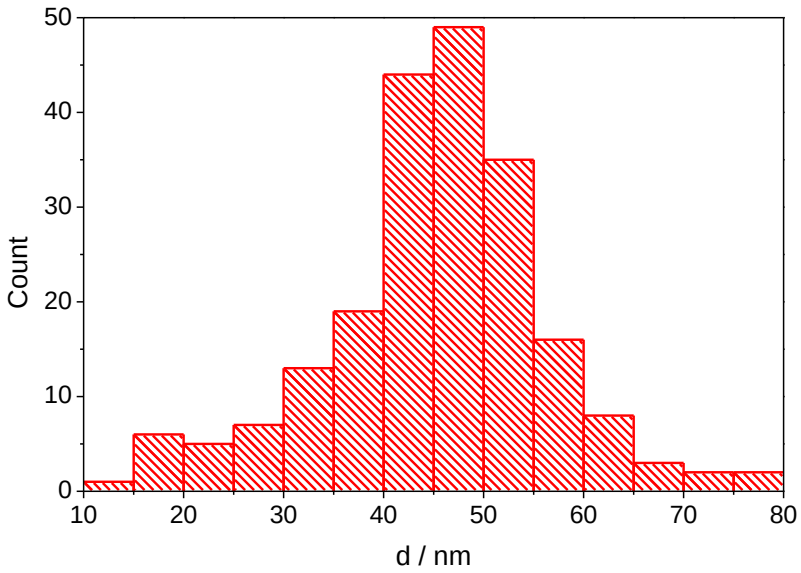

Fig. 65: Size distribution of the pristine SiC nanoparticles, derived from TEM measurements.

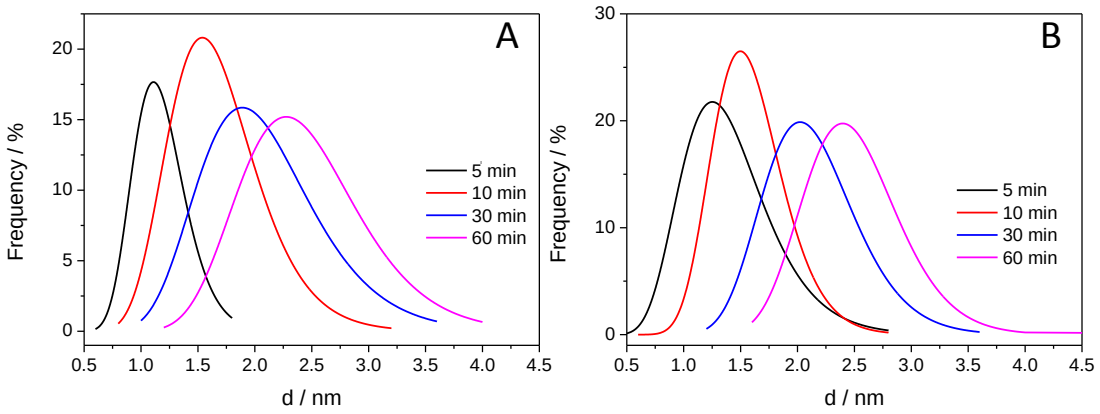

Fig. 66: Distribution of the PANI layer thickness on the various samples. (A) UV-irradiated samples, (B) UV-filtered samples.

After determining the particle size and the thickness of the polymer film on the SiC particles from the TEM investigations, SEM images were taken to characterize the overall morphology of the samples. **Fig. 67** shows SEM images for SiC and for the two hybrid PANI/SiC samples, synthesized by the longest irradiation time (60 min), differing only in the type of irradiation. As shown in **Fig. 67A**, the pristine SiC sample had a granular morphology, where the individual nanoparticles can be spotted. Contrastingly, on the other two images (**Fig. 67B** and **C**), a more coherent structure can be seen, where the polymer covered the SiC nanoparticles. In addition, it seems that PANI deposited not only on the surface of the nanoparticles, but also among the particles, thus glued them together.

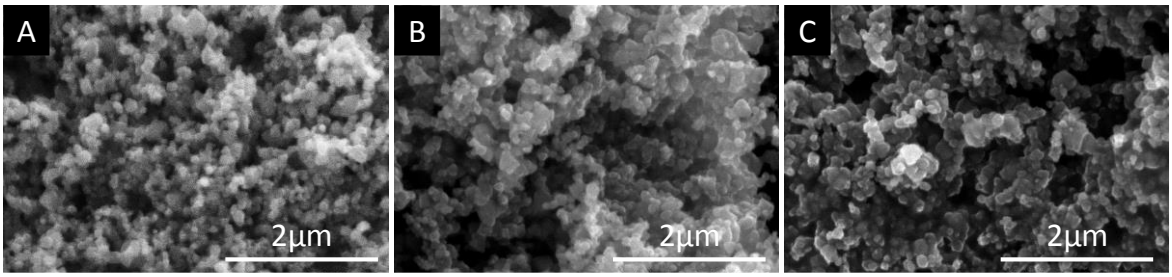

Fig. 67: SEM images, taken for (A) SiC, (B) PANI/SiC UV-irradiated sample (60 min), (C) SiC/PANI UV-filtered sample (60 min).

5.3.4 Cyclic voltammetric analysis

The electrochemical behavior of the PANI/SiC samples was probed by cyclic voltammetry (**Fig. 68**). SiC showed only limited electroactivity in this potential window (red curve), which was comparable with the current densities measured for the PANI/SiC sample prepared under full UV-irradiation. However, the shape of this latter voltammogram (blue curve) is

more characteristic: it has one anodic and one cathodic peak. If the synthesis procedure was milder (UV-filtered), the shape of the voltammogram clearly exhibits the features of the electrochemical transformation of PANI [70,71]. The most important conclusions to be drawn from these observations is that the PANI/SiC nanocomposite, prepared by UV-filtered light irradiation was much more electroactive, compared to its counterpart prepared using the full output of the lamp. This observation is in perfect agreement with the vibrational spectroscopic data presented above, namely that the hard UV-component degraded the conjugated structure of PANI.

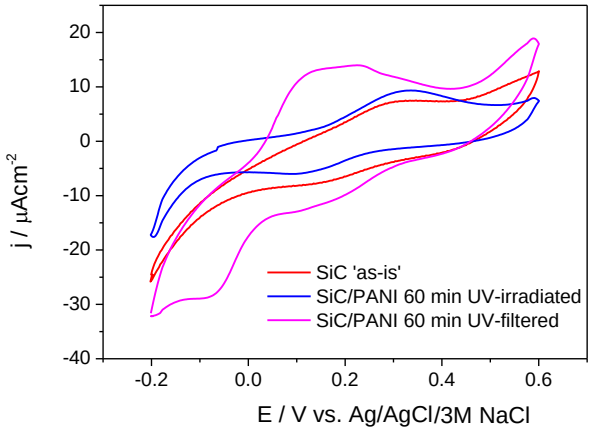

Fig. 68: Cyclic voltammograms of the SiC nanoparticles and the synthesized nanocomposites recorded in 0.5 M H_2SO_4 at a sweep rate of 25 mV s^{-1}.

We demonstrated how photoexcitation of SiC nanoparticles can be used to deposit a CP coating on the particle's surface. The presented photocatalytic polymerization is a facile and versatile approach to obtain hybrid organic/inorganic SC assemblies. The most important advantage of synthesizing nanocomposites by photocatalytic deposition is that perfectly covered SC nanoparticles can be obtained, and the thickness of the CP layer can be easily tuned. On the other hand, the electroactivity of the nanocomposites suggests that the contact between the nanocomposite and the substrate electrode was rather poor. Therefore, a different method/setup has to be used by which a much better contact can be achieved between the nanocomposite and the substrate electrode. One possible solution is to immobilize the SC nanoparticles on the substrate electrode surface by for example, spray-coating and subsequently deposit the CP on this SC-modified electrode by electrodeposition. Results corresponding to the electrosynthesis and PEC properties of PANI/SiC photoelectrodes, synthesized by employing this method are presented in the next chapter.

5.4 Electrosynthesis and photoelectrochemical properties of polyaniline/SiC nanohybrid electrodes

5.4.1 Electrodeposition of polyaniline on SiC-modified electrodes

After preparing the SiC-modified GC electrodes by spray-coating, PANI was electrodeposited by potentiodynamic cycling (**Fig. 69**). There was no observable difference between the polymerization curves, recorded during the electrodeposition of PANI on a GC-, and a SiC-coated GC-electrode. Because of the higher surface area of the SiC-coated electrodes, however, the same amount of polymerization charge passed through within less cycles compared to the unmodified GC electrode.

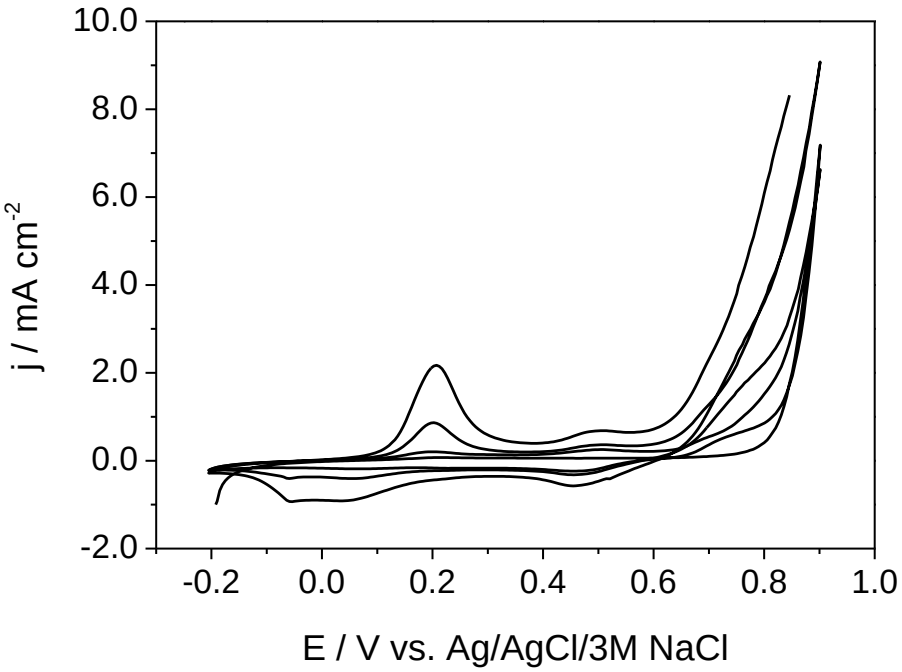

Fig. 69: Potentiodynamic polymerization curve, recorded during the electrodeposition of PANI on a SiC-coated GC electrode (m_{SiC} = 0.4 mg cm^{-2}). The polymerization solution contained 0.2 M aniline and 0.5 M H_2SO_4. Q_{pol} = 40 mC cm^{-2}, υ = 100 mV s^{-1}.

Nanocomposites with three different CP/SiC ratios were synthesized (10, 20, and 40 mC cm^{-2} polymerization charge density). The electroactivity of the nanocomposite electrodes was probed by CV scans, recorded in N_2-saturated 0.1 M Na_2SO_4 (**Fig. 70A** and **B**). After determining the area of the voltammograms (charge capacitance), it was plotted vs. the polymerization charge density (**Fig. 70C**). A linear relationship was observed, which confirms the continuous growth of PANI on the surface of the SiC nanocrystals. Notably,

the overall electroactivity of the electrodeposited nanocomposite samples was much better, compared to their photopolymerized counterparts (**Fig. 68**).

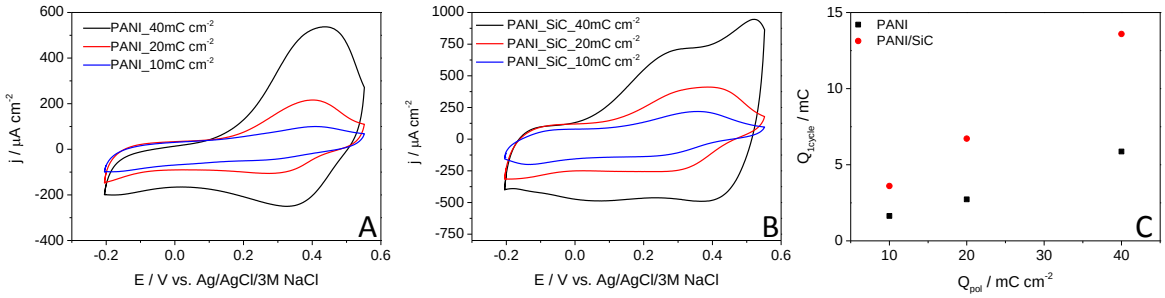

Fig. 70: (A) Comparison of CVs, recorded for PANI (A) and for PANI/SiC (B) electrodes in N_2-saturated 0.1 M Na_2SO_4. m_{SiC} = 0.4 mg cm^{-2}, Q_{pol} = 10, 20, 40 mC cm^{-2}, υ = 50 mV s^{-1} (C) Charge capacitance vs. polymerization charge density plot, derived from (A) and (B).

Raman spectroscopy was employed to confirm the formation of the PANI/SiC nanohybrids (**Fig. 71**). Three intensive bands appeared on the spectrum of SiC; centered at 790 cm^{-1}, 1334 cm^{-1}, and 1595 cm^{-1}. The first one corresponds to the lattice vibration of SiC, specifically to the zone-center transverse optical (TO) phonons of 3C–SiC [183]. The latter two can be assigned to vibrational modes of isolated carbon arrangements [183,184], indicating the presence of carbon traces in the sample. All characteristic bands appeared on the spectrum of the PANI/SiC nanocomposite layer, confirming the formation of PANI on the surface of SiC (**Table 3**).

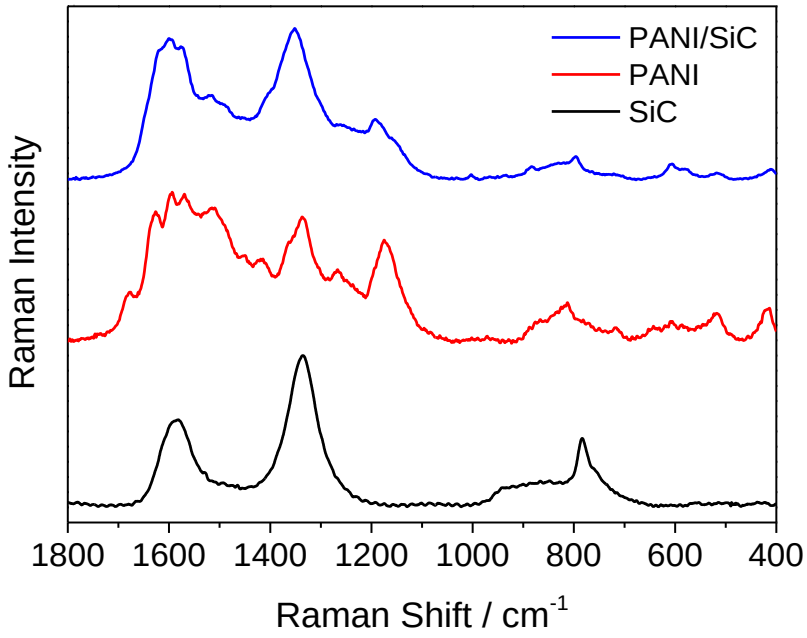

Fig. 71: Raman spectra of SiC (black line), PANI (red line), and PANI/SiC (blue line) samples (m_{SiC} = 0.4 mg cm^{-2}, Q_{pol} = 20 mC cm^{-2}).

The morphological characteristics of SiC and the PANI/SiC nanocomposites were explored by both SEM and TEM. SiC appeared on the SEM images in the form of small, angular, individual nanoparticles (**Fig. 72A**). The particle size is quite diverse, but the majority of the nanoparticles are in the ≈ 50 nm-range (see also **Fig. 65** for the size distribution histogram, derived from the TEM measurements). Contrastingly, in the case of the nanocomposite sample (**Fig. 72B**) a more coherent structure, along with more rounded nanoparticles can be identified, which were glued together by the polymer.

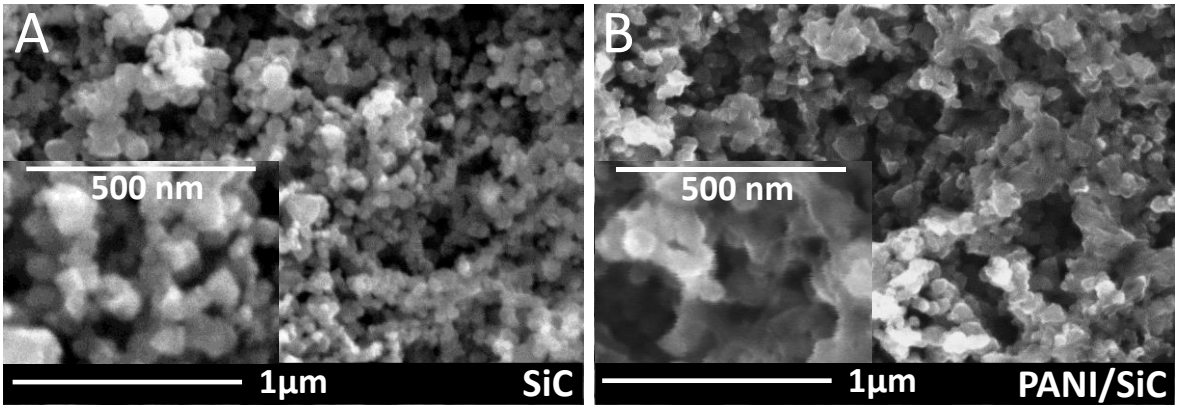

Fig. 72: SEM images of (A) a SiC-coated GC electrode (m_{SiC} = 0.4 mg cm^{-2}) and (B) a PANI/SiC-coated GC electrode (m_{SiC} = 0.4 mg cm^{-2}, Q_{pol} = 40 mC cm^{-2}).

The most prominent difference between the TEM images (**Fig. 73**) of the pristine nanoparticles and the nanocomposite sample is that in the latter case, a PANI layer covers the surface of the SiC nanocrystals (black arrows in **Fig. 73B**). Based on the TEM images, approximately a 2 − 10 nm polymer layer thickness can be estimated. Additionally, a very thin amorphous layer was seen on the images captured for the pristine SiC nanoparticles, corresponding to the ultrathin carbon layer (also identified by Raman spectroscopy). This film however, is much thinner in this case, compared to the PANI film in the core-shell nanocomposites.

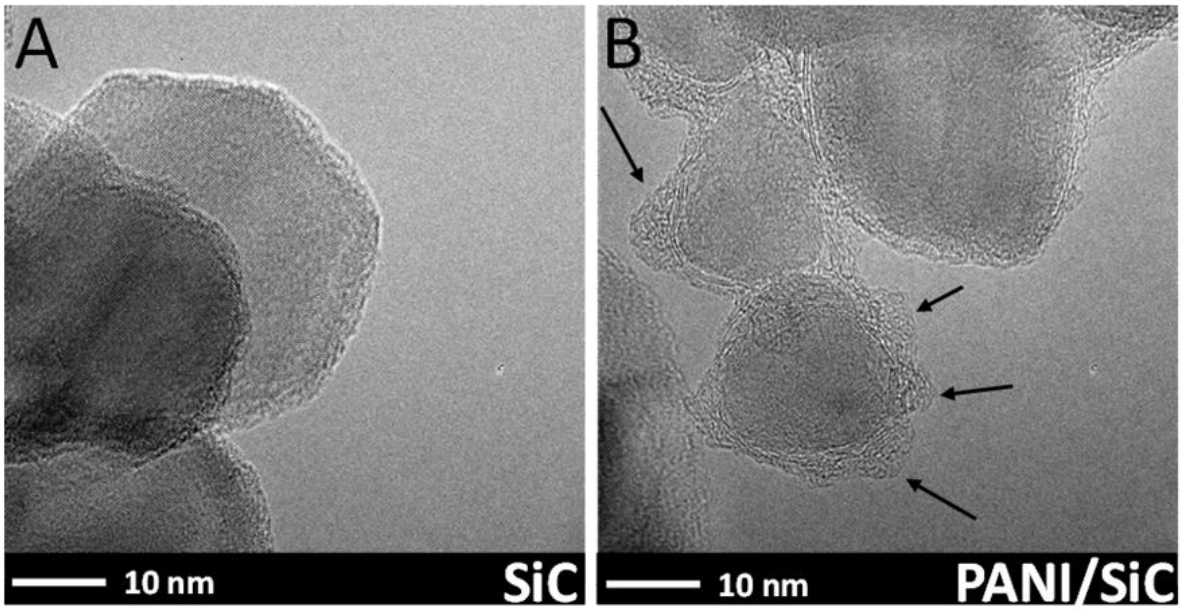

Fig. 73: TEM images of (A) SiC nanoparticles and (B) a PANI-coated SiC nanoparticles (Q_{pol} = 40 mC cm^{-2}). The black arrows indicate the presence of PANI on the surface of the SiC nanoparticles.

5.4.2 Photoelectrochemical behavior

Given the fact that PEC properties highly depend on the morphology and the composition of the photoelectrodes, the role of two parameters were investigated during PEC experiments: i) the effect of the different atmospheres (N_2 and CO_2), and ii) the effect of the PANI/SiC ratio. Comparison of the two photoelectrodes, having the same amount of PANI is presented in **Fig. 74A**, along with the bare SiC. The shape of the voltammograms are similar, but almost two-times higher photocurrents were recorded for the PANI/SiC nanocomposites compared to the bare PANI. Photovoltammograms, recorded for the bare SiC and for the PANI/SiC nanocomposites with various PANI/SiC ratios in CO_2 atmosphere, are presented in **Fig. 74B** (results, measured in N_2 atmosphere for both the pristine polymer and for the nanocomposite samples are presented in **Fig. 75**). Notably, enhanced photocurrents were reached for all nanocomposite photoelectrodes, compared to both pristine components (i.e., SiC and PANI). In addition, photocurrents gradually increased with the amount of PANI, but without a noticeable rise in the value of the dark currents.

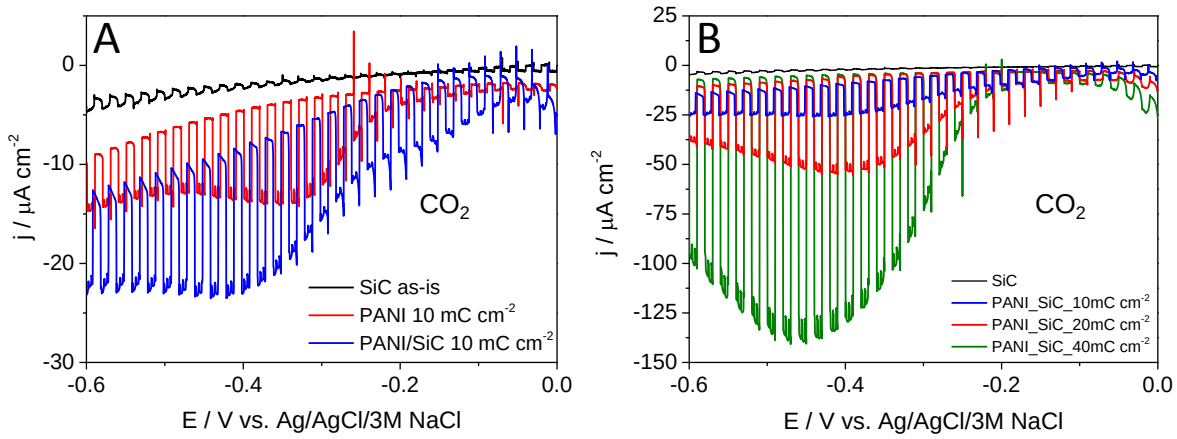

Fig. 74: (A) Comparison of the PEC behavior of PANI and PANI/SiC photoelectrodes in CO_2-saturated 0.1 M $NaHCO_3$ solution. Q_{pol} = 10 mC cm^{-2}. (B) Comparison of the photovoltammograms recorded for PANI/SiC layers with different PANI/SiC ratio in CO_2-saturated 0.1 M $NaHCO_3$ solution. A 300 W Hg-Xe lamp was applied as a light source. The sweep rate was kept at 0.5 mV s^{-1}, while the applied chopping frequency was 0.05 Hz.

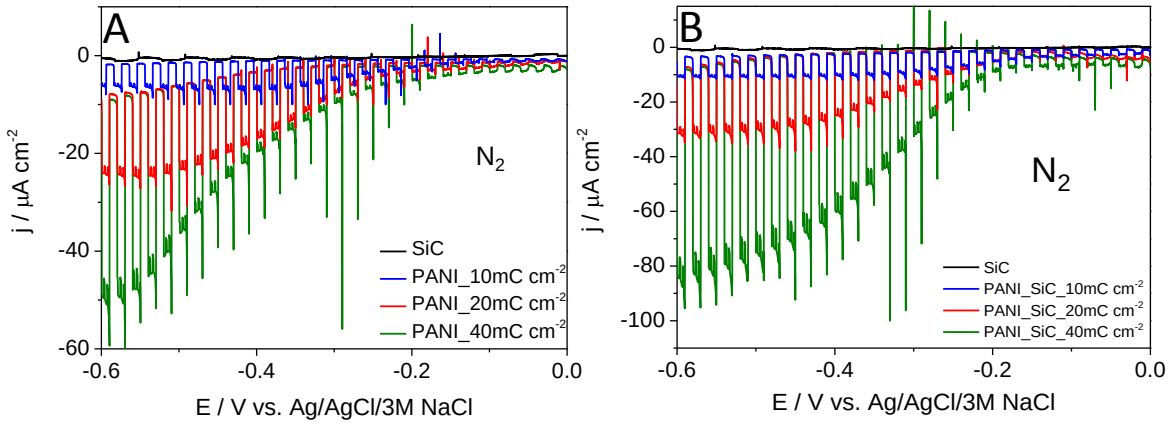

Fig. 75: Comparison of the photovoltammograms, recorded for (A) PANI layers with different thicknesses in N_2-saturated 0.1 M Na_2SO_4 solution, and (B) for PANI/SiC layers with different thicknesses in N_2-saturated 0.1 M Na_2SO_4 solution. A 300 W Hg-Xe lamp was applied as a light source. The sweep rate was kept at 0.5 mV s^{-1}, while the applied chopping frequency was 0.05 Hz.

To quantify the experienced differences, the maximum photocurrent values were determined and plotted versus the polymerization charge (**Fig. 76A, B**). Gradually increasing maximum photocurrents were registered with the higher PANI amount, in both N_2 and CO_2 atmospheres. Additionally, the maximum photocurrents, harvested for the PANI/SiC photoelectrodes are always higher than the ones, registered from the bare PANI. To see, whether these higher photocurrents could be attributed to the higher selectivity toward the PEC reduction of CO_2, the photocurrents, registered in CO_2 atmosphere were

normalized with the ones, obtained in the N_2-saturated electrolyte. According to **Fig. 76C**, solely judging from the currents, there was no increase in the selectivity for the PANI/SiC nanocomposites compared to the bare PANI layers. This also means that the PEC reduction of CO_2 predominantly occurs only on the surface of the PANI layer, but also facilitated by the photoelectrons coming from SiC.

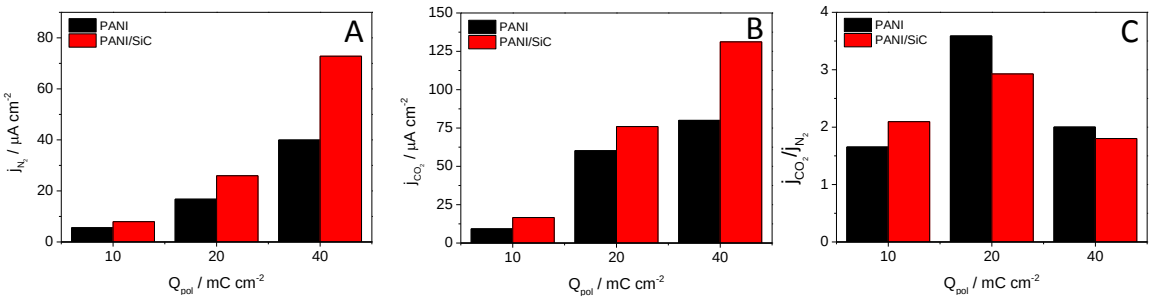

Fig. 76: Maximum photocurrents plotted vs. polymerization charge density, for both PANI and PANI/SiC layers, measured in (A) N_2-saturated 0.1 M Na_2SO_4 and in (B) CO_2-saturated 0.1 M $NaHCO_3$ solutions. (C) Photocurrent ratios registered in CO_2 atmosphere were normalized with the ones, obtained in the N_2-saturated electrolyte for both PANI and PANI/SiC layers.

Photoaction spectra, recorded for PANI and for PANI/SiC nanohybrid photoelectrodes in CO_2 atmosphere (**Fig. 77**) have a similar overall pattern (IPCE values and the wavelength range), to what we observed for PANI earlier (see **Fig. 28A**). The characteristics of the spectrum, measured for PANI/SiC differs from the one of the bare PANI in two aspects: the IPCE percentages are slightly lower in the 300 – 330 nm wavelength range and the wavelength range, where the PANI/SiC nanocomposite is photoactive, broadened.

The bandgap can be calculated by fitting to the linear cutoff region of the spectra and extrapolating to the wavelength axis. The estimated bandgap was 3.1 eV for PANI and 2.9 eV for the nanocomposite sample. The reason behind this improvement lies in the smaller bandgap of the cubic polytype of SiC, which is around 2.4 eV, determined by diffuse reflectance UV-vis spectroscopy. This observation proves that the higher photocurrents are not only rooted in geometrical effects (higher specific surface area due to the carbide nanoparticles), but also to the lower bandgap (the nanocomposite samples can harness a higher portion of the illuminating light compared to the pristine PANI).

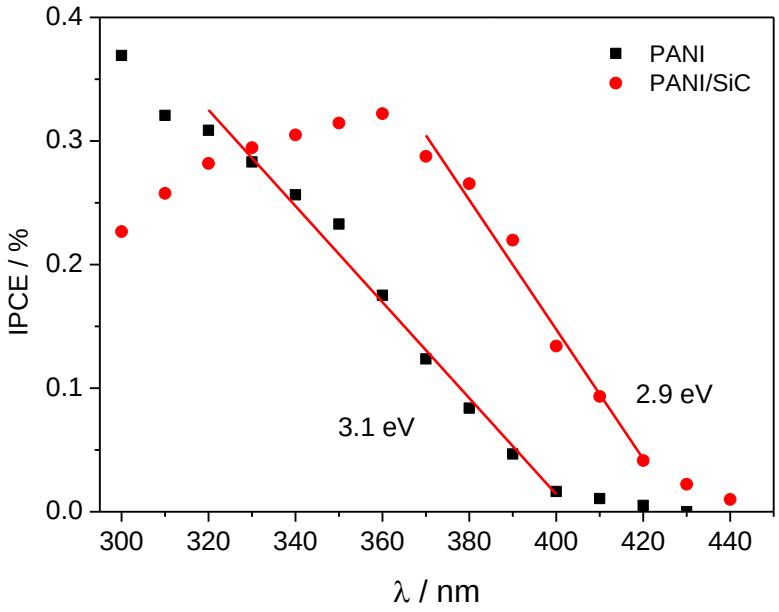

Fig. 77: Photoaction spectra recorded for the PANI and PANI/SiC nanocomposite samples in 0.1 M $NaHCO_3$ saturated with CO_2, at E = −0.4 V potential. Q_{pol} = 40 mC cm^{-2}, $\Delta\lambda$ = 10 nm.

5.4.3 Electrochemical impedance spectroscopy

The effect of the composition on the electric properties was further studied by EIS. The potential was kept at E = −0.4 V to make sure that PANI was fully reduced during the measurements. **Fig. 78A** shows the Nyquist plots, collected for the bare PANI, and SiC layer and for nanocomposites with different amount of PANI (10 mC cm^{-2} and 100 mC cm^{-2} polymerization charge density).

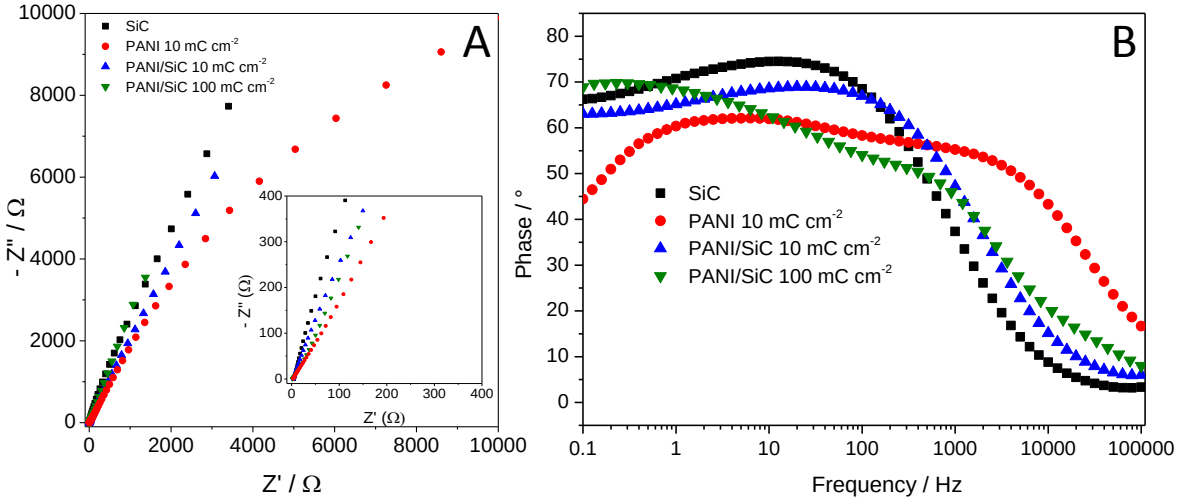

Fig. 78: (A) Nyquist plots recorded for SiC (m_{SiC} = 0.4 mg cm^{-2}), PANI and PANI/SiC composites with varying PANI content, and (B) Bode-plots recorded for the same systems in 1 M Na_2SO_4 solution saturated with Ar at E = −0.4 V potential, in the 0.1 Hz-100 kHz frequency range.

The Nyquist plot recorded for SiC is a vertical line, with an inclination close to 90°, suggesting a capacitive behavior without diffusion limitations [190]. The one, registered for the thin PANI film, consists of a semicircle with a very small diameter (barely visible even in the inset of **Fig. 78A**) in the high-frequency range, and a linear part with an inclination of 45° in the lower-frequency range, which corresponds to a diffusion-limited charge transfer process [190–192]. The shape of the ones, registered for the two nanocomposite electrodes, is similar to the one, collected for SiC. These trends were also supported by the Bode plots (**Fig. 78B**). When only a thin layer of PANI was electrodeposited on the SiC surface, the registered curve is almost identical to the one, measured for SiC. Contrastingly, at high PANI amounts (100 mC cm^{-2} polymerization charge density), the frequency-dependent behavior resembled to the one experienced in the case of the PANI.

To glean quantitative information from these results, an equivalent circuit was fitted to the experimental data (the equivalent circuit is presented in **Fig. 17** and one example to the accuracy of the fit is presented in **Fig. 79**).

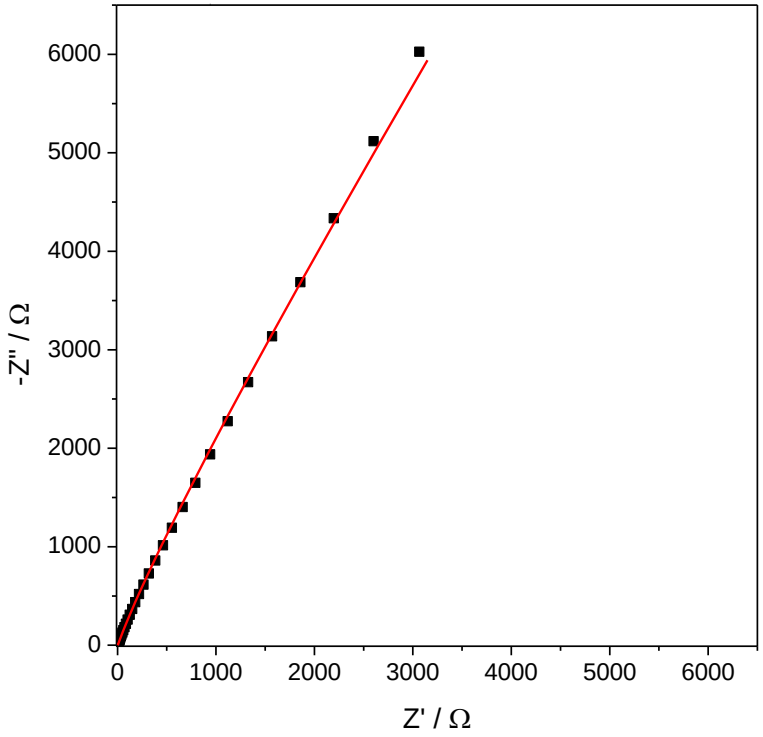

Fig. 79: Accuracy of the fit, using the equivalent circuit presented in **Fig. 17**, demonstrated on the data, recorded for a PANI/SiC layer in 0.1 M Na_2SO_4 solution saturated with Ar, at E = −0.4 V potential, in the 0.1 Hz-100 kHz frequency range. Q_{pol} = 10 mC cm^{-2}, m_{SiC} = 0.4 mg cm^{-2}.

The charge transfer resistance (R_{ct}) values were very small (between 1 – 10 Ω), and almost identical for SiC and the two nanocomposite samples. A bit higher value was determined for PANI (80 Ω), which reveals a good electric contact between the PANI and SiC. In other words, PANI have not ruined the conductivity, and this conclusion stands even for the nanocomposite, containing the highest amount of PANI. The double-layer capacitance values gradually decreased with the increasing amount of PANI, however remained higher, than the one, obtained for the bare PANI layer. This behavior can be explained by the decrease in the accessible surface area (compared to the pristine SiC), experienced in the case of all nanocomposite samples (also seen on the SEM images in **Fig. 72**).

5.4.4 Long-term photoelectrolysis

To explore the stability of the synthesized photoelectrodes, long-term chronoamperometry measurements were performed. In the case of the PANI layers, a photocurrent transient evolved after turning on the illumination, but the evolved maximum photocurrent immediately started to decrease to reach a steady-state value after 30 minutes (10 – 15 µA, **Fig. 80A**). A similar transient behavior was seen for the PANI/SiC nanocomposite photoelectrodes; however, the decrease of the photocurrent was somewhat slower, and its steady-state value was around 30-40% higher compared to the pristine polymer.

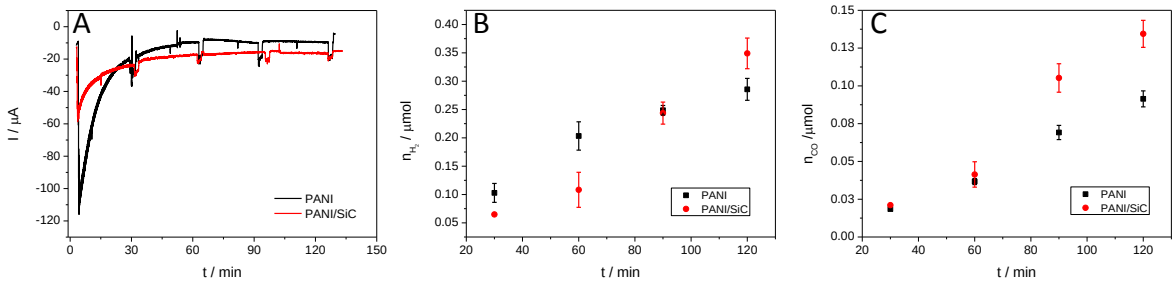

Fig. 80: (A) Long-term chronoamperometry data registered for PANI and PANI/SiC layers, at E = −0.4 V potential (vs. Ag/AgCl/3M NaCl). Error bars were calculated from four individual photoelectrolysis experiments. Q_{pol} = 40 mC cm^{-2}, m_{SiC} = 0.4 mg cm^{-2}. A 300 W Hg-Xe lamp was used as a light source. Formation of (B) H_2 and (C) CO during the photoelectrolysis, presented in (A).

To validate that the experienced higher photocurrents belong to the PEC reduction of CO_2, aliquots were taken in every 30 minutes, from both the gas-, and liquid phases. The gas phase contained H_2 and CO as products, and their amount gradually increased during

the measurement (**Fig. 80B** and **C**). There was almost no difference in the amount of the evolved H_2, and this statement holds for the FE values, calculated for both systems (20%). Contrastingly, the concentration of CO was higher in the samples taken in the case of the PANI/SiC photoelectrodes, which difference has been also reflected in the FE values (the FE increased from 13% to 19%). In the case of the liquid samples, methanol and ethanol were detected by both NMR spectroscopy and GC-MS analysis. We found however, the exact quantitative measurement of these products very challenging. Note that if all the charge passed through during the photoelectrolysis (except subtracting that responsible for the formation of the gas phase products) had corresponded to the formation of ethanol and methanol products, their concentrations would only in the 2 − 4 μM regime at the end of the photoelectrolysis (2h).

6. SUMMARY

The first step of my doctoral work was to study the photoelectrochemical behavior of various conducting polymers. Both PANI and PEDOT showed remarkable performance in PEC fuel generation, however two major drawbacks were identified. First, the poor transport of the photogenerated charge carriers and second, the poor photostability of these electrode materials. In the second phase of my work we tried to mitigate these problems via two different approaches. First, CP/nanocarbon nanocomposites were synthesized, and the effect of the nanocarbons on the PEC properties was investigated. Secondly, the possibility of depositing PANI on the surface of an inorganic SC (SiC) was studied by photocatalytic-, or electrochemical deposition; along with the effect of the polymer on the PEC properties.

The most important results of my doctoral work can be summarized in the following points:

1. According to the measured cathodic photocurrents and to the positive photopotential, all the studied CPs behaved as p-type semiconductors. Photocurrents were originating from the reduction of either H^+ ions or CO_2 at the CP/electrolyte interface. In the case of PANI, a two-fold increase was seen in the photocurrents in the plateau region in the presence of CO_2 compared to the measurements, carried out in N_2-saturated electrolytes. Furthermore, the observed onset potential was +0.1 V (vs. Ag/AgCl/ 3M NaCl), which was 500-700 mV less negative compared to the thermodynamic potential of most of the CO_2 reduction processes. The recorded photoaction spectra perfectly corresponded to the UV-vis spectrum of PANI, as well as the determined bandgaps (2.8 eV in both cases).

2. A fast decrease in the measured photocurrents was observed during the long-term photoelectrolysis experiments in both the case of PANI. The stationary photocurrents were two times higher in the CO_2-saturated case. H_2 was the only detected product in the gas phase in both cases, while methanol and ethanol were detected in the liquid phase only in the CO_2-saturated samples. The experienced decrease in the photocurrents was correlated to the charge carrier recombination-

induced local heating, which resulted in the melting of the PANI film, thus in a decreased electrochemically active surface area.

3. Three essential criteria were identified, which a CP must simultaneously meet to successfully reduce CO_2: i) E_{CB} has to be negative enough for the photogenerated electrons to reduce CO_2, ii) E_{VB} has to be positive enough, to make the CP behave as an SC at the potential where the PEC experiment is performed, and iii) the polymer has to bear with good CO_2-adsorption capacity. (i.e., it has to contain N−H groups, on which chemisorption of CO_2 occurs).

4. The effect of CNT and graphene was investigated on the PEC behavior of PEDOT and PANI. The polymer was successfully electrodeposited on the surface of both spray-coated nanocarbons, which allowed the precise control of the amount of CP present on the electrode surface. The effect of the CP/nanocarbon ratio and the amount of the spray-coated CNT and graphene on the measured photocurrent values was explored. A maximum of four times higher photocurrents were harvested in the case of the PEDOT/CNT system, compared to the pristine PEDOT, while this value was two and a half in the case of the PEDOT/graphene photoelectrodes. Similar observations were made in the case of PANI, however the enhancement was not as striking as in the PEDOT case (two and a half times higher photocurrents were detected for PANI/CNT-, and 1.5 times higher for the PANI/graphene electrodes). According to the EIS measurements, both nanocarbons significantly enhanced the conductivity of the nanocomposites compared to the bare CP layers. These interconnected CNT and graphene networks facilitated the photogenerated charge carrier transport toward both to the surface of the glassy carbon electrode and to the electrode/electrolyte interface resulting in depressed charge carrier recombination, and thus higher harvested photocurrents.

5. The characteristics of the photoaction spectra were identical, while the order of the maximum incident photon to current conversion efficiencies was in line with the photovoltammetry data (highest values were obtained for the CNT-containing layers). These observations suggest, that the light absorption properties were not

affected by the presence of the nanocarbons. An E_{BG} of 1.7 eV (PEDOT-containing systems), and 2.8 eV (PANI containing systems) were estimated. Hydrogen gas was the only detectable product in the gas phase for all PEDOT-containing systems, which evolved with a Faradaic efficiency close to 100%.

6. PANI layers were deposited on the surface of SiC by photocatalytic deposition. The thickness of the polymer was varied between 1.0 − 2.5 nm, simply by varying the irradiation time. This increasing PANI content was also corroborated by TGA data, which additionally confirmed that there is no bulk PANI in the hybrid samples. As gleaned from vibrational spectroscopic and electrochemical studies, it was crucial to filter out the irradiation below 300 nm during the synthesis. While polymer formation was evidenced even when the full UV-vis output of the lamp was utilized, the formed polymer was of low quality, both in terms of structure and electroactivity. This effect is most related to the formation of insulating polymer upon direct photopolymerization (i.e., not by the photogenerated holes in SiC), as well as to the degradation caused by the high energy irradiation. In contrast, such problems did not occur when the hard UV component was filtered out during the synthesis. The low electroactivity of the nanocomposites suggested that the contact between the nanocomposite and the substrate electrode was rather poor.

7. PANI was successfully electrodeposited on the surface of SiC nanoparticles by potentiodynamic cycling, allowing the precise control on the deposited amount of polymer. PANI had a clear effect on the PEC behavior: approximately two times higher photocurrents were detected for the best nanocomposite sample compared to its pristine PANI counterpart. On the other hand, the selectivity towards the PEC reduction of CO_2 has remained unchanged, confirming that the surface chemistry of PANI is dictating the process in both cases. According to the IPCE data, the nanocomposite samples had a 0.2 eV lower bandgap, compared to the bare PANI. This beneficial change in the optical properties can be explained by the smaller bandgap of 3C−SiC (2.4 eV) underneath the polymer coating.

8. Three factors were identified which resulted in enhanced PEC activity in the case of the PANI/SiC samples: i) geometric effects, coming from the higher specific surface area of the PANI/SiC layers, ii) photogenerated charge carriers coming from the SiC nanoparticles (smaller bandgap), iii) catalytic effect of PANI, facilitating e^- transfer from SiC to the substrates. The stability of the photoelectrodes was tested by long-term chronoamperometry. The decrease in the value of the photocurrent was slower in the case of the PANI/SiC system, however, still substantial. H_2 and CO were detected as PEC reduction products in the gas phase, while methanol and ethanol were found in the liquid phase in both cases.

7. ÖSSZEFOGLALÁS

Doktori munkám során első lépésben polianilin és poli(3,4-etiléndioxitiofén) vezető polimer fotokatódok fotoelektrokémiai viselkedését vizsgáltuk. Eredményeink azt mutatták, hogy ugyan mindkét anyag alkalmas tüzelőanyagok előállítására fotoelektrokatalitikus úton, ám két, komoly problémát is azonosítottunk, nevezetesen: i) a polimerekben a töltéstranszport gátolt a rossz vezetésnek köszönhetően, illetve ii) a polimerek gyenge fotostabilitással rendelkeztek. Ezen problémákat két különböző módon próbáltuk meg kiküszöbölni. Először vizsgáltuk a vezető polimernek egy jól vezető szén nanomátrixra történő leválasztásának hatását a fotoelektrokémiai tulajdonságokra. Munkám során következő lépésben annak lehetőségét tanulmányoztuk, hogy miként lehet vezető polimereket leválasztani szervetlen félvezető felületre fotokatalitikus-, illetve elektrokémiai úton, továbbá vizsgálni kívántuk az előállított nanokompozitok fotoelektrokémiai sajátságait.

Doktori munkám legfontosabb eredményei a következő pontokban foglalhatók össze:

1. A vizsgált polimerek mind p-típusú félvezetőként viselkedtek, mely a pozitív fotopotenciálban, illetve a katódos fotoáramokban mutatkozott meg. A mért fotoáram a H^+-ionok, illetve a CO_2 elektród/elektrolit határfelületen történő redukciójából eredt. A PANI esetében, CO_2 jelenlétében mintegy kétszeres növekményt tapasztaltunk a stacionárius fotoáram nagyságában, a N_2 atmoszférában mértekhez képest. Továbbá, az onset potenciál értéke +0.1 V-nak (vs. Ag/AgCl/ 3M NaCl) adódott, mely 500-700 mV-tal pozitívabb a CO_2 redukciós folyamatok többségének termodinamikai potenciájához képest. A felvett IPCE görbék tökéletesen átfedtek a polimer UV-látható spektrumával, továbbá a kétféle spektrumból meghatározott tiltott sáv szélesség értékek is azonosnak adódtak (2.8 eV).

2. A PANI elektródokon végzett hosszú távú fotoelektrolízis alatt a kezdeti fotoáram gyorsan lecsökkent a stacionárius értékére. A mért egyensúlyi értékek mintegy kétszer nagyobbak voltak a CO_2-dal telített oldatokban végzett mérések esetén. A gáz fázisban mind N_2-, mind pedig CO_2 atmoszférában végzett mérések esetén H_2 volt detektálható, míg a folyadék fázisban metanol és etanol jelenlétét mutattuk ki,

de csak a CO_2-dal telített oldatokból vett minták esetén. A fotoáram gyors csökkenését a felületi töltéshordozó rekombináció eredményeképp fellépő lokális hőeffektusoknak tulajdonítottuk, melyek hatására a polimer réteg megolvadt, így az aktív felület nagymértékű csökkenését eredményezte.

3. A mérések alapján három alapvető követelményt definiáltunk, amelyeket egy vezető polimer fotoelekródnak teljesíteni kell, hogy azon a CO_2 fotoelektrokémiai redukciója sikerrel megvalósítható legyen: i) A E_{CB}-nek megfelelően negatívnak kell lenni, hogy a fotogenerált elektronok képesek legyenek redukálni a CO_2-ot, ii) E_{VB}-nek megfelelően pozitívnak kell lennie ahhoz, hogy a vezető polimer félvezetőként viselkedjen a fotoelektrokatalitikus folyamat potenciáltartományában, illetve iii) a polimernek jó CO_2-adszorpciós kapacitással kell rendelkeznie, melyet a struktúrában jelenlévő N−H csoportok biztosítanak, amelyeken a CO_2 kemiszorpciója megvalósulhat.

4. Következő lépésben a szén nanocső-, illetve grafén hatását vizsgáltuk a PANI-, illetve PEDOT fotoelektrokémiai sajátságaira. A nanoszenek felületére elektrokémiai polimerizációval választottuk le a vezető polimer rétegeket, mely segítségével egyszerűen, mégis precízen kontrollálható volt a leválasztott polimer mennyisége. Mind a CP/nanoszén arány, mind pedig a nanoszén mennyiségének hatását vizsgáltuk a kinyerhető fotoáram értékekre. A sima PEDOThoz képest maximálisan mintegy négyszer nagyobb fotoáramokat mértünk a PEDOT/CNT rendszer esetében, míg két és félszereset a PEDOT/grafén elektródok esetén. Hasonló megfigyeléseket tettünk a PANI/nanoszén rendszerek esetében is, de a növekmény a sima polimerhez képest kisebb volt (két és félszeres a PANI/CNT-, míg másfélszeres a PANI/grafén fotoelektródok esetén). Az EIS mérések alapján arra következtethetünk, hogy mind a szén nanocsövek, mindkét nanoszén nagyban növelte a nanokompozitok vezetését a sima polimerekhez képest, azaz nagyban javították a fotogenerált töltéshordozók transzportját, mind a GC hordozó elektródfelület-, mind pedig az elektród/elektrolit határfelület felé. Ez visszaszorította a töltéshordozó rekombinációt, mely nagyobb mért fotoáram értékeket eredményezett.

5. A felvett IPCE görbék karakterisztikája minden esetben azonos volt, míg az IPCE értékek nagysága a fotovoltammetriás méréseknél tapasztaltakat tükrözte (a legnagyobb értékeket a CNT-tartalmú rendszerek esetén kaptuk). Ezen megfigyelések alapján arra lehet következtetni, hogy a nanoszén mátrixok nem befolyásolták a fényelnyelési sajátságokat. A spektrumokból 1.7 eV-os (PEDOT-tartalmú rendszerek), illetve 2.8 eV-os (PANI-tartalmú rendszerek) tiltott sáv szélesség értékeket határoztunk meg. A PEDOT-tartalmú fotoelektródok esetén egyetlen kimutatható termék H_2 volt a gáz fázisban, mely közel 100%-os Faraday-hatékonysággal keletkezett.

6. Sikerrel választottunk le PANI vékonyrétegeket SiC nanorészecskék felületére fotokatalitikus polimerizációval. A polimer réteg vastagsága 1.0 − 2.5 nm között egyszerűen variálható volt a megvilágítás idejének változtatásával. Mint az kitűnt az infravörös-, Raman-spektroszkópiás, illetve ciklikus voltammetriás mérésekből, kulcsfontosságú, hogy a polimerizáció során a 300 nm alatti hullámhosszúságú fényt kiszűrjük. A polimer leválása a nanorészecskék felületére egyértelműen bizonyítható volt abban az esetben is, amikor a megvilágító fényforrás spektrumából ezen kemény UV-komponensek nem voltak kiszűrve, azonban a leválasztott polimer réteg mind a szerkezet-, mind pedig az elektroaktivitás szempontjából rossz minőségű volt. Ezt a hatást a direkt fotopolimerizáció (azaz nem a SiC-ben keletkező fotogenerált lyukak által történő) során keletkező szigetelő bevonatnak, illetve a nagy energiájú sugárzás miatt fellépő fotodegradációnak tulajdonítottuk. Ezzel szemben, amikor a kemény UV-komponense a megvilágító fényforrásnak kiszűrésre került a szintézis során, ilyen effektusokat nem figyeltünk meg. Azonban az ebben az esetben is tapasztalt rossz elektroaktivitásból a nanokompozit és a hordozó elektród felülete közötti rossz kontaktra következtettünk.

7. A spray-coating technikával felvitt SiC felületére PANI vékonyrétegeket választottunk le elektrodepozícióval, mely segítségével egyszerűen, mégis precízen kontrollálható volt a leválasztott polimer mennyisége. A polimer egyértelműen jelentős hatással bírt a fotoelektrokémiai sajátságokra: mintegy kétszer nagyobb

fotoáramokat detektáltunk a sima polimerhez képest az optimális összetételű nanokompozit minta esetén. A szelektivitás a CO_2 fotoelektrokémiai redukciója irányába azonban nem nőtt, mely arra enged következtetni, hogy mindkét esetben a PANI felületén zajlik a folyamat. Az IPCE adatok alapján a nanokompozit minták kb. 0.2 eV-tal kisebb tiltott sáv szélességgel bírtak az ezen körülmények között szintetizált és vizsgált PANI rétegekhez képest. Ezt az előnyös hatást a polimer réteg alatt lévő, jelentősen kisebb tiltott sáv szélességgel rendelkező (E_{BG} = 2.4 eV) köbös kristályrácsú 3C−SiC-nak tulajdonítottuk.

8. A PANI/SiC nanokompozitok esetében tapasztalt megnövekedett fotoelektrokémiai aktivitás a következőképp magyarázható: i) geometriai effektusok, a PANI/SiC rétegek megnövekedett specifikus felülete miatt, ii) többlet fotogenerált töltéshordozók a kisebb E_{BG}-ű SiC-tól, illetve iii) a PANI katalitikus hatása, mely nagyban elősegíti a töltéstranszfert a SiC-tól a szubsztrátum molekulákra. A fotoelektródok stabilitását hosszútávú kronoamperometriás mérésekkel vizsgáltuk, melyek során a fotoáram lassabb, azonban így is jelentős lecsengését tapasztaltuk a PANI/SiC rendszer esetén a sima polimerhez képest. A gázfázisban H_2-t és CO-t detektáltunk, míg a folyadékfázisban metanol és etanol jelenlétét mutattuk ki.

8. REFERENCES

[1] N. Lewis, D. Nocera, Powering the planet: Chemical challenges in solar energy utilization, Proc. Natl. Acad. Sci. 104 (2006) 15729–15735.

[2] A.M. Appel, J.E. Bercaw, A.B. Bocarsly, H. Dobbek, D.L. Dubois, M. Dupuis, J.G. Ferry, E. Fujita, R. Hille, P.J. A Kenis, C. A Kerfeld, R.H. Morris, C.H.F. Peden, A.R. Portis, S.W. Ragsdale, T.B. Rauchfuss, J.N.H. Reek, L.C. Seefeldt, R.K. Thauer, G.L. Waldrop, Frontiers, opportunities, and challenges in biochemical and chemical catalysis of CO_2 fixation., Chem. Rev. 113 (2013) 6621–6658.

[3] G.W. Crabtree, N.S. Lewis, Solar energy conversion, Phys. Today. 60 (2007) 37–42.

[4] https://www.iea.org/publications/freepublications/publication/KeyWorld2017.pdf. last visited: 2018.02.22.

[5] Y. Tachibana, L. Vayssieres, J.R. Durrant, Artificial photosynthesis for solar water-splitting, Nat. Photonics 6 (2012) 511–518.

[6] J.-W. Jang, S. Cho, G. Magesh, Y.J. Jang, J.Y. Kim, W.Y. Kim, J.K. Seo, S. Kim, K.-H. Lee, J.S. Lee, Aqueous-solution route to zinc telluride films for application to CO_2 reduction, Angew. Chemie Int. Ed. 53 (2014) 5852–5857.

[7] J. Li, N. Wu, Semiconductor-based photocatalysts and photoelectrochemical cells for solar fuel generation: a review, Catal. Sci. Technol. 5 (2015) 1360–1384.

[8] J.L. White, M.F. Baruch, J.E. Pander, Y. Hu, I.C. Fortmeyer, J.E. Park, T. Zhang, K. Liao, J. Gu, Y. Yan, T.W. Shaw, E. Abelev, A.B. Bocarsly, Light-driven heterogeneous reduction of carbon dioxide: photocatalysts and photoelectrodes, Chem. Rev. 115 (2015) 12888–12935.

[9] B. Kumar, M. Llorente, J. Froehlich, T. Dang, A. Sathrum, C.P. Kubiak, Photochemical and photoelectrochemical reduction of CO_2, Annu. Rev. Phys. Chem. 63 (2012) 541–569.

[10] I. Roger, M.A. Shipman, M.D. Symes, Earth-abundant catalysts for electrochemical and photoelectrochemical water splitting, Nat. Rev. Chem. 1 (2017) 3-1-3-13.

[11] C.M. Sánchez-Sánchez, V. Montiel, D. A. Tryk, A. Aldaz, A. Fujishima, Electrochemical approaches to alleviation of the problem of carbon dioxide accumulation, Pure Appl. Chem. 73 (2001) 1917–1927.

[12] H.A. Schwarz, R.W. Dodson, Reduction potentials of CO_2- and the alcohol radicals, J. Phys. Chem. 93 (1989) 409–414.

[13] P.S. Surdhar, S.P. Mezyk, D.A. Armstrong, Reduction potential of the carboxyl radical anion in aqueous solutions, J. Phys. Chem. 93 (1989) 3360–3363.

[14] E. Lamy, L. Nadjo, J.M. Saveant, Standard potential and kinetic parameters of the electrochemical reduction of carbon dioxide in dimethylformamide, J. Electroanal. Chem. Interfacial Electrochem. 78 (1977) 403–407.

[15] B. Aurian-Blajeni, M. Halmann, J. Manassen, Electrochemical measurement on the photoelectrochemical reduction of aqueous carbon dioxide on p-gallium phosphide and p-gallium arsenide semiconductor electrodes, Sol. Energy Mater. 8 (1983) 425–440.

[16] M. Jitaru, Electrochemical carbon dioxide reduction - fundamental and applied topics, J. Univ. Chem. Technol. Metall. 42 (2007) 333–344.

[17] K. Rajeshwar, A. Thomas, C. Janáky, Photocatalytic activity of inorganic semiconductor surfaces: myths, hype, and reality, J. Phys. Chem. Lett. 6 (2015) 139–147.

[18] I. Taniguchi, B. Aurian-Blajeni, J.O. Bockris, The reduction of carbon dioxide at illuminated p-type semiconductor electrodes in nonaqueous media, Electrochim. Acta 29 (1984) 923–932.

[19] K. Rajeshwar, Solar energy conversion and environmental remediation using inorganic semiconductor/liquid interfaces: the road traveled and the way forward, J. Phys. Chem. Lett. 2 (2011) 1301–1309.

[20] A. Kormányos, A. Thomas, M.N. Huda, P. Sarker, J.P. Liu, N. Poudyal, C. Janáky, K. Rajeshwar, Solution combustion synthesis, characterization, and photoelectrochemistry of $CuNb_2O_6$ and $ZnNb_2O_6$ nanoparticles, J. Phys. Chem. C 120 (2016) 16024–16034.

[21] E. Kecsenovity, B. Endrődi, P.S. Tóth, Y. Zou, R.A.W. Dryfe, K. Rajeshwar, C. Janáky, Enhanced photoelectrochemical performance of cuprous oxide/graphene nanohybrids, J. Am. Chem. Soc. 139 (2017) 6682–6692.

[22] Y. Yang, S. Ajmal, X. Zheng, L. Zhang, Efficient nanomaterials for harvesting clean fuels from electrochemical and photoelectrochemical CO_2 reduction, Sustain. Energy Fuels. 0 (2018) 1–28.

[23] L.S.Ramsdell, Studies on silicon carbide, Am. Miner. 32 (1945) 64–82.

[24] Y.A. Vodakov, E.N. Mokhov, A.D. Roenkov, D.T. Saidbekov, Effect of crystallographic orientation on the polytype stabilization and transformation of silicon carbide, Phys. Status Solidi. 51 (1979) 209–215.

[25] I. Lauermann, Electrochemical properties of silicon carbide, J. Electrochem. Soc. 144 (1997) 73-80.

[26] H. Zhuang, N. Yang, L. Zhang, R. Fuchs, X. Jiang, Electrochemical properties and applications of nanocrystalline, microcrystalline, and epitaxial cubic silicon carbide films, ACS Appl. Mater. Interfaces 7 (2015) 10886–10895.

[27] C. He, X. Wu, J. Shen, P.K. Chu, High-efficiency electrochemical hydrogen evolution based on surface autocatalytic effect of ultrathin 3C-SiC nanocrystals, Nano Lett. 12 (2012) 1545–1548.

[28] M. Mwania, C. Janáky, K. Rajeshwar, P. Kroll, Fabrication of β-SiC quantum dots by photo-assisted electrochemical corrosion of bulk powders, Electrochem. Commun. 37 (2013) 1–4.

[29] N. Yang, H. Zhuang, R. Hoffmann, W. Smirnov, J. Hees, X. Jiang, C.E. Nebel, Electrochemistry of nanocrystalline 3C silicon carbide films, Chem. - A Eur. J. 18 (2012) 6514–6519.

[30] C.H. Park, B. Cheong, K. Lee, K.J. Chang, Structural and electronic properties of cubic, 2H , 4H , and 6H SiC, Phys. Rev. B. 49 (1994) 4485–4493.

[31] T. Inoue, A. Fujishima, S. Konishi, K. Honda, Photoelectrocatalytic reduction of carbon dioxide in aqueous suspensions of semiconductor powders, Nature 277 (1979) 637–638.

[32] A. Kohler, H. Bassler, The electronic structure of organic semiconductors, in Electron. Process. Org. Semicond., 1st ed., Wiley-VCH, Weinheim, 2015: pp. 1–3.

[33] Y. Wang, X. Wang, M. Antonietti, Polymeric graphitic carbon nitride as a heterogeneous organocatalyst: from photochemistry to multipurpose catalysis to sustainable chemistry, Angew. Chemie Int. Ed. 51 (2012) 68–89.

[34] A. Thomas, A. Fischer, F. Goettmann, M. Antonietti, J.-O. Müller, R. Schlögl, J.M. Carlsson, Graphitic carbon nitride materials: variation of structure and morphology and their use as metal-free catalysts, J. Mater. Chem. 18 (2008) 4893-4908.

[35] J. Lü, C. Perez-Krap, M. Suyetin, N.H. Alsmail, Y. Yan, S. Yang, W. Lewis, E. Bichoutskaia, C.C. Tang, A.J. Blake, R. Cao, M. Schröder, A robust binary supramolecular organic framework (SOF) with high CO_2 adsorption and selectivity, J. Am. Chem. Soc. 136 (2014) 12828–12831.

[36] S. Kampouri, T.N. Nguyen, C. Ireland, B. Valizadeh, F. Ebrahim, G. Capano, D. Ongari, M. Mace, N. Guijarro, K. Sivula, A. Sienkiewicz, L. Forro, B. Smit, K. Stylianou, Photocatalytic hydrogen generation from a visible-light responsive metal-organic framework system: The impact of nickel phosphide nanoparticles, J. Mater. Chem. A (2018) 2476-2481.

[37] T. Sick, A.G. Hufnagel, J. Kampmann, I. Kondofersky, M. Calik, J.M. Rotter, A.M. Evans, M. Döblinger,

S. Herbert, K. Peters, D. Boehm, P. Knochel, D.D. Medina, D. Fattakhova-Rohlfing, T. Bein, Oriented films of conjugated 2D covalent organic frameworks as photocathodes for water splitting, J. Am. Chem. Soc. (2017) 2085-2092.

[38] G. Inzelt, Classification of electrochemically active polymers, in: F. Scholz (Ed.), second ed., Springer Verlag, Berlin, 2012: pp. 7–82.

[39] J.L. Bredas, G.B. Street, Polarons, bipolarons, and solitons in conducting polymers, Acc. Chem. Res. 18 (1985) 309–315.

[40] V. Brandl, R. Holze, Influence of the preparation conditions on the properties of electropolymerised polyaniline, Berichte Der Bunsengesellschaft Für Phys. Chemie. 101 (1997) 251–256.

[41] J.-L. Brédas, D. Beljonne, V. Coropceanu, J. Cornil, Charge-transfer and energy-transfer processes in π-conjugated oligomers and polymers: a molecular picture, Chem. Rev. 104 (2004) 4971–5004.

[42] H. Yang, A.J. Bard, The application of fast scan cyclic voltammetry. Mechanistic study of the initial stage of electropolymerization of aniline in aqueous solutions, J. Electroanal. Chem. 339 (1992) 423–449.

[43] G. Zotti, S. Cattarin, N. Comisso, Cyclic potential sweep electropolymerization of aniline. The role of anions in the polymerization mechanism, J. Electroanal. Chem. 239 (1988) 387–396.

[44] S. Patra, K. Barai, N. Munichandraiah, Scanning electron microscopy studies of PEDOT prepared by various electrochemical routes, Synth. Met. 158 (2008) 430–435.

[45] M. Kaneko, H. Nakamura, Photoresponse of a liquid junction polyaniline film, J. Chem. Soc. Chem. Commun. 104 (1985) 346-347.

[46] M. Kaneko, K. Okuzumi, A. Yamada, Photocurrent generation by a liquid-junction poly(pyrrole) film, J. Electroanal. Chem. Interfacial Electrochem. 183 (1985) 407–410.

[47] P.A. Kilmartin, G.A. Wright, Photoelectrochemistry and spectroscopy of substituted polyanilines, Synth. Met. 104 (1999) 145–156.

[48] P.A. Kilmartin, G.A. Wright, Photoeffects to characterise polypyrrole electrodes and bilayers with polyaniline, Electrochim. Acta 46 (2001) 2787–2794.

[49] D.N. Upadhyay, S. Bharathi, V. Yegnaraman, G.P. Rao, Photoelectrochemical and electrochemical behaviour of gold electrode modified with bilayers of polypyrrole and polyaniline, Sol. Energy Mater. Sol. Cells. 37 (1995) 307–314.

[50] M. Kalaji, L. Nyholm, L.M. Peter, A.J. Rudge, Photoelectrochemical properties of polyaniline films, J. Electroanal. Chem. Interfacial Electrochem. 310 (1991) 113–126.

[51] P.K. Shen, Z.Q. Tian, Photoelectrochemical behavior of polyaniline in the presence of redox couple and electron acceptor, Electrochim. Acta 34 (1989) 1611–1613.

[52] J. Desilvestro, O. Haas, Electrocatalytic behavior of polyaniline in the dark and under illumination, Electrochim. Acta 36 (1991) 361–367.

[53] E.. Geniès, M. Lapkowski, Spectroelectrochemical studies of redox mechanisms in polyaniline films. Evidence of two polaron-bipolaron systems, Synth. Met. 21 (1987) 117–121.

[54] E.M. Geniès, M. Lapkowski, E. Moldculaire, L. De Chimie, D. De Recherche, Influence of light on the electrochemical behaviour of polyaniline films, Synth. Met. 24 (1988) 69–76.

[55] M. Martini, M.-A. De Paoli, Action spectra of EE and SE illuminated polypyrrole-dodecylsulphate films in aqueous solutions, Sol. Energy Mater. Sol. Cells. 60 (2000) 73–83.

[56] F.L.C. Miquelino, M.-A. De Paoli, E.M. Geniès, Photoelectrochemical response in conducting polymer films, Synth. Met. 68 (1994) 91–96.

[57] L. Micaroni, M.-A. De Paoli, Photoelectrochemistry of poly(3-methylthiophene), I: Surface

morphology and thickness effect, Sol. Energy Mater. Sol. Cells 43 (1996) 79–91.

[58] O. Semenikhin, E. Ovsyannikova, M. Ehrenburg, N. Alpatova, V. Kazarinov, Electrochemical and photoelectrochemical behaviour of polythiophenes in non-aqueous solutions, J. Electroanal. Chem. 494 (2000) 1–11.

[59] P. Bornoz, M.S. Prévot, X. Yu, N. Guijarro, K. Sivula, Direct light-driven water oxidation by a ladder-type conjugated polymer photoanode, J. Am. Chem. Soc. 137 (2015) 15338–15341.

[60] P.B. Pati, G. Damas, L. Tian, D.L.A. Fernandes, L. Zhang, I.B. Pehlivan, T. Edvinsson, C.M. Araujo, H. Tian, An experimental and theoretical study of an efficient polymer nano-photocatalyst for hydrogen evolution, Energy Environ. Sci. 10 (2017) 1372–1376.

[61] C. Liu, K. Wang, X. Gong, A.J. Heeger, Low bandgap semiconducting polymers for polymeric photovoltaics, Chem. Soc. Rev. 45 (2016) 4825–4846.

[62] K. Ogura, Mechanistic studies of CO_2 reduction on a mediated electrode with conducting polymer and inorganic conductor films, J. Electrochem. Soc. 145 (1998) 3801-3809.

[63] A. Zhang, W. Zhang, J. Lu, G.G. Wallace, J. Chen, Electrocatalytic reduction of carbon dioxide by cobalt phthalocyanine-incorporated polypyrrole, Electrochem. Solid-State Lett. 12 (2009) E17-E19.

[64] M.R. Liebl, J. Senker, Microporous functionalized triazine-based polyimides with high CO_2 capture capacity, Chem. Mater. 25 (2013) 970–980.

[65] X. Yang, J. Loos, S.C. Veenstra, W.J.H. Verhees, M.M. Wienk, J.M. Kroon, M.A.J. Michels, R.A.J. Janssen, Nanoscale morphology of high-performance polymer solar cells, Nano Lett. 5 (2005) 579–583.

[66] Y. Olivier, D. Niedzialek, V. Lemaur, W. Pisula, K. Müllen, U. Koldemir, J.R. Reynolds, R. Lazzaroni, J. Cornil, D. Beljonne, High-mobility hole and electron transport conjugated polymers: How structure defines function, Adv. Mater. 26 (2014) 2119–2136.

[67] Q. Wei, M. Mukaida, Y. Naitoh, T. Ishida, Morphological change and mobility enhancement in PEDOT:PSS by adding co-solvents, Adv. Mater. 25 (2013) 2831–2836.

[68] P.A. Kilmartin, G.A. Wright, Photoeffects at a polyaniline film electrode, Electrochim. Acta 41 (1996) 1677–1687.

[69] E. Kang, K. Neoh, K. Tan, Polyaniline: A polymer with many interesting intrinsic redox states, Prog. Polym. Sci. 23 (1998) 277–324.

[70] C. Janaky, N.R. de Tacconi, W. Chanmanee, K. Rajeshwar, Electrodeposited polyaniline in a nanoporous WO_3 matrix: An organic/inorganic hybrid exhibiting both p-and n-type photoelectrochemical activity, J. Phys. Chem. C 116 (2012) 4234–4242.

[71] G.F. Samu, K. Pencz, C. Janáky, K. Rajeshwar, On the electrochemical synthesis and charge storage properties of WO_3/polyaniline hybrid nanostructures, J. Solid State Electrochem. 19 (2015) 2741–2751.

[72] X. Li, D. Wang, G. Cheng, Q. Luo, J. An, Y. Wang, Preparation of polyaniline-modified TiO_2 nanoparticles and their photocatalytic activity under visible light illumination, Appl. Catal. B Environ. 81 (2008) 267–273.

[73] X. Wang, Y. Shen, A. Xie, L. Qiu, S. Li, Y. Wang, Novel structure CuI/PANI nanocomposites with bifunctions: Superhydrophobicity and photocatalytic activity, J. Mater. Chem. 21 (2011) 9641-9646.

[74] L. Ge, C. Han, J. Liu, In situ synthesis and enhanced visible light photocatalytic activities of novel PANI–g-C_3N_4 composite photocatalysts, J. Mater. Chem. 22 (2012) 11843-11850.

[75] C.M. Hart, D.M. De Leeuw, M. Matters, P.T. Herwig, C.M.J. Mutsaerts, C.J. Drury, Low-cost all-polymer integrated circuits, Eur. Solid-State Circuits Conf. 108 (1998) 30–34.

[76] E.R. Holland, S.J. Pomfret, P.N. Adams, A.P. Monkman, Conductivity studies of polyaniline doped with

camphorsulfonic acid, J. Phys. Condens. Matter. 8 (1996) 2991–3002.

[77] R. Patil, Y. Harima, K. Yamashita, K. Komaguchi, Y. Itagaki, M. Shiotani, Charge carriers in polyaniline film: A correlation between mobility and in-situ ESR measurements, J. Electroanal. Chem. 518 (2002) 13–19.

[78] C. Belabed, A. Abdi, Z. Benabdelghani, G. Rekhila, A. Etxeberria, M. Trari, Photoelectrochemical properties of doped polyaniline: Application to hydrogen photoproduction, Int. J. Hydrogen Energy. 38 (2013) 6593–6599.

[79] H. Zhang, R. Zong, Y. Zhu, Photocorrosion inhibition and photoactivity enhancement for zinc oxide via hybridization with monolayer polyaniline, J. Phys. Chem. C 113 (2009) 4605–4611.

[80] H. Zhang, Y. Zhu, Significant Visible Photoactivity and antiphotocorrosion performance of CdS photocatalysts after monolayer polyaniline hybridization, J. Phys. Chem. C 114 (2010) 5822–5826.

[81] J. Gu, A. Wuttig, J.W. Krizan, Y. Hu, Z.M. Detweiler, R.J. Cava, A.B. Bocarsly, Mg-doped $CuFeO_2$ photocathodes for photoelectrochemical reduction of carbon dioxide, J. Phys. Chem. C 117 (2013) 12415–12422.

[82] U. Salzner, J.B. Lagowski, P.G. Pickup, R.A. Poirier, Comparison of geometries and electronic structures of polyacetylene, polyborole, polycyclopentadiene, polypyrrole, polyfuran, polysilole, polyphosphole, polythiophene, polyselenophene and polytellurophene, Synth. Met. 96 (1998) 177–189.

[83] R.B. Gupta, Ultraviolet electroluminescence from zinc oxide nanorods/deoxyribonucleic acid hybrid bio light-emitting diode, J. Nanophotonics 5 (2011) 59505-1-59505-6.

[84] B. Aurian-Blajeni, I. Taniguchi, J.O. Bockris, Photoelectrochemical reduction of carbon dioxide using polyaniline-coated silicon, J. Electroanal. Chem. Interfacial Electrochem. 149 (1983) 291–293.

[85] B. Winther-Jensen, O. Winther-Jensen, M. Forsyth, D.R. MacFarlane, High rates of oxygen reduction over a vapor phase-polymerized PEDOT electrode, Science 321 (2008) 671–674.

[86] J. Xia, N. Masaki, M. Lira-Cantu, Y. Kim, K. Jiang, S. Yanagida, Influence of doped anions on poly(3,4-ethylenedioxythiophene) as hole conductors for iodine-free solid-state dye-sensitized solar cells, J. Am. Chem. Soc. 130 (2008) 1258–1263.

[87] Y. Xiao, G. Han, J. Wu, J. Lin, Efficient bifacial perovskite solar cell based on a highly transparent poly(3,4-ethylenedioxythiophene) as the p-type hole-transporting material, J. Power Sources 306 (2016) 171–177.

[88] J. Kim, J.K. Koh, B. Kim, S.H. Ahn, H. Ahn, D.Y. Ryu, J.H. Kim, E. Kim, Enhanced performance of I_2-free solid-state dye-sensitized solar cells with conductive polymer up to 6.8%, Adv. Funct. Mater. 21 (2011) 4633–4639.

[89] A. Guerrero, M. Haro, S. Bellani, M.R. Antognazza, L. Meda, S. Gimenez, J. Bisquert, Organic photoelectrochemical cells with quantitative photocarrier conversion, Energy Environ. Sci. 7 (2014) 3666–3673.

[90] C. Janáky, K. Rajeshwar, The role of (photo)electrochemistry in the rational design of hybrid conducting polymer/semiconductor assemblies: From fundamental concepts to practical applications, Prog. Polym. Sci. 43 (2015) 96–135.

[91] C. Janáky, E. Kecsenovity, K. Rajeshwar, Electrodeposition of inorganic oxide/nanocarbon composites: Opportunities and challenges, ChemElectroChem 3 (2016) 181–192.

[92] A.K. Chauhan, S.K. Gupta, D. Taguchi, T. Manaka, P. Jha, P. Veerender, C. Sridevi, S.P. Koiry, S.C. Gadkari, M. Iwamoto, Enhancement of the carrier mobility of conducting polymers by formation of their graphene composites, RSC Adv. 7 (2017) 11913–11920.

[93] I. V. Lightcap, P. V. Kamat, Fortification of CdSe quantum dots with graphene oxide. Excited state interactions and light energy conversion, J. Am. Chem. Soc. 134 (2012) 7109–7116.

[94] J.G. Radich, A.L. Krenselewski, J. Zhu, P. V Kamat, Is graphene a stable platform for photocatalysis? Mineralization of reduced graphene oxide with UV-irradiated TiO_2 nanoparticles, Chem. Mater. 26 (2014) 4662–4668.

[95] E. Kecsenovity, B. Endrődi, Z. Pápa, K. Hernádi, K. Rajeshwar, C. Janáky, Decoration of ultra-long carbon nanotubes with Cu_2O nanocrystals: A hybrid platform for enhanced photoelectrochemical CO_2 reduction, J. Mater. Chem. A 4 (2016) 3139–3147.

[96] S. Krishnamurthy, P. V. Kamat, CdSe-graphene oxide light-harvesting assembly: Size-dependent electron transfer and light energy conversion aspects, ChemPhysChem 15 (2014) 2129–2135.

[97] I. V. Lightcap, P. V. Kamat, Graphitic design: Prospects of graphene-based nanocomposites for solar energy conversion, storage, and sensing, Acc. Chem. Res. 46 (2013) 2235–2243.

[98] A. Du, Y.H. Ng, N.J. Bell, Z. Zhu, R. Amal, S.C. Smith, Hybrid graphene/titania nanocomposite: Interface charge transfer, hole doping, and sensitization for visible light response, J. Phys. Chem. Lett. 2 (2011) 894–899.

[99] Y. Liu, D.-P. Wang, Y.-X. Yu, W.-D. Zhang, Preparation and photoelectrochemical properties of functional carbon nanotubes and Ti co-doped Fe_2O_3 thin films, Int. J. Hydrogen Energy. 37 (2012) 9566–9575.

[100] G. Williams, B. Seger, P. V. Kamat, TiO_2-graphene nanocomposites. UV-assisted photocatalytic reduction of graphene oxide, ACS Nano 2 (2008) 1487–1491.

[101] F. Vietmeyer, B. Seger, P. V. Kamat, Anchoring ZnO particles on functionalized single wall carbon nanotubes. Excited state interactions and charge collection, Adv. Mater. 19 (2007) 2935–2940.

[102] H. Zhang, G. Cao, W. Wang, K. Yuan, B. Xu, W. Zhang, J. Cheng, Y. Yang, Influence of microstructure on the capacitive performance of polyaniline/carbon nanotube array composite electrodes, Electrochim. Acta 54 (2009) 1153–1159.

[103] C. Peng, J. Jin, G.Z. Chen, In situ electrochemical polymerization of a nanorod-PANI–graphene composite in a reverse micelle electrolyte and its application in a supercapacitor, Phys. Chem. Chem. Phys. 14 (2012) 15652-15656.

[104] A. Österholm, T. Lindfors, J. Kauppila, P. Damlin, C. Kvarnström, Electrochemical incorporation of graphene oxide into conducting polymer films, Electrochim. Acta 83 (2012) 463–470.

[105] D-J. Guo, H-L. Li, Well-dispersed multi-walled carbon nanotube/polyaniline composite films, J. Sol. State Electrochem. 9 (2005) 445–449.

[106] C. Peng, J. Jin, G.Z. Chen, A comparative study on electrochemical co-deposition and capacitance of composite films of conducting polymers and carbon nanotubes, Electrochim. Acta 53 (2007) 525–537.

[107] C. Oueiny, S. Berlioz, F.X. Perrin, Carbon nanotube-polyaniline composites, Prog. Polym. Sci. 39 (2014) 707–748.

[108] Y. Lin, X. Cui, Electrosynthesis, characterization, and application of novel hybrid materials based on carbon nanotube–polyaniline–nickel hexacyanoferrate nanocomposites, J. Mater. Chem. 16 (2006) 585–592.

[109] H. Zhang, G. Cao, Z. Wang, Y. Yang, Z. Shi, Z. Gu, Tube-covering-tube nanostructured polyaniline/carbon nanotube array composite electrode with high capacitance and superior rate performance as well as good cycling stability, Electrochem. Commun. 10 (2008) 1056–1059.

[110] Y. Xiao, J.-Y. Lin, S.-Y. Tai, S.-W. Chou, G. Yue, J. Wu, Pulse electropolymerization of high performance PEDOT/MWCNT counter electrodes for Pt-free dye-sensitized solar cells, J. Mater. Chem. 22 (2012) 19919-19925.

[111] D. Wang, F. Li, J. Zhao, W. Ren, Z. Chen, J. Tan, Z. Wu, I. Gentle, G.Q. Lu, H. Cheng, Fabrication of graphene/polyaniline composite paper via in situ anodic electropolymerization for high-performance flexible electrode, ACS Nano 3 (2009) 1745–1752.

[112] Z. Niu, P. Luan, Q. Shao, H. Dong, J. Li, J. Chen, D. Zhao, L. Cai, W. Zhou, X. Chen, S. Xie, A "skeleton/skin" strategy for preparing ultrathin free-standing single-walled carbon nanotube/polyaniline films for high performance supercapacitor electrodes, Energy Environ. Sci. 5 (2012) 8726-8733.

[113] D. Fejes, Z. Pápa, E. Kecsenovity, B. Réti, Z. Toth, K. Hernádi, Super growth of vertically aligned carbon nanotubes on pulsed laser deposited catalytic thin films, Appl. Phys. A 118 (2015) 855–861.

[114] Y. Hu, Y. Zhao, Y. Li, H. Li, H. Shao, L. Qu, Defective super-long carbon nanotubes and polypyrrole composite for high-performance supercapacitor electrodes, Electrochim. Acta. 66 (2012) 279–286.

[115] W.N. Wang, J. Soulis, Y. Jeffrey Yang, P. Biswas, Comparison of CO_2 photoreduction systems: A review, Aerosol Air Qual. Res. 14 (2014) 533–549.

[116] W. Tu, Y. Zhou, Z. Zou, Photocatalytic conversion of CO_2 into renewable hydrocarbon fuels: state-of-the-art accomplishment, challenges, and prospects, Adv. Mater. 26 (2014) 4607–4626.

[117] A. Sápi, A. Varga, G.F. Samu, D. Dobó, K.L. Juhász, B. Takács, E. Varga, Á. Kukovecz, Z. Kónya, C. Janáky, Photoelectrochemistry by design: Tailoring the nanoscale structure of Pt/NiO composites leads to enhanced photoelectrochemical hydrogen evolution performance, J. Phys. Chem. C. 121 (2017) 12148–12158.

[118] R. Hinogami, Y. Nakamura, S. Yae, Y. Nakato, An approach to ideal semiconductor electrodes for efficient photoelectrochemical reduction of carbon dioxide by modification with small metal particles, J. Phys. Chem. B 102 (1998) 974–980.

[119] Q. Shen, Z. Chen, X. Huang, M. Liu, G. Zhao, High-yield and selective photoelectrocatalytic reduction of CO_2 to formate by metallic copper decorated Co_3O_4 nanotube arrays, Environ. Sci. Technol. 49 (2015) 5828–5835.

[120] S. Sato, T. Arai, T. Morikawa, K. Uemura, T.M. Suzuki, H. Tanaka, T. Kajino, Selective CO_2 conversion to formate conjugated with H_2O oxidation utilizing semiconductor/complex hybrid photocatalysts, J. Am. Chem. Soc. 133 (2011) 15240–15243.

[121] K. Alenezi, S.K. Ibrahim, P. Li, C.J. Pickett, Solar Fuels: Photoelectrosynthesis of CO from CO_2 at p-type Si using Fe porphyrin electrocatalysts, Chem. - A Eur. J. 19 (2013) 13522–13527.

[122] Y. Liu, Y. Yang, Q. Sun, Z. Wang, B. Huang, Y. Dai, X. Qin, X. Zhang, Chemical adsorption enhanced CO_2 capture and photoreduction over a copper porphyrin based metal organic framework, ACS Appl. Mater. Interfaces. 5 (2013) 7654–7658.

[123] E.E. Barton, D.M. Rampulla, A.B. Bocarsly, Selective solar-driven reduction of CO_2 to methanol using a catalyzed p-GaP based photoelectrochemical cell, J. Am. Chem. Soc. 130 (2008) 6342–6344.

[124] A.A. Pud, Y. V Noskov, A. Kassiba, K.Y. Fatyeyeva, N.A. Ogurtsov, M. Makowska-Janusik, W. Bednarski, M. Tabellout, G.S. Shapoval, New aspects of the low-concentrated aniline polymerization in the solution and in SiC nanocrystals dispersion, J. Phys. Chem. B 111 (2007) 2174–2180.

[125] A. Kassiba, W. Bednarski, A. Pud, N. Errien, M. Makowska-Janusik, L. Laskowski, M. Tabellout, S. Kodjikian, K. Fatyeyeva, N. Ogurtsov, Y. Noskov, Hybrid core-shell nanocomposites based on silicon carbide nanoparticles functionalized by conducting polyaniline: electron paramagnetic resonance investigations, J. Phys. Chem. C 111 (2007) 11544–11551.

[126] J.F. Felix, E.A. de Vasconcelos, E.F. da Silva, W.M. de Azevedo, Fabrication and electrical characterization of polyaniline/silicon carbide heterojunctions, J. Phys. D. Appl. Phys. 44 (2011) 205101-1-205101-5.

[127] J.F. Felix, D.L. Da Cunha, M. Aziz, E.F. Da Silva, D. Taylor, M. Henini, W.M. De Azevedo, Effect of gamma radiation on the electrical properties of polyaniline/silicon carbide heterojunctions, Radiat. Meas. 71 (2014) 402–406.

[128] P. Mavinakuli, S. Wei, Q. Wang, A.B. Karki, S. Dhage, Z. Wang, D.P. Young, Z. Guo, Polypyrrole/silicon

carbide nanocomposites with tunable electrical conductivity, J. Phys. Chem. C 114 (2010) 3874–3882.

[129] M. Omastová, K. Boukerma, M.M. Chehimi, M. Trchová, Novel silicon carbide/polypyrrole composites; preparation and physicochemical properties, Mater. Res. Bull. 40 (2005) 749–765.

[130] K. Zhang, M. Sun, W. Jiang, Y. Wang, D. Wang, F. Wu, A. Xie, W. Dong, A core-shell polypyrrole@silicon carbide nanowire (PPy@SiC) nanocomposite for the broadband elimination of electromagnetic pollution, RSC Adv. 6 (2016) 43056–43059.

[131] M. Mičušík,, M. Omastová, K. Boukerma, A. Albouy, M.M. Chehimi, M. Trchová, P. Fedorko, Preparation, surface chemistry, and electrical conductivity of novel silicon carbide/polypyrrole composites containing an anionic surfactant, Polym. Eng. Sci. 47 (2007) 1198–1206.

[132] A. Peled, J.-P. Lellouche, Preparation of a novel functional SiC@polythiophene nanocomposite of a core-shell morphology, J. Mater. Chem. 22 (2012) 2069–2073.

[133] A. Jarkov, S. Bereznev, O. Volobujeva, R. Traksmaa, A. Tverjanovich, A. Öpik, E. Mellikov, Photo-assisted electrodeposition of polypyrrole back contact to CdS/CdTe solar cell structures, Thin Solid Films 535 (2013) 198–201.

[134] J.C. Colmenares, R. Luque, Heterogeneous photocatalytic nanomaterials: Transformations of biomass-derived compounds, Chem. Soc. Rev. 43 (2014) 765–778.

[135] C. Janáky, N.R. De Tacconi, W. Chanmanee, K. Rajeshwar, Bringing conjugated polymers and oxide nanoarchitectures into intimate contact: Light-induced electrodeposition of polypyrrole and polyaniline on nanoporous WO_3 or TiO_2 nanotube array, J. Phys. Chem. C 116 (2012) 19145–19155.

[136] A. Yildiz, A. Sobczynski, A.J. Bard, A. Campion, M.A. Fox, T.E. Mallouk, S.E. Webber, J.M. White, Sensitized polypyrrole-coated semiconducting powders as materials in photosystems for hydrogen generation, Langmuir 5 (1989) 148–149.

[137] M.A. Fox, K.L. Worthen, Comparison of the physical properties of polypyrrole produced by anodic oxidation and by photoelectrochemical activation of TiO_2, Chem. Mater. 3 (1991) 253–257.

[138] A. Ramanavicius, V. Karabanovas, A. Ramanaviciene, R. Rotomskis, Stabilization of (CdSe)ZnS quantum dots with polypyrrole formed by UV/Vis irradiation initiated polymerization, J. Nanosci. Nanotechnol. 9 (2009) 1909–1915.

[139] F. Goubard, P.-H. Aubert, K. Boukerma, E. Pauthe, C. Chevrot, Elaboration of nanohybrid materials by photopolymerisation of 3,4-ethylenedioxythiophene on TiO_2, Chem. Commun. (2008) 3139–3141.

[140] Z. Weng, X. Ni, Oxidative polymerization of pyrrole photocatalyzed by TiO_2 nanoparticles and interactions in the composites, J. Appl. Polym. Sci. 110 (2008) 109–116.

[141] C. Janáky, W. Chanmanee, K. Rajeshwar, Mechanistic aspects of photoelectrochemical polymerization of polypyrrole on a TiO_2 nanotube array, Electrochim. Acta 122 (2014) 303–309.

[142] A. Varga, B. Endrődi, V. Hornok, C. Visy, C. Janáky, Controlled photocatalytic deposition of CdS nanoparticles on poly(3-hexylthiophene) nanofibers: A versatile approach to obtain organic/inorganic hybrid semiconductor assemblies, J. Phys. Chem. C 119 (2015) 28020–28027.

[143] S.H. Domingues, R. V Salvatierra, M.M. Oliveira, A.J.G. Zarbin, Transparent and conductive thin films of graphene/polyaniline nanocomposites prepared through interfacial polymerization, Chem. Commun. 47 (2011) 2592–2594.

[144] S. Biswas, L.T. Drzal, Multilayered nanoarchitecture of graphene nanosheets and polypyrrole nanowires for high performance supercapacitor electrodes, Chem. Mater. 22 (2010) 5667–5671.

[145] I.D. Baikie, A.C. Grain, J. Sutherland, J. Law, Ambient pressure photoemission spectroscopy of metal surfaces, Appl. Surf. Sci. 323 (2014) 45–53.

[146] K. Rajeshwar, Electron transfer at semiconductor–electrolyte interfaces, in: V. Balzani (Ed.), Electron Transf. Chem., Wiley- VCH, Weinheim, 2001., pp:3-47.

[147] Z. Chen, T.G. Deutsch, H.N. Dinh, K. Domen, K. Emery, A.J. Forman, N. Gaillard, R. Garland, C. Heske, T.F. Jaramillo, A. Kleiman-Shwarsctein, E. Miller, K. Takanabe, J. Turner, Photoelectrochemical water splitting, Springer, 2013., pp:87-97.

[148] R. Ramya, R. Sivasubramanian, M.V. Sangaranarayanan, Conducting polymers-based electrochemical supercapacitors—Progress and prospects, Electrochim. Acta 101 (2013) 109–129.

[149] S. Sahoo, G. Karthikeyan, G.C. Nayak, C.K. Das, Electrochemical characterization of in situ polypyrrole coated graphene nanocomposites, Synth. Met. 161 (2011) 1713–1719.

[150] J. Zhang, L.-B. Kong, B. Wang, Y.-C. Luo, L. Kang, In-situ electrochemical polymerization of multi-walled carbon nanotube/polyaniline composite films for electrochemical supercapacitors, Synth. Met. 159 (2009) 260–266.

[151] W. Zou, W. Wang, B. He, M. Sun, M. Wang, L. Liu, X. Xu, Effects of counterions on pseudocapacitance performance of polyaniline in sulfuric acid and p-toluene sulphonic acid electrolyte, J. Electroanal. Chem. 641 (2010) 111–118.

[152] Y. Ma, S.R. Pendlebury, A. Reynal, F. Le Formal, J.R. Durrant, Dynamics of photogenerated holes in undoped $BiVO_4$ photoanodes for solar water oxidation, Chem. Sci. 5 (2014) 2964-2973.

[153] F. Le Formal, S.R. Pendlebury, M. Cornuz, S.D. Tilley, M. Grätzel, J.R. Durrant, Back electron–hole recombination in hematite photoanodes for water splitting, J. Am. Chem. Soc. 136 (2014) 2564–2574.

[154] V. Noack, H. Weller, A. Eychmüller, Electron transport in particulate ZnO electrodes: A simple approach, J. Phys. Chem. B. 106 (2002) 8514–8523.

[155] https://www.shimadzu.com/an/journal/selection/SR13_001E.pdf. last visited: 2018.02.02.

[156] D.M. DeLongchamp, B.D. Vogt, C.M. Brooks, K. Kano, J. Obrzut, C.A. Richter, O.A. Kirillov, E.K. Lin, Influence of a water rinse on the structure and properties of poly(3,4-ethylene dioxythiophene):poly(styrene sulfonate) films, Langmuir 21 (2005) 11480–11483.

[157] P. Kilmartin, G. Wright, Photoeffects at a polyaniline film electrode, Electrochim. Acta 41 (1996) 1677–1687.

[158] J.X. Huang, R.B. Kaner, Flash welding of conducting polymer nanofibres, Nat. Mater. 3 (2004) 783–786.

[159] S. Quillard, G. Louran, S. Lefrant, A.G. MacDiarmid, Vibrational analysis of polyaniline: A comparative study of leucoemeraldine, emeraldine, and perigraniline bases, Phys. Rev. B 50 (1994) 496–508.

[160] A. Danon, P. Stair, E. Weitz, FTIR study of CO_2 adsorption on amine-grafted SBA-15: Elucidation of adsorbed species, J. Phys. Chem. C 115 (2011) 11540–11549.

[161] W.C. Wilfong, C.S. Srikanth, S.S.C. Chuang, In situ ATR and DRIFTS studies of the nature of adsorbed CO_2 on tetraethylenepentamine films., ACS Appl. Mater. Interfaces 6 (2014) 13617–13626.

[162] X. Wu, W. Pei, H. Zhang, Y. Chen, X. Guo, H. Chen, S. Wang, Sodium dodecyl sulfate doping PEDOT to enhance the performance of neural microelectrode, J. Electroanal. Chem. 758 (2015) 26–32.

[163] E.F. Antunes, A.O. Lobo, E.J. Corat, V.J. Trava-Airoldi, A.A. Martin, C. Veríssimo, Comparative study of first- and second-order Raman spectra of MWCNT at visible and infrared laser excitation, Carbon 44 (2006) 2202–2211.

[164] C. Zhou, Z. Liu, X. Du, S.P. Ringer, Electrodeposited PEDOT films on ITO with a flower-like hierarchical structure, Synth. Met. 160 (2010) 1636–1641.

[165] N. Sakmeche, J.J. Aaron, M. Fall, S. Aeiyach, M. Jouini, J.C. Lacroix, P.C. Lacaze, Anionic micelles; a new aqueous medium for electropolymerization of poly(3,4-ethylenedioxythiophene) films on Pt electrodes, Chem. Commun. (1996) 2723-2724.

[166] L. Jin, T. Wang, Z.-Q. Feng, M.K. Leach, J. Wu, S. Mo, Q. Jiang, A facile approach for the fabrication of

core–shell PEDOT nanofiber mats with superior mechanical properties and biocompatibility, J. Mater. Chem. B 1 (2013) 1818-1825.

[167] S. Garreau, G. Louarn, J. Buisson, In situ spectroelectrochemical Raman studies of poly (3,4-ethylenedioxythiophene) (PEDT), Macromolecules 32 (1999) 6807-6812.

[168] X. Chen, F. Meng, Z. Zhou, X. Tian, L. Shan, S. Zhu, X. Xu, M. Jiang, L. Wang, D. Hui, Y. Wang, J. Lu, J. Gou, One-step synthesis of graphene/polyaniline hybrids by in situ intercalation polymerization and their electromagnetic properties, Nanoscale. 6 (2014) 8140–8148.

[169] H. Yu, T. Wang, B. Wen, M. Lu, Z. Xu, C. Zhu, Y. Chen, X. Xue, C. Sun, M. Cao, Graphene/polyaniline nanorod arrays: Synthesis and excellent electromagnetic absorption properties, J. Mater. Chem. 22 (2012) 21679-21685.

[170] A.C. Ferrari, D.M. Basko, Raman spectroscopy as a versatile tool for studying the properties of graphene, Nat. Nanotechnol. 8 (2013) 235–246.

[171] A.C. Ferrari, J. Robertson, Interpretation of Raman spectra of disordered and amorphous carbon, Phys. Rev. B 61 (2000) 14095–14107.

[172] E. Poverenov, Y. Sheynin, N. Zamoshchik, A. Patra, G. Leitus, I.F. Perepichka, M. Bendikov, Flat conjugated polymers combining a relatively low HOMO energy level and band gap: Polyselenophenes versus polythiophenes, J. Mater. Chem. 22 (2012) 14645-14655.

[173] S. Ghosh, N.A. Kouame, S. Remita, L. Ramos, F. Goubard, P.-H. Aubert, A. Dazzi, A. Deniset-Besseau, H. Remita, Visible-light active conducting polymer nanostructures with superior photocatalytic activity, Sci. Rep. 5 (2016) 18002-1-18002-9.

[174] Z. Chen, T.G. Deutsch, H.N. Dinh, K. Domen, K. Emery, A.J. Forman, N. Gaillard, R. Garland, C. Heske, T.F. Jaramillo, A. Kleiman-Shwarsctein, E. Miller, K. Takanabe, J. Turner, Photoelectrochemical water splitting, Springer, 2013., pp:76.

[175] P. Sen, A. De, Electrochemical performances of poly(3,4-ethylenedioxythiophene)–$NiFe_2O_4$ nanocomposite as electrode for supercapacitor, Electrochim. Acta 55 (2010) 4677–4684.

[176] S.H. Aboutalebi, A.T. Chidembo, M. Salari, K. Konstantinov, D. Wexler, H.K. Liu, S.X. Dou, Comparison of GO, GO/MWCNTs composite and MWCNTs as potential electrode materials for supercapacitors, Energy Environ. Sci. 4 (2011) 1855-1865.

[177] Q. Yang, S.-K. Pang, K.-C. Yung, Study of PEDOT–PSS in carbon nanotube/conducting polymer composites as supercapacitor electrodes in aqueous solution, J. Electroanal. Chem. 728 (2014) 140–147.

[178] M. Braik, M.M. Barsan, C. Dridi, M. Ben Ali, C.M.A. Brett, Highly sensitive amperometric enzyme biosensor for detection of superoxide based on conducting polymer/CNT modified electrodes and superoxide dismutase, Sensors Actuators, B Chem. 236 (2016) 574–582.

[179] N.H. Nabilah Azman, H.N. Lim, Y. Sulaiman, Effect of electropolymerization potential on the preparation of PEDOT/graphene oxide hybrid material for supercapacitor application, Electrochim. Acta 188 (2016) 785–792.

[180] G. Wu, L. Li, J.-H. Li, B.-Q. Xu, Polyaniline-carbon composite films as supports of Pt and PtRu particles for methanol electrooxidation, Carbon 43 (2005) 2579–2587.

[181] W.J. Zhang, J. Feng, A.G. MacDiarmid, A.J. Epstein, Synthesis of oligomeric anilines, Synth. Met. 84 (1997) 119–120.

[182] S.-X. Wang, Z.-C. Tan, Y.-S. Li, L.-X. Sun, Y. Li, A kinetic analysis of thermal decomposition of polyaniline/ZrO_2 composite, J. Therm. Anal. Calorim. 92 (2008) 483–487.

[183] K.J. Kim, S. Lee, J.H. Lee, M.-H. Roh, K.-Y. Lim, Y.-W. Kim, Structural and optical characteristics of crystalline silicon carbide nanoparticles synthesized by carbothermal reduction, J. Am. Ceram. Soc. 92 (2009) 424–428.

[184] A. Kassiba, M. Makowska-Janusik, J. Bouclé, J.F. Bardeau, A. Bulou, N. Herlin-Boime, Photoluminescence features on the Raman spectra of quasistoichiometric SiC nanoparticles: Experimental and numerical simulations, Phys. Rev. B 66 (2002) 155317-1-155317–7.

[185] G. Louarn, M. Lapkowski, S. Quillard, A. Pron, J.P. Buisson, S. Lefrant, Vibrational properties of polyaniline-isotope effects, J. Phys. Chem. 100 (1996) 6998–7006.

[186] R. Mažeikienė, V. Tomkutė, Z. Kuodis, G. Niaura, A. Malinauskas, Raman spectroelectrochemical study of polyaniline and sulfonated polyaniline in solutions of different pH, Vib. Spectrosc. 44 (2007) 201–208.

[187] S. Quillard, K. Berrada, G. Louam, S. Lefrant, Polyanilines and substituted polyanilines: A comparative study of the Raman spectra of leucoemeraldine, emeraldine and pernigraniline, in: Int. Conf. Sci. Technol. Synth. Met., IEEE, 1994: pp. 201–204.

[188] X.-R. Zeng, T.-M. Ko, Structures and properties of chemically reduced polyanilines, Polymer 39 (1998) 1187–1195.

[189] H. Neugebauer, In situ vibrational spectroscopy of conducting polymer electrodes, Macromol. Symp. 94 (1995) 61–73.

[190] M. Kim, I. Oh, J. Kim, Hierarchical porous silicon carbide with controlled micropores and mesopores for electric double layer capacitors, J. Power Sources 282 (2015) 277–285.

[191] M. Kim, I. Oh, J. Kim, Influence of surface oxygen functional group on the electrochemical behavior of porous silicon carbide based supercapacitor electrode, Electrochim. Acta 196 (2016) 357–368.

[192] Y. Zhao, W. Kang, L. Li, G. Yan, X. Wang, X. Zhuang, B. Cheng, Solution blown silicon carbide porous nanofiber membrane as electrode materials for supercapacitors, Electrochim. Acta 207 (2016) 257–265.

ACKNOWLEDGEMENT

I am grateful to the Head of Department of Physical Chemistry and Materials Science, **Dr. Ágota Tóth**, for allowing me to carry out my doctoral work in her department.

I would like to thank my supervisors, **Dr. Csaba Janáky** and **Dr. Csaba Visy** for assisting in my scientific development since my second undergraduate year. Their guidance and advices always helped me not just to become a better researcher, but to grow as a person, too. Finally, I am also grateful for the countless opportunities and encouraging words, provided by them to present my work on international conferences or to spend ten months in the United States as a visiting scholar.

I owe special thanks to **Dr. Krishnan Rajeshwar**, who was much more than a supervisor to me, while I was conducting research at UTA. Long walks, deep conversations during our coffee-, or wine sessions taught me a lot not only about science and scientific thinking, but about life in general.

I would like to also thank **Dr. András Sápi** for his help during the TGA measurements.

Many thanks to the former, and current members of the research group for all their help and for providing an honest, friendly, and creative working environment. I would like to highlight **Dr. Balázs Endrődi**, **Dorottya Hursán**, **Róbert Ondok**, **Gergely Ferenc Samu** and **Ádám Balog**, who also often helped me during the measurements too.

My deepest gratitude goes to all my **friends, climbing-, and running partners** for all the chats, laughs and activities which always helped me to distract my attention from all the unsuccessful experiments, disappointments with which this journey was often paved with. After these sessions, I've always continued my work with renewed strength and enthusiasm. I am also grateful to my partner, **Vivien** for her kind words and continuous encouragement during the writing process, which gave me strength even in the hardest moments.

Last but not least I owe thanks to my **family**, for their continuous support and encouragement and for providing a peaceful environment during my university and doctoral studies.